Faculteit Wetenschappen

Departement Fysica

An advanced TEM study on quantification of Ni_4Ti_3 precipitates in low temperature aged Ni-Ti shape memory alloy

Een geavanceerde TEM studie over de kwantificatie van Ni_4Ti_3 precipitaten in een Ni-Ti vormgeheugenlegering verouderd bij lage temperatuur

Proefschrift voorgelegd tot het behalen van de graad van Doctor in de Wetenschappen aan de Universiteit Antwerpen, te verdedigen door

Xiayang Yao

Promotor

Prof. Dr. Dominique Schryvers

Co-promotor

Prof. Dr. Xin-Ping Zhang

Antwerp

2019

Doctoral Committee

Chairman

Prof. Dr. Paul Scheunders, University of Antwerp, Belgium

Promoter

Prof. Dr. Dominique Schryvers, University of Antwerp, Belgium

Members

Prof. Dr. Paul De Meulenaere, University of Antwerp, Belgium

Prof. Dr. Jin Won Seo, Catholique University Leuven, Belgium

Dr. Shanshan Cao, South China University of Technology, China

Dr. Wim Tirry, Belgium

Contact information

Xiayang Yao

University of Antwerp – Department of Physics

EMAT – Electron Microscopy for Materials Science

Groenenborgerlaan 171

B-2020 Antwerp

Belgium

xiayang.yao@uantwerpen.be

Introduction

Shape memory alloys (SMAs) are fascinating materials that have the ability to remember their original shape under well-defined temperature or stress conditions. The unique shape memory effect and superelasticity of the SMAs make them stand out of the ordinary metals and alloys. Among these properties, alloys with the two-way shape memory effect (TWSME) have very promising applications such as an artificial anal sphincter since the shape recovery of the alloy occurs during both heating and cooling processes. One of the methods to obtain the TWSME is by constrained aging which introduces aligned Ni_4Ti_3 precipitates in the alloy. During constrained aging, different stresses are applied in different regions of the bulk material which eventually lead to the different distribution of precipitates. Due to the lattice mismatch between the matrix and precipitates, internal stress fields are induced by the precipitates and the stress fields strongly affect the shape change behavior.

In this thesis, a $Ni_{51}Ti_{49}$ alloy is used to fabricate samples with TWSME. Different aging parameters are involved during the material preparation process which leads to different shape change behaviors. Different shape recovery abilities are observed from the alloys with different aging parameters and an abnormal shape change behavior is observed compared to the normal TWSME alloys. All these properties are closely related to the size, morphology, and distribution of the precipitates. A quantitative study of the precipitates can give a better understanding of the anisotropic precipitation mechanism in this alloy which can improve functional properties of the material. Automated Crystal Orientation Mapping in TEM (ACOM-TEM) which obtains orientation and phase information in TEM images is used as the main technology to quantitatively characterize the size and distribution of precipitates, together with other TEM techniques such as electron diffraction, bright/dark field imaging and high resolution TEM imaging. Since it was the first attempt to apply ACOM-TEM on the characterization of Ni-Ti alloys containing Ni_4Ti_3 precipitates, an optimization process was

made to improve the quality of the collected images. After the optimization, the technique is used to quantify the various cases of treatment studied. The results reveal the influence of aging parameters to the nucleation and growth of the precipitates as well as the relation between the external stress and precipitates.

The content of this thesis is divided into five chapters, organized as follows:

Chapter 1 provides a general introduction to the SMAs from the aspect of structure, properties, and applications. The Ni_4Ti_3 precipitate which plays an important role in the shape memory behavior is also introduced including its influence on the material under different conditions.

Chapter 2 gives a review of experimental methodologies used in this thesis. These methodologies include basic and advanced TEM techniques and TEM sample preparation methods. ACOM-TEM is introduced in detail since it is a relatively new technique.

Chapter 3 covers all results from the optimization process of ACOM-TEM applied on Ni-Ti alloys. Parameters that can affect the final mapping results are optimized both from data collection and diffraction pattern simulation parts. After the optimization, clear orientation and phase mapping images can be obtained and used for quantitative analysis.

Chapter 4 investigates the influence of aging parameters on the shape recovery ability of the Ni-Ti alloy with constrained aging treatment. Quantitative data are extracted from orientation and phase mapping images. The relation between the size, morphology, and distribution of the precipitates to the shape change behavior is discussed, and the relation between the precipitates and external stress is discussed as well.

Chapter 5 studies the precipitates generated under low-temperature aging conditions where the precipitates are still at the nano-scale size. The relation between the abnormal TWSME and precipitates is discussed with a quantitative study on the size of the precipitates.

Inleiding

De vormgeheugenlegeringen (SMA's) zijn fascinerende materialen die hun originele vorm kunnen onthouden onder goed gedefinieerde temperatuur- of stressomstandigheden. Het unieke vormgeheugeneffect en de superelasticiteit van de SMA's geven ze een aparte plaats tussen de gewone metalen en legeringen. Onder deze eigenschappen heeft de legering met het bidirectionele vormgeheugeneffect (TWSME) veelbelovende toepassingen zoals een kunstmatige anale sluitspier, omdat het vormherstel van de legering plaatsvindt tijdens zowel verwarmings- als koelprocessen. Een van de methoden om het TWSME te verkrijgen is door beperkte veroudering die uitgelijnde Ni_4Ti_3 precipitaten in de legering introduceert. Tijdens beperkte veroudering worden verschillende spanningen uitgeoefend in verschillende gebieden van het bulkmateriaal die uiteindelijk leiden tot de verschillende verdeling van de precipitaten. Vanwege de roosterafwijking tussen de matrix en de precipitaten, worden interne spanningsvelden geïnduceerd en beïnvloeden de stressvelden het gedrag van vormverandering.

In dit proefschrift wordt een $Ni_{51}Ti_{49}$ legering gebruikt om stalen met TWSME te fabriceren. Verschillende verouderingsparameters zijn betrokken tijdens het materiaalvoorbereidingsproces dat leidt tot verschillend gedrag van vormverandering. Verschillende vormherstelmogelijkheden worden waargenomen in de legeringen met verschillende verouderingsparameters en een abnormaal gedrag van vormverandering wordt waargenomen in vergelijking met normale TWSME legeringen. Al deze eigenschappen hangen nauw samen met de grootte, morfologie en verdeling van de precipitaten. Een kwantitatief onderzoek van de precipitaten kan een beter begrip geven van het anisotrope precipitatiemechanisme in deze legering zodat we deekunnen verbeteren. Geautomatiseerde kristaloriëntatiemapping in TEM (ACOM-TEM) die oriëntatie- en fase-informatie verkrijgt wanneer toegepast op TEM beelden, wordt gebruikt als de belangrijkste methode om de

grootte en verdeling van precipitaten kwantitatief te bepalen, samen met andere TEM-technieken zoals elektronendiffractie, helder-/donkerveld en hoge resolutie TEM beeldvorming. Aangezien het de eerste poging was om ACOM-TEM toe te passen op het karakteriseren van Ni-Ti legeringen met Ni_4Ti_3 precipitaten, werd een optimalisatieproces uitgevoerd om de kwaliteit van de verzamelde afbeeldingen te verbeteren en na de optimalisatie wordt de techniek gebruikt voor kwantitatief onderzoek. De resultaten onthulden de invloed van verouderingsparameters op de kernvorming en groei van het precipitaten en hun relatie met de uitwendige stress.

De inhoud van dit proefschrift is verdeeld in vijf hoofdstukken, als volgt georganiseerd:

Hoofdstuk 1 biedt een algemene inleiding tot de SMA's vanuit het oogpunt van structuur, eigenschappen en toepassingen. De Ni_4Ti_3 precipitaten die een belangrijke rol spelen in het vormgeheugengedrag worden ook geïntroduceerd en hun invloed op het materiaal onder verschillende omstandigheden wordt toegelicht.

Hoofdstuk 2 geeft een overzicht van de experimentele methoden die in dit proefschrift worden gebruikt. Deze methoden omvatten basis- en gevorderde TEM-technieken en TEM-monsterbereidingsmethoden. ACOM-TEM wordt in detail geïntroduceerd omdat het een relatief nieuwe techniek is.

Hoofdstuk 3 behandelt alle optimalisatieprocessen van ACOM-TEM toegepast op de Ni-Ti legeringen. Parameters die de uiteindelijke resultaten kunnen beïnvloeden, zijn geoptimaliseerd voor zowel gegevensverzameling als diffractiepatroonsimulatie. Na de optimalisatie kunnen duidelijke oriëntatie- en fasebeelden worden verkregen en gebruikt voor kwantitatieve analyse.

Hoofdstuk 4 onderzoekt de invloed van verouderingsparameters op het vormherstelvermogen van de Ni-Ti legering met beperkte verouderingsbehandeling. Kwantitatieve gegevens worden geëxtraheerd uit oriëntatie- en fasebeelden. De relatie tussen de grootte, morfologie

en verdeling van de precipitaten tot het gedrag van vormverandering wordt besproken, alsook de relatie tussen de precipitaten en uitwendige stress.

Hoofdstuk 5 bestudeert de precipitaten die werden gegenereerd onder verouderingsomstandigheden bij lage temperatuur waarbij de precipitaten nog op nanoschaalgrootte zijn. De relatie tussen de abnormale TWSME en precipitaten wordt besproken met een kwantitatief onderzoek naar de grootte van de precipitaten.

CONTENTS

Chapter 1

An Introduction to Ni-Ti-based Shape Memory Alloys

1.1 Shape memory alloys: Origin and applications

1.1.1 The origin story

Shape memory alloy (SMA) is a general name for a series of alloys that present the ability to remember their original shapes under well-defined temperature and/or stress conditions. The discovery of the first SMA was made by Buehler et al. in 1963 [1], who were affiliated with the United States Naval Ordnance Laboratory, in an equiatomic binary Ni-Ti alloy that was named Nitinol (Nickel Titanium Naval Ordnance Laboratory). The discovery of Nitinol was serendipitous because their original goal was to find binary alloys with good impact resistance and ductility, and Ni-Ti was among one of several options. To test the fatigue, a Ni-Ti alloy strip was bent into a type of metallic accordion and was heated accidentally by a pipe lighter. When the alloy was heated, the accordion-shaped alloy stretched out longitudinally, and this amazing "automatic" shape change led to the realization and systematic study of SMAs [2]. Strictly speaking, however, the exact origin of this shape memory phenomenon was even earlier. The first report of shape memory-related behavior was made by the Swedish researcher A. Ölander in 1932 who observed rubberlike behavior in a Au-Cd alloy [3]. Later, the formation and disappearance of a so-called martensite phase with temperature control in a Cu-Zn alloy was observed by Greninger et al. in 1937 [4]. The word "martensite", which memorializes German metallurgist Adolf Martens, was initially used to represent the hard phase found in steel after quenching it from a high temperature and

later on it was also used to represent the hard phase in SMA because a similar phase transformation occurs in SMA. Since the 1950s, more studies have focused on this reversible martensitic transformation behavior, and it was found that alloys such as InTl, CuAlNi and AuAgCd could present similar phase transformation behavior. However, these studies did not realize the potential applications of these alloys due to their high material costs, manufacturing complexity and unattractive mechanical properties until the report by Buehler et al. in 1963 [1]. The study of SMAs quickly became popular worldwide, especially for Ni-Ti alloys; over half a century has passed and the study of SMAs is still attracting attention from scientists.

The first commercial Ni-Ti SMA product soon appeared in industry in 1969 and was a “shrink-to-fit” pipe coupler used on a jet fighter built by the Grumman Aerospace Corporation [2]. Both research and application progressed quickly, and the understanding of SMAs improved. In 1974, a two-way shape memory effect (TWSME) was reported in a Ni-Ti alloy by Nagasawa et al. which made shape deformation reversible; before this report, it was only possible to obtain the desired shape via heating but not cooling [5]. The observation of this effect greatly enriched the potential applications of SMAs and raised interest in studying the phase transformation process. In 1984, the all-round shape memory effect (ARSME) was found by Nishida and Honma in Ni-rich Ni-Ti alloys when the material was appropriately aged under constraint conditions [6]. These phenomena are closely related to certain kinds of precipitates being densely dispersed in the alloy, and which later were proved to be Ni4Ti3. In 1985, a rhombohedral phase referred to as the R phase was reported and appearing before the martensitic transformation, depending on the thermomechanical history and composition of the material [7]. The appearance of the R phase reduces the hysteresis of the transformation temperature, which enlarges the possible application of SMAs to situations where a narrow temperature hysteresis is needed. Recently, a “fishtail-like” four-way shape memory effect was observed in compositionally graded Ni-Ti thin plates, which enables the alloy to bend and reverse in a single heating or cooling process [8]. Thus, when a complete

cooling/heating thermal cycle is applied, the shape of the alloy plate will move like a fishtail.

In addition to the long history and vast investigation of binary Ni-Ti alloys, the effect of ternary elements such as Cu, Nb, Fe, Co, Mn and Al on the performance of Ni-Ti SMAs was also studied [9, 10]. Adding Cu to a binary Ni-Ti alloy will narrow the transformation hysteresis compared to that of the binary Ni-Ti system, and the transformation hysteresis could be widened if Nb is added to Ni-Ti alloys [11, 12]. The R phase transformation could be promoted, and the martensitic transformation could be suppressed when iron is added and substitutes for a small amount of Ni [7, 13].

1.1.2 Applications

Because of their extraordinary function and properties SMAs have numerous applications in many sectors, such as automotive, aerospace and biomedical applications and more than 10,000 US SMA-related patents have been granted. In the aerospace industry, one of the early applications for a Ni-Ti alloy was a knitted self-deployed antenna used in outer space. The antenna could be deformed to a very small size in the martensitic state, and after it was launched into space, it would expand into its original dome shape when it was heated by an electric current [14]. SMA parts such as actuators, structural connectors, vibration dampers, sealers, inflatable structures, manipulators etc. are widely used in aircrafts and other industrial applications [15, 16]. Another typical example is a variable geometry chevron (VGC), which is an active serrated aerodynamic device with SMA actuators developed by the Boeing Corporation [17-20]. This device is designed to be very effective in reducing noise during take-off by maximizing the chevron deflection, whereas during the remaining flight time, the cruise efficiency could be increased by minimizing the chevron deflection.

For biomedical applications, SMAs exhibit attractive behavior, such as high corrosion resistance and bio-compatibility, and nonmagnetic and other unique physical properties that replicate those of human tissues and bones. These factors, together with shape memory effects, superelasticity (in which the material shows much more severe elastic properties than

conventional metals) and other excellent mechanical properties such as good ductility and high damping property, make SMAs very appealing. All these properties meet the requirements for precise and reliable miniature instruments to achieve accurate positioning and functioning for complex medical treatments or surgical procedures. SMAs are now applied in many medical fields, including orthopedics, orthodontics, neurology, cardiology and endodontics, where they are used as stents, medical tweezers, sutures, implants and for aneurism treatments [15]. The first biomedical application were superelastic braces made from a Ni-Ti alloy in 1971 [21]. Another more recent application are orthopedic implants, where the SMA is used to help the bone heal rapidly and thus enables it to bear weight and avoid follow-up operations. A Ni-Ti-SMA has been developed where an alterable stiffness could be achieved by triggering the one-way shape memory effect with contactless heat induction [22]. The Ni-Ti alloys discussed in this thesis also aim at biomedical applications, which will be discussed in detail later.

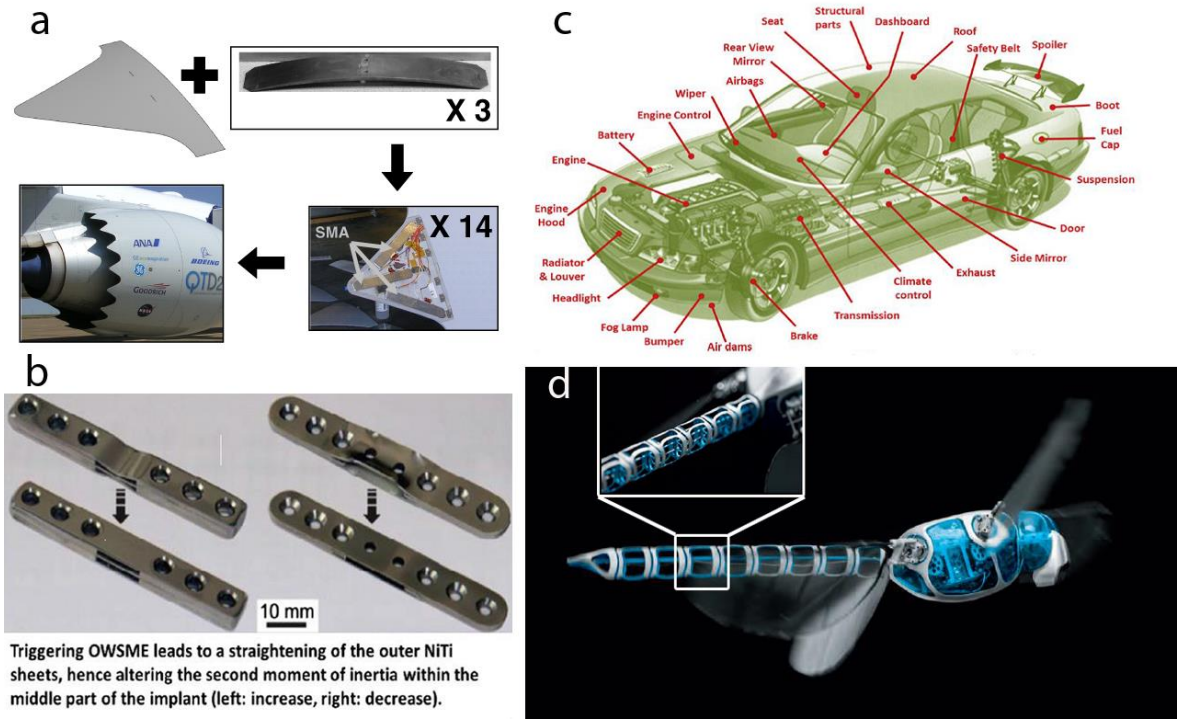

Figure 1.1 Examples of the applications of Ni-Ti-based SMAs: (a) variable geometry chevron on airplane [20], (b) an "alterable stiffness" orthopedic implant [22], (c) existing and potential SMA applications in the automotive domain [15] and (d) the Festo BionicOpter: inspiration of a dragonfly [23].

In the automotive industry, SMAs are now widely used in many components, as indicated in Figure 1.1c. Most of these SMAs applied in the automotive industry comprise the binary Ni-Ti alloy because its operational temperature range lies approximately within the standard range of environmental temperature extremes to which a passenger vehicle may be exposed during service. This required temperature range is approximately from -40℃ to 120℃, which is very close to the transformation temperature of binary Ni-Ti SMAs, i.e., approximately from -50℃ to 110℃ depending on the variation of Ni concentration and heat treatment processes [24]. The robotic industry also provides substantial possibilities for SMAs, which could simplify control systems. One recent extraordinary application was made by collaborators of the Festo Corporation, who designed a bionic dragonfly equipped with Nitinol, as shown in Figure 1.1d. Four flexible Nitinol muscles form the body of the dragonfly and shrink when exposed to heat and expand when cooled down, which enables the dragonfly to fly steadily in all directions [23].

1.2 Phase transformation

1.2.1 Ni-Ti phase diagram

The relevant phase transformation for SM behavior of Ni-Ti is referred to as the martensitic transformation, which is a diffusionless displacive phase transformation in solid materials. To study the transformation process, the phases in the Ni-Ti alloy need to be known first. Figure 1.2a [25] shows the partial phase diagram for Ni-Ti alloys, and this diagram is the cornerstone for investigation of this alloy, especially when heat treatment is involved. The compositions on the diagram are in the vicinity of the equiatomic position, which shows that the main phase at this near-equiatomic composition is NiTi. When the Ni concentration decreases, $NiTi_2$ will appear and when it increases, Ni_3Ti will emerge. The slope of the curve close to the equiatomic NiTi region shows the solubility limit of the alloy, which indicates that the temperature has almost no influence on the Ti-rich side, whereas on the Ni-rich side, the solubility decreases with decreasing temperature. Thus, in Ni-rich Ni-Ti alloys, heat

treatment could be used to control the matrix composition and precipitation.

Figure 1.2b is the time-temperature-transformation diagram describing the aging behavior of a Ni52.0at.%-Ti alloy developed by Nishida et al. [26]. This diagram provides a typical example of how heat treatment influences the phases inside a Ni-Ti alloy. When the alloy is aged at various temperatures after quenching from 1000℃, final stable Ni_3Ti precipitates will appear on the Ni-rich side. Metastable phases also appear during this process when the aging time is short or the temperature is low, such as Ni_4Ti_3 and Ni_3Ti_2. Both of these phases will occur in the alloy when the aging temperature is lower than 873 K (600℃) with increasing aging time, and the final Ni_3Ti could be reached after prolonged aging. From the phase diagram, it is clear that the formation temperature of Ni_4Ti_3 is lower than that of Ni_3Ti_2, which is an indication that a lower nucleation energy is needed for the Ni_4Ti_3 phase; thus, the evolution of phases in the Ni-Ti alloy with increasing aging time at a relatively low temperature is given as NiTi → NiTi + Ni_4Ti_3 → NiTi + Ni_3Ti_2 → NiTi + Ni_3Ti.

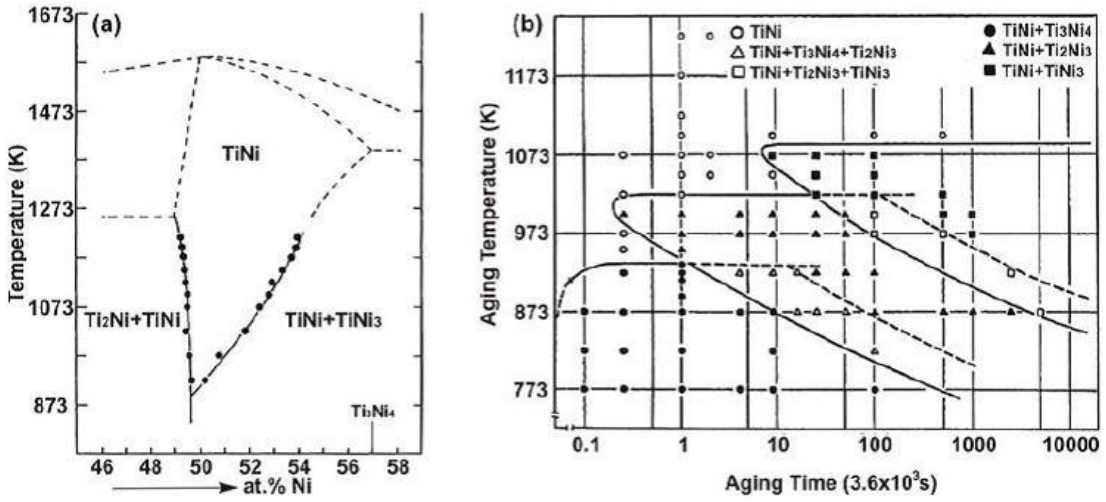

Figure 1.2 (a) Partial equilibrium phase diagram of Ni-Ti in the vicinity of the near-equiatomic ratio [25]. (b) Time-temperature-transformation diagram of a Ni52at.%Ti alloy [26, 27].

Another metastable phase, $NiTi_2$, usually appears in the Ni-Ti matrix during the fabrication of the alloy. Despite the fact that $NiTi_2$ is quite unstable, it readily reacts with oxygen to form

certain oxides, which enable it to remain in the alloy instead of disappearing, even after solution treatment. A eutectoid reaction ($NiTi \rightarrow NiTi_2 + Ni_3Ti$) that was once proposed does not exist [28]. The final stable structure, which was once misinterpreted as $NiTi_2$, is actually Ni_2Ti_4O, and it has a very similar structure to $NiTi_2$ because oxygen atoms take vacant positions in the structure instead of displacing Ni or Ti atoms [29]. Several studies have investigated this phase, and it is known that a higher annealing temperature promotes the formation of Ni_2Ti_4O [30], which is a relevant note since the existence of Ni_2Ti_4O could affect the refinement of the microstructure during processing of the alloy when rolling is involved [31].

1.2.2 Crystal structures of Ni-Ti

In Ni-Ti SMAs, the martensitic transformation occurring during the shape memory or superelasticity behavior is closely related to the binary Ni-Ti phase. This parent or high-temperature phase of the martensitic transformation is usually referred to as austenite and has a B2-type ordered body-centered cubic (BCC) structure. The martensitic transformation of Ni-Ti SMAs has different paths, and the transformation might end up with different structures depending on the composition, temperature or heat treatment process. The martensite in binary Ni-Ti is called B19' and has a monoclinic structure while an orthorhombic B19 phase can also occur in between the B2 and B19' upon adding third elements. In some cases, the rhombohedral R phase may occur prior to the formation of martensite. In the following we will discuss the corresponding structures in detail.

B2 austenite has a space group of $Pm\bar{3}m$, which corresponds to the well-known CsCl structure and has a lattice parameter of a=0.301 nm in Ni-Ti. The atomic sites in the unit cell are defined as Ti (0,0,0) and Ni (1/2,1/2,1/2), as is shown in Figure 1.3a [32].

B19' martensite has a space group of $P2_1/m$ with lattice parameters of a=0.2898 nm, b=0.4108 nm and c=0.4646 nm and a monoclinic angle $\beta=97.78^\circ$ [33, 34]. The atomic positions in this structure are slightly dependent on the composition of the alloy, and one set

of values for the $Ni_{50.8}Ti_{49.2}$ alloy has been given by Kudoh et al. and is shown in Table 1.1 [33]. The unit cell of B19' martensite is shown in Figure 1.3b.

Table 1.1 The atomic coordinates in the B19' unit cell of a $Ni_{50.8}Ti_{49.2}$ alloy.

Atom coordinates	X	Y	Z
Ti1	0	0	0
Ti2	0.1648	0.5	0.5672
Ni1	0.6196	0	0.4588
Ni2	0.5452	0.5	0.1084

The R phase can be regarded as a cubic structure distorted slightly by stretching the cubic parent lattice along the <111> diagonal direction, which ultimately forms a rhombohedral structure. The space group belongs to $P\bar{3}$, and in the hexagonal lattice setting, the lattice parameter of the unit cell is a=0.734 nm and c=0.528 nm, the unit cell of the R phase is shown in Figure 1.3c [32, 35].

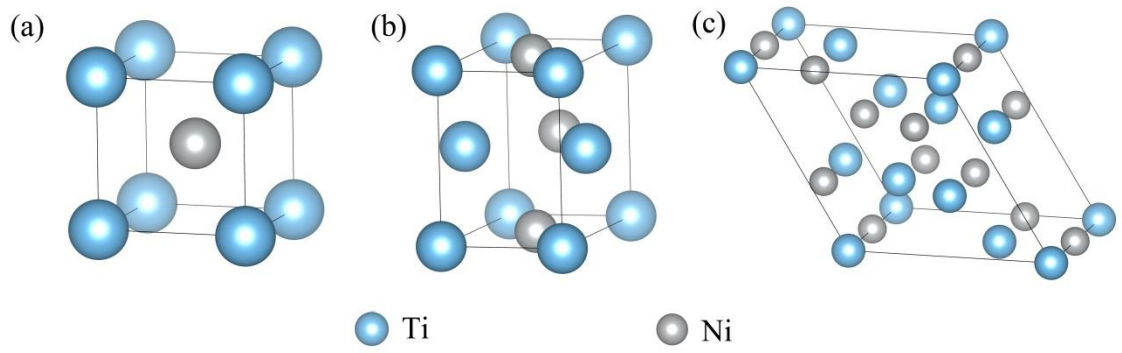

Figure 1.3 Unit cell of the (a) B2 austenite, (b) B19' martensite, and (c) R phase in Ni-Ti alloys.

1.2.3 Martensitic transformation

The martensitic transformation is a diffusionless phase transformation that occurs without the long-range diffusion of atoms but rather by some form of cooperative, homogeneous movement of many atoms that results in a change in crystal structure. With rapid cooling

from a high temperature, the martensitic transformation will occur at a critical temperature, which is known as the martensitic start temperature (M_s). At this M_s temperature, the crystal structure changes abruptly from a high-symmetry structure to a low-symmetry structure, as shown in Figure 1.4. The low-symmetry structure can form in different crystallographic variants and ultimately different variants reach an accommodating shape. If the temperature is raised and the martensite becomes unstable the reverse transformation occurs and the martensite will revert to the austenite phase in the original orientation. This is the origin of the shape memory effect, which will be discussed in detail later.

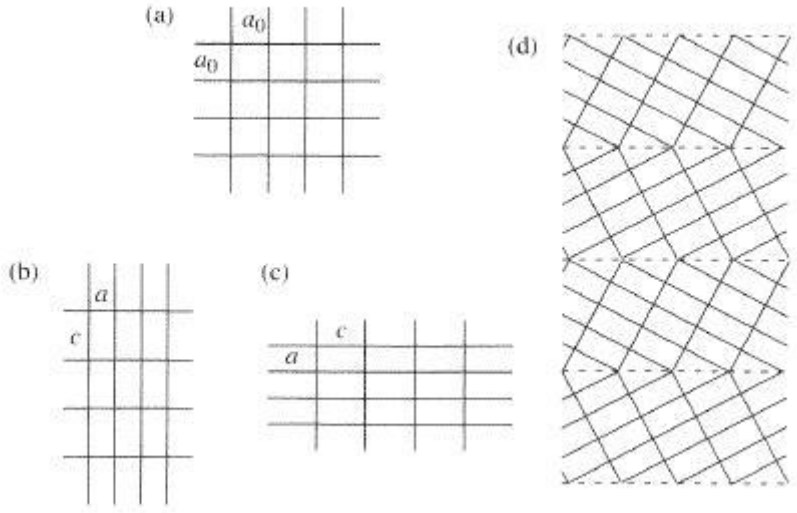

Figure 1.4 A schematic illustration of the martensitic phase transformation: (a) austenite, (b, c) variants of martensite, and (d) a coherent arrangement of alternating variants of martensite [36].

The whole martensitic transformation (MT) process is a displacive (no diffusion) and first-order (abrupt change in the lattice parameter) transformation, which means that its characteristics lie in the cooperative movement of atoms. Because of this, a macroscopic shape change appears associated with the MT even though the relative atomic displacements are small. Figure 1.5 provides a schematic illustration of the macroscopic shape change during a MT, which is a well-known experiment consisting of marking the surface of an austenite single crystal by a straight scratch line XY. After the MT, the scratch line shifted from its original position to the XZ position when it cuts through the martensite, which is the

grey region in figure. The surface plane ADE also changed its position. This result clearly shows that the shape change associated with a MT is linear because upon the transformation, a line and a surface are changed into another line and surface, respectively. This also implies that the shape change associated with a MT can be described by a matrix as an operator.

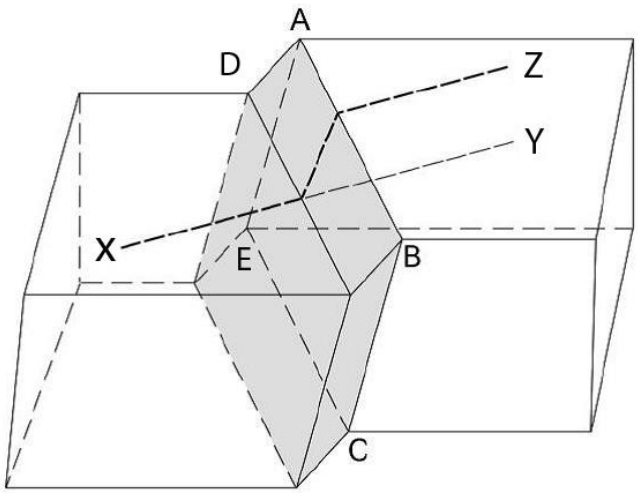

Figure 1.5 Schematic representation of shape change associated with martensitic transformation. The initially straight scratch line XY is transformed to position XZ due to the effect of the MT. The grey region is martensite, and plane ABC is the habit plane.

The plane ABC is neither rotated nor distorted upon transformation, and this plane is called the invariant plane or habit plane of the MT. The habit plane is a reference plane where the parent and product phases are impacted by a homogeneous distortion such that the displacement of any point is in a common direction and proportional to the distance from the reference plane.

A shape change associated with a MT always leads to a large strain around the martensite when it is formed in the parent phase, and it is very important to reduce the strain for further nucleation and growth processes. There are two ways to achieve this goal, namely by introducing slip or twins, both of which are referred to as lattice invariant shears (LIS) because neither of them changes the structure of the martensite. Figure 1.6 shows how

martensite variants accommodate to minimize the deformation energy by slip or twinning. Whether slip or twinning is introduced depends on the kind of alloy, but in SMAs, twinning is the dominant LIS mode.

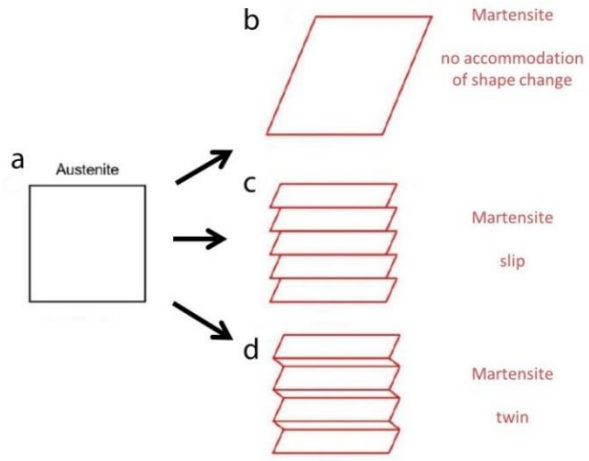

Figure 1.6 Illustration of lattice invariant shear: (a) austenite lattice, (b) shape change and high strain after MT, (c) and (d) show the accommodation of strain by slip and twin, respectively.

For SMAs, the martensitic transformation contains a thermal cycle that includes both cooling and heating processes. Therefore, there are four temperatures needed to describe the whole process of this transformation: M_s, the temperature during cooling when martensite starts to form; M_f, the temperature when the alloy is fully transformed into martensite; A_s, the temperature during heating when austenite starts to form; and A_f, the temperature when the alloy is fully transformed into austenite. When the intermediate R phase also appears, R_s and R_f are used to indicate the start and finish temperature of the R phase transformation, respectively, as shown in Figure 1.7.

1.3 Shape memory effect and superelasticity

1.3.1 Shape memory effect

The shape memory effect (SME) is a thermal elastic martensitic transformation. There are

different kinds of SMEs according to the type of shape reaction that occurs at different temperatures. Two major categories are one-way SME (OWSME) and two-way SME (TWSME) where the phase transformation is controlled by the temperature. The OWSME indicates that shape recovery is possible only in one direction, which is the heating process when the alloy is transformed from martensite to austenite. In order to obtain the shape in the martensite phase, the material needs to be deformed again in every cycle. For TWSME, shape recovery occurs during both the heating and cooling processes. Figure 1.8 clearly shows the shape change routes for both OWSME and TWSME.

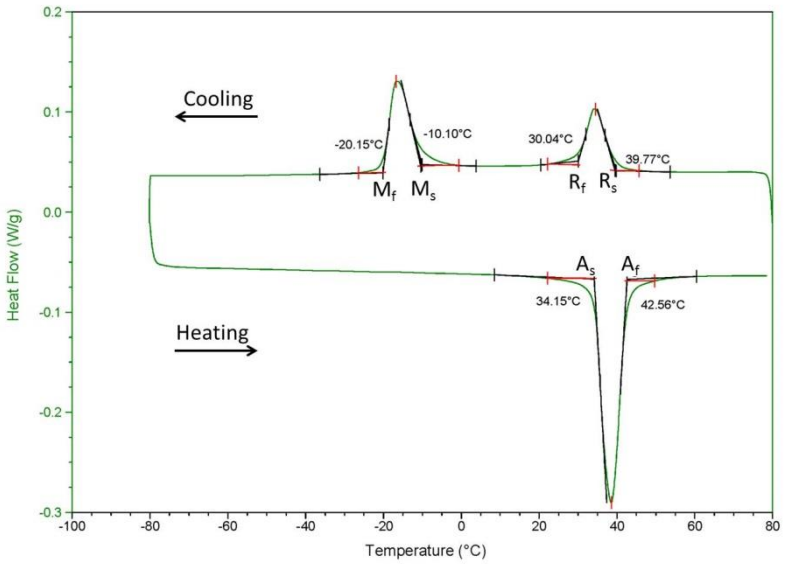

Figure 1.7 DSC curve of a 450 °C, 10 h aged $Ni_{51}Ti_{49}$ alloy, showing M_s, M_f, A_s, A_f, R_s and R_f temperatures.

The SME mechanism can be explained according to Figure 1.8. The initial state of austenite is indicated as position A in the figure, and when the temperature decreases below M_f, the austenite completely transforms to a self-accommodated twinned martensite, which is the B position in Figure 1.8 (and in case the LIS is twinning). At the B position, twinning reduces the strain of the shape change, thus, both stress and strain remain at a low level at this stage. From B to C, the temperature remains below M_f, while external stress is applied to deform the martensite. During this process, the twin interfaces move to accommodate the applied

stress. After the unloading of the external stress, a higher strain remains in the alloy, but the shape does not change, as shown in positions C to D in Figure 1.8. From D to A, the temperature increases above A_f, and all detwinned martensite completely transforms back to austenite, which completes a single OWSME cycle.

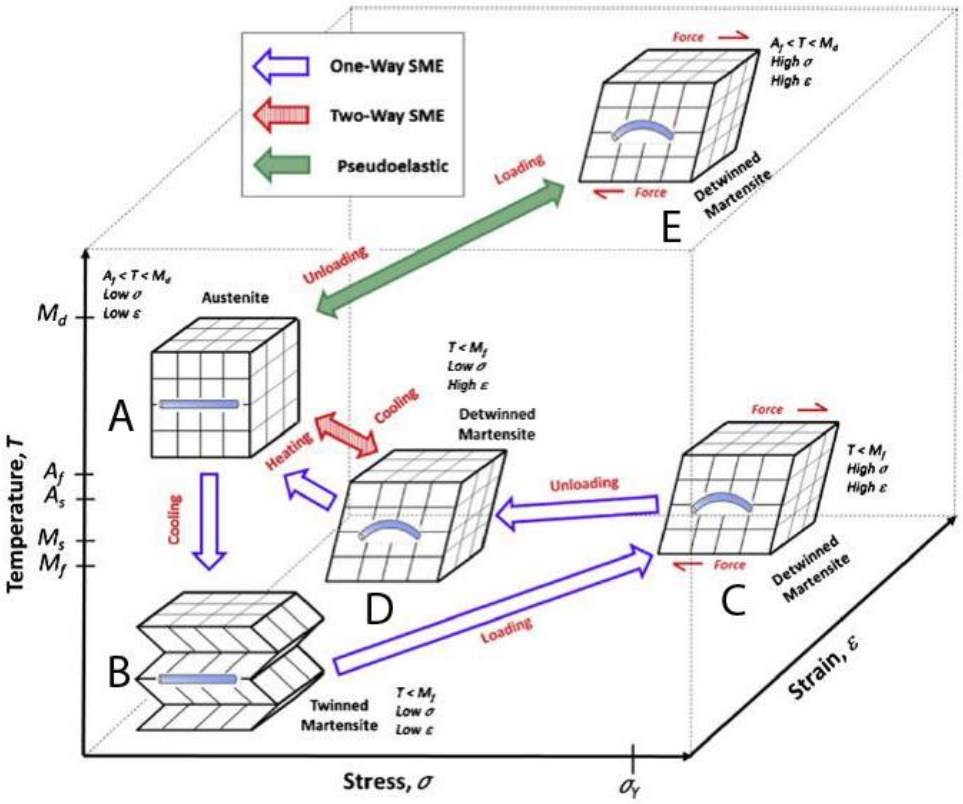

Figure 1.8 Shape and crystal structure changes in SMAs [15].

TWSME is a repeated cycle between positions A and D in Figure 1.8 as temperature changes. This process cannot be inherited directly from the alloy but needs a training process since the mechanism of TWSME is due to the influence of internal stress, which is usually obtained through dislocations or precipitates inside the alloy. To date, many different methods have been developed to obtain TWSME. In the conventional approach, the training process aims at introducing internal stress fields in the matrix by creating dislocations or precipitates since such internal stresses affect and control the growth of martensite variants during the phase

transformation. These training methods include stress cycling above the A_f temperature to reproduce the deformation that occurs during the stress-induced martensitic transformation; temperature cycling through the martensitic transformation under constant stress; and shape memory training which repeats the deformation cycle in a way that applies a stress to induce the martensitic transformation while heating under no stress to induce the reverse transformation back to austenite [37-39]. Later, new training methods were developed with different goals, such as martensite reorientation, which creates deformation in the martensite phase under stress [40], and constrained aging, which introduces aligned precipitates in the alloy [6].

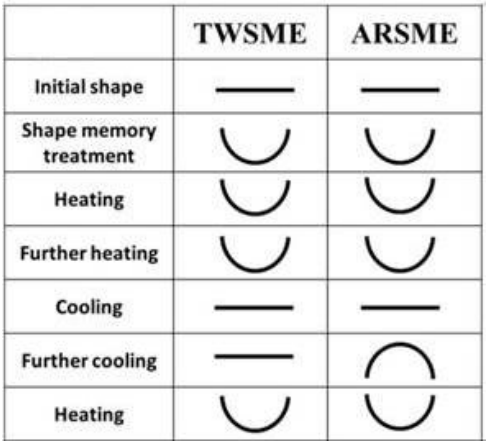

Figure 1.9 Schematic illustration of differences between TWSME and ARSME.

Among these novel training processes, constrained aging generates a special type of TWSME, which remembers the shape of the alloy in the austenite phase. When martensitic transformation occurs by decreasing temperature, the shape will change dramatically to the opposite side of the original form. Such a shape change can always be repeated in subsequent thermal cycles, and this special TWSME is called the all-round shape memory effect (ARSME). Figure 1.9 schematically illustrates the difference between TWSME and ARSME, which is the bending direction of an arc shaped stripe during further cooling. The first report of ARSME was found by Nishida and Honma [6], who observed an intermediate phase and precipitates at the same time, which they suggested were the reason for the ARSME. A later

study confirmed that the intermediate phase is the R phase and that precipitates are Ni_4Ti_3, which usually appear in Ni-rich Ni-Ti alloys after an appropriate aging treatment. As discussed in Section 1.2.1, Ni_4Ti_3 is a metastable phase that exists as precipitates in the Ni-Ti B2 matrix but never occurs as a bulk material. Strain fields exist around the Ni_4Ti_3 precipitates due to matrix-precipitate lattice mismatch [41, 42], and these strain fields lie at the origin of the ARSME. Applying external stress during the nucleation and growth of Ni_4Ti_3 could affect the isotropic orientation distribution of these precipitates, which is a coupling effect between the external stress and local strain around them and that leads to the final state of strain energy minimization inside the matrix [43]. As a result, the preferential orientation of the precipitates appears to fulfil the minimum strain requirement. This preferentially orientated growth of precipitates creates anisotropic internal strain, which finally controls the growth of martensite variants. In the case of ARSME, constrained aging is applied by bending Ni-Ti alloy strips, which causes a tensile stress on one side of the strip and compression stress on the other side. This overall anisotropic stress is caused by the different orientation distribution of precipitates, which are parallel to the stress direction in tension and perpendicular to the stress in compression. This distribution of precipitates eventually causes the shape change behavior that results in the ARSME [44].

1.3.2 Superelasticity

In solid state physics, elasticity is the ability of a body to resist a distorting influence or deforming force and to return to its original size and shape when that influence or force is removed. For most metals and alloys, 0.5% deformation is the maximum value that can be reached, but for SMAs, it is possible to reach up to 8% deformation without any irreversible deformation when the force is removed. Such extraordinary elastic deformation behavior in SMAs is called superelasticity. However, because the deformation mechanism is quite different between common materials and SMAs, this superelasticity is sometimes also known as pseudoelasticity because it is not the “real” elasticity observed in other materials.

Superelasticity is another manifestation of the reversible MT in SMAs, as shown in Figure 1.8. In the figure, the M_d temperature is the highest temperature at which martensite can no longer be stress induced; thus, above this temperature, SMAs will deform like ordinary metallic materials. When a SMA deforms below the M_d temperature, its typical stress-strain curve is shown in Figure 1.10. The structure starts as austenite upon loading, and when the stress is equal to $\sigma_{a\text{-}m}$, the martensite phase is initiated; this is the starting point of the martensitic transformation, which is shown as a plateau on the stress-strain curve. Austenite gradually transforms to martensite along this plateau since the applied stress remains stable while the strain gradually increases. At the end of the plateau, the transition from austenite to martensite is completed, and the martensite begins to deform elastically, which further increases the strain value. In the end, the maximum strain reaches a point where the martensite remains in the elastically deformed state. During unloading, the martensite first releases its elastic strain, and then the reverse transformation back to the elastically deformed austenite occurs after which the original shape is found again.

1.4 Ni_4Ti_3 precipitate

As discussed in Section 1.2.1, secondary phases can form in a Ni-rich Ni-Ti alloy with subsequent heat treatment after alloy fabrication, and which include Ni_3Ti_2, Ni_3Ti and Ni_4Ti_3. Among these phases, Ni_3Ti_2 and Ni_3Ti are normally incoherent with the alloy matrix and therefore have little contribution to the transformation process since they do not induce a particular lattice deformation or strain. The metastable Ni_4Ti_3 precipitates, however, can be coherent or semi-coherent with the B2 matrix, depending on their size, which greatly affects the MT process; thus, this precipitate has received special attention by researchers in view of the shape memory characteristics of the alloy.

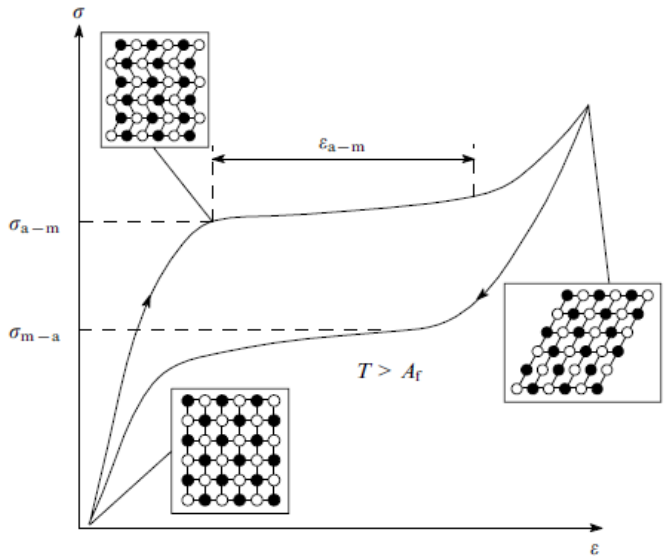

Figure 1.10 Stress-strain curve of a SMA with an illustration of the structure evolution during superelasticity [45].

1.4.1 Crystal structure and morphology

The crystal structure of Ni_4Ti_3 precipitates that is widely accepted is the one that was determined by Tadaki et al. and that has a rhombohedral structure with space group R-3 [46]. The lattice parameters are a=0.670 nm and α=113.9° in the rhombohedral coordinate system, as shown in Figure 1.11a, and in the hexagonal system, the parameters are a=b=1.124 nm and c=0.510 nm. The atomic positions were refined by Tirry et al. using advanced electron microscopy and which also better explains the specific lattice mismatch of the precipitates with the matrix than the original structure [47]. From observations with transmission electron microscopy (TEM), it was concluded that Ni_4Ti_3 precipitates have a lenticular shape and that different variants exist at the same time. The central plane of Ni_4Ti_3 precipitates is parallel to the crystallographic $[111]_{B2}$ planes in the B2 matrix; upon combining this with the space symmetry, there are a total of eight possible Ni_4Ti_3 variants. However, because two-by-two of these variants share the same habit plane, only four different orientation variants are typically considered, as shown in Figure 1.11b, c and d [47, 48]. Due to the orientation relationship with the matrix, a maximum of three variants are usually recognized in a single TEM image.

The orientation relation between one of the variants and the matrix is given as follows: $[100]_R$ // $[20\bar{1}]_{B2}$ and $(111)_R$ // $(111)_{B2}$.

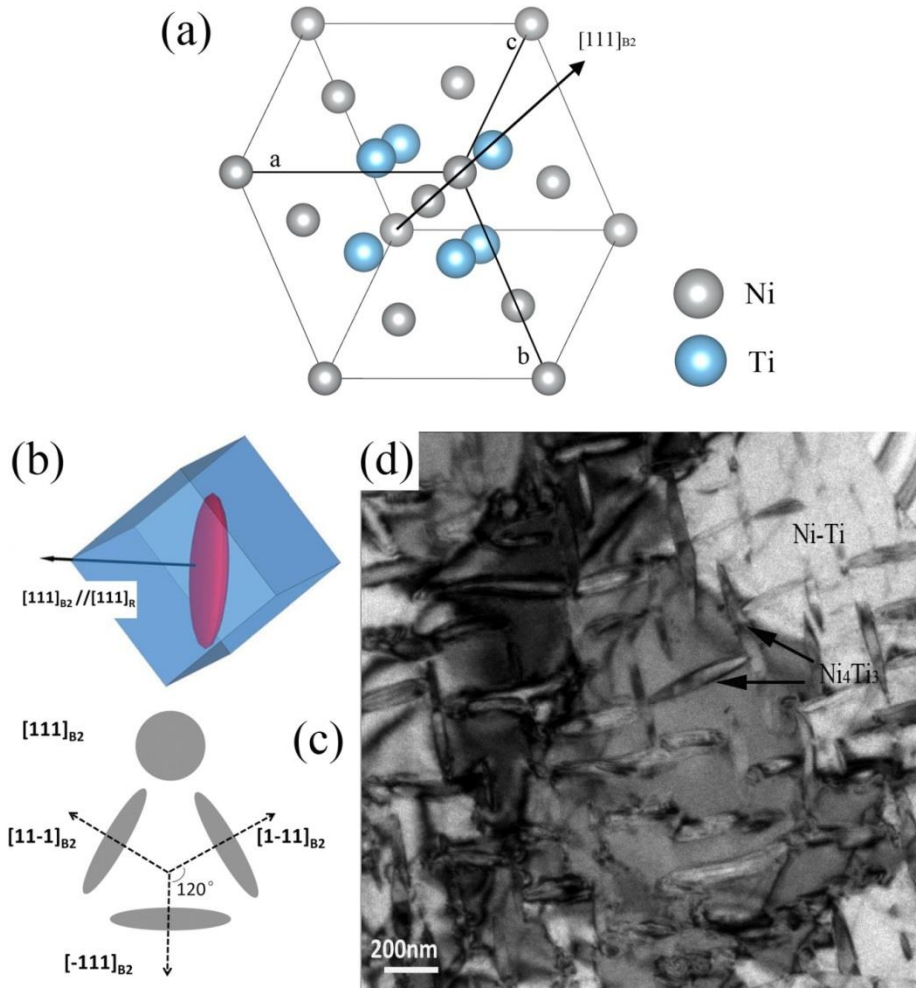

Figure 1.11 Schematic drawing of Ni_4Ti_3 precipitates: (a) rhombohedral unit cell of Ni_4Ti_3 in which the $[111]_{B2}$ direction is indicated by the arrow, (b) crystal relation with one variant and matrix [41], (c) cross-section drawing of the distribution along the $[111]_{B2}$ zone, and (d) typical TEM bright field image showing different variants of Ni_4Ti_3 precipitates.

The morphology of the lenticular shape of the precipitates can be explained by the lattice mismatch between the matrix and precipitates. This lattice mismatch is -3.1% along the $[111]_{B2}$ direction, which induces a tensile strain in the matrix, whereas along the perpendicular direction, the lattice mismatch is only 0.5%, which induces a compressive

strain in the matrix, as shown in Figure 1.12a (where the difference in lattice spacing is exaggerated in order to visualize it). The distribution of the matrix strains around the precipitates is thus anisotropic. As a result, along the $[111]_{B2}$ direction, the growth of precipitates is obstructed by the large strain induced by the large difference in the lattice parameter, whereas in the directions perpendicular to it, the growth is relatively easy due to the small strain and small lattice mismatch. This lattice mismatch and its induced strain fields in the surrounding matrix was quantitatively investigated by Tirry et al. [41], as shown in Figure 1.12b. Moreover, the strain fields surrounding the precipitates are one way in which Ni_4Ti_3 precipitates can affect the MT, as will be discussed in the following section.

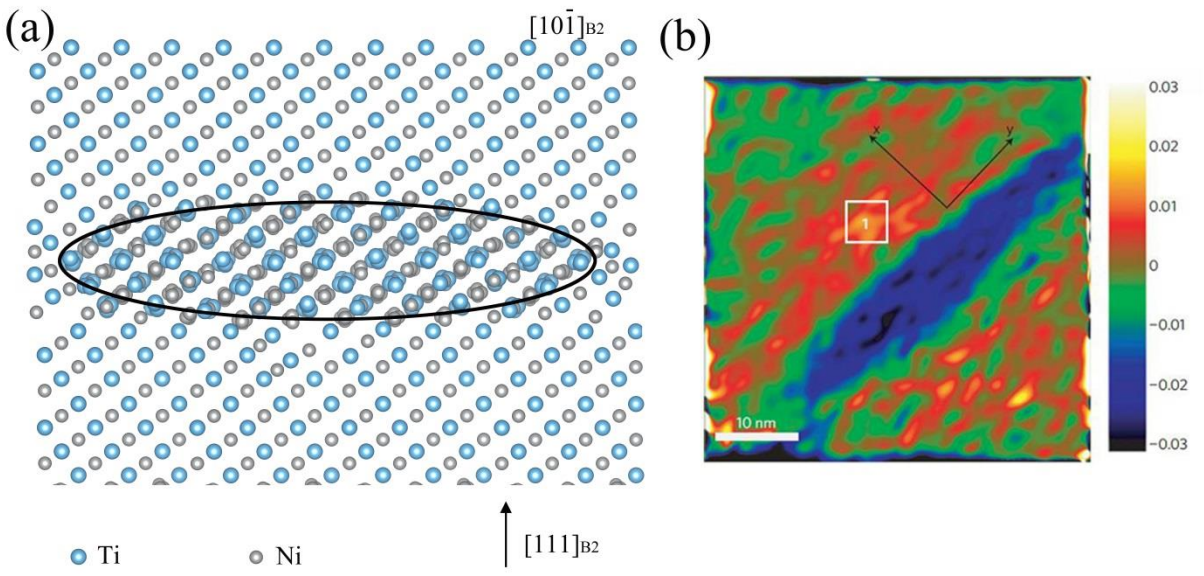

Figure 1.12 (a) An illustration of a coherent interface and resulting lattice distortion of the Ni-Ti $[10\bar{1}]_{B2}$ planes surrounding a Ni_4Ti_3 precipitate and (b) geometric phase analysis of the strain field gradient in the matrix surrounding a coherent Ni_4Ti_3 precipitate [41].

1.4.2 Growth of precipitates

Aging is considered a good way to adjust the MT performance of Ni-rich Ni-Ti alloys even after the alloys have been made, as first discovered by Horikawa et al. [49], even though the underlying mechanism was not clear at that time. They reported that there is an alternating

change in transformation temperatures when a Ni-rich Ni-Ti alloy is alternatively aged between two aging temperatures, whereas in equiatomic NiTi, such a result does not appear. A later study clarified that the results came from the equilibrium between the Ni-Ti matrix and the Ni_4Ti_3 precipitates because the appearance of the precipitates finely adjusts the composition of the Ni-Ti matrix, hence providing precise control of the transformation temperatures [50, 51]. Although Ni_4Ti_3 is considered a metastable phase compared with the equilibrium Ni_3Ti phase in the phase diagram, it is quite stable at temperatures below 600℃, and under normal aging conditions, only Ni_4Ti_3 is observed.

Many factors can affect the nucleation and growth of Ni_4Ti_3 precipitates; these factors determine the actual size, morphology and distribution of the precipitates. A higher Ni concentration in the alloy results in a higher supersaturation of Ni, which increases the nucleation rate and leads to a larger amount of precipitates. Apart from the composition, studies also show that the nucleation and growth rate are very different between the grain boundary and interior regions of the grains. The precipitates nucleate at the grain boundary regions prior to the grain interior because the nucleation barrier in the grain boundary region is reduced compared with grain interior region [52, 53]. However, if the alloy has a relatively high Ni concentration, the effect of the grain boundary will be significantly reduced due to the supersaturation of Ni; this indicates that different parameters always have combined effects on precipitates which will need to be studied very carefully.

Aging time and temperature are two other important parameters affecting the final appearance of Ni_4Ti_3 precipitates. Since the transformation temperature is very sensitive to composition, the aging process could easily change the transformation properties after alloy fabrication, and this process is performed via the fine tuning of the equilibrium state between the matrix composition and Ni_4Ti_3 precipitates. Different aging temperatures can lead to various sizes of Ni_4Ti_3 precipitates. Studies have already clarified that low temperature aging (473-623 K) introduces small (<15 nm) and densely dispersed coherent Ni_4Ti_3 precipitates,

which can improve the stability of the alloy during thermomechanical cycling by resisting the movement of dislocations. During this stage of aging, the formation of nuclei rather than growth of precipitates occurs, which enhances the shape recovery properties [54-56]. When the aging temperature is higher than 623 K and lower than 873 K, the size of precipitates increases as the aging time or temperature increase, which results in coherent or semi-coherent precipitates in the alloy. If the aging temperature exceeds 873 K, the precipitates can grow larger than 300 nm, in which case they will lose coherency with the matrix and form interface dislocations.

Recently, some research determined that an early stage growth of precipitates could be expected even at room temperature. In earlier studies it was considered that the aging temperature should not be lower than 470 K in order to induce the precipitation of Ni_4Ti_3; this conclusion was reached because precipitates were not observed in a $Ni_{50.9}Ti_{49.1}$ alloy quenched from 1070 K and aged at 373 K for 3000 h but were observed as tiny 2-3 nm precipitates in an alloy aged at 473 K for 100 h [57]. However, recently Kustov et al. observed that aging a sample at room temperature combined with differential scanning calorimetry (DSC) cycles suppresses the MT, which could be related to the initial stage or nucleation of precipitates [58]. A more systematic investigation was carried out by Wang et al. on a series of samples to test the effect of DSC cycling and room temperature aging [59]. They confirmed that room temperature aging needs to be followed with thermal cycling to suppress the MT, whereas room temperature aging alone has no effect on the transformation process. These samples were then investigated using TEM to check the atomic scale structural changes by Pourbabak et al. [60]. In their observed selected area electron diffraction (SAED) patterns, strong structured diffuse intensities condensed in periodic locations were observed, which revealed that microdomains exist in the form of needles of pure Ni atoms along the $<111>_{B2}$ directions. This could be considered as the initial formation of Ni_4Ti_3 precipitates since such precipitates contain 1 out of 7 [111] columns of pure Ni, which matches the needles concluded from the SAED results.

External stresses and strains could also affect the formation and growth of Ni_4Ti_3 precipitates. As discussed in Section 1.4.1, four orientational variants exist in the matrix when the alloy is aged without external stress, but when external stress is applied during the aging process, Ni_4Ti_3 precipitates will display preferential growth and a single variant will appear upon stress-assisted aging [43, 61-63]. This effect is due to the coupling between the local strain fields around the precipitates and the applied external stresses so that the precipitates are distributed to minimize the strain energy. This effect is used as an effective method to control the precipitate distribution, and one typical example is its application in the fabrication of ARSMAs.

In the case of ARSMAs, constrained aging is applied by bending Ni-Ti alloy strips, which induces tensile stress on one side of the strip and compressive stress on the other side. The tensile stress suppresses the formation of Ni_4Ti_3 variants in which the central plane is perpendicular to the stress direction, whereas the compressive stress favors the variants in this direction. Thus, the anisotropic stress in the final material is caused by the different orientational distribution of the precipitates, which are parallel to the stress direction in tension and perpendicular to the stress in compression. Such a distribution of precipitates eventually enables the shape change behavior that results in the ARSME [44]. Polycrystaline Ni-Ti alloy with strong texture further promotes the shape change behavior in the ARSME. Li. et al. has investigated that a $Ni_{51}Ti_{49}$ alloy obtained through rapid solidification followed by constrained aging treatment can induce the ARSME with very large deformation and narrow phase transformation temperature. Such property is appeared due to a strong $<001>_{B2}$ texture inside the alloy during rapid solidification process. The strongly textured structure limits the orientation of the grains and restricts the growth of Ni_4Ti_3 precipitates, which lead to the well-aligned Ni_4Ti_3 precipitates with dispersive distribution, eventually introducing strong internal stress fields around the precipitates [64]. Further understanding on the influence of constrained aging and texture will be studied in later chapers in this thesis.

1.4.3 Influence of Ni_4Ti_3 precipitates on the martensitic transformation

The existence of Ni_4Ti_3 precipitates can strongly influence the MT in different ways. On the one hand, it has been found that in a Ni-rich near-equiatomic Ni-Ti alloy, the M_s temperature is strongly dependent on the Ni concentration; increasing Ni causes a drastic decrease in the transformation temperature, as shown in Figure 1.13a [64]. When Ni_4Ti_3 is formed, the higher Ni/Ti concentration ratio in the precipitates will lead to the depletion of Ni from the matrix, as shown in Figure 1.13b, where the concentration gradients surrounding Ni_4Ti_3 precipitates in the matrix were quantified with analytical TEM [51]. This depletion of Ni in the matrix caused by Ni_4Ti_3 precipitates will eventually increase the transformation temperature. Because the aging treatment can determine the nucleation and growth of precipitates, it is possible to finely control the transformation temperature via different aging treatments. In this way, the transformation can be almost independent of the original nominal composition of the alloy but rather depends on aging parameters, which are easier to control in industrial productions.

On the other hand, the introduction of Ni_4Ti_3 precipitates could also affect the MT by changing the transformation path. In contrast to the B2-B19' transformation, a third intermediate R phase appears prior to the formation of B19' martensite when Ni_4Ti_3 precipitates are distributed in the matrix. The crystal structure of the R phase was introduced in Section 1.2.2. Due to the appearance of the R phase, a two-step B2-R-B19' transformation takes place instead of the original one-step transformation. This two-step transformation can be explained by the stress field around Ni_4Ti_3 precipitates in the matrix in coherent or semi-coherent cases. When changing from B2 to B19', a large lattice deformation is required due to the structure difference between cubic and monoclinic structures, while the lattice deformation is smaller when transforming from B2 to R phase, which means that the latter will occur first after which the R phase transforms into B19'. The precipitates themselves do not transform during R phase or martensitic transformation, but the strain they induce in the matrix thus favors the B2-R transformation.

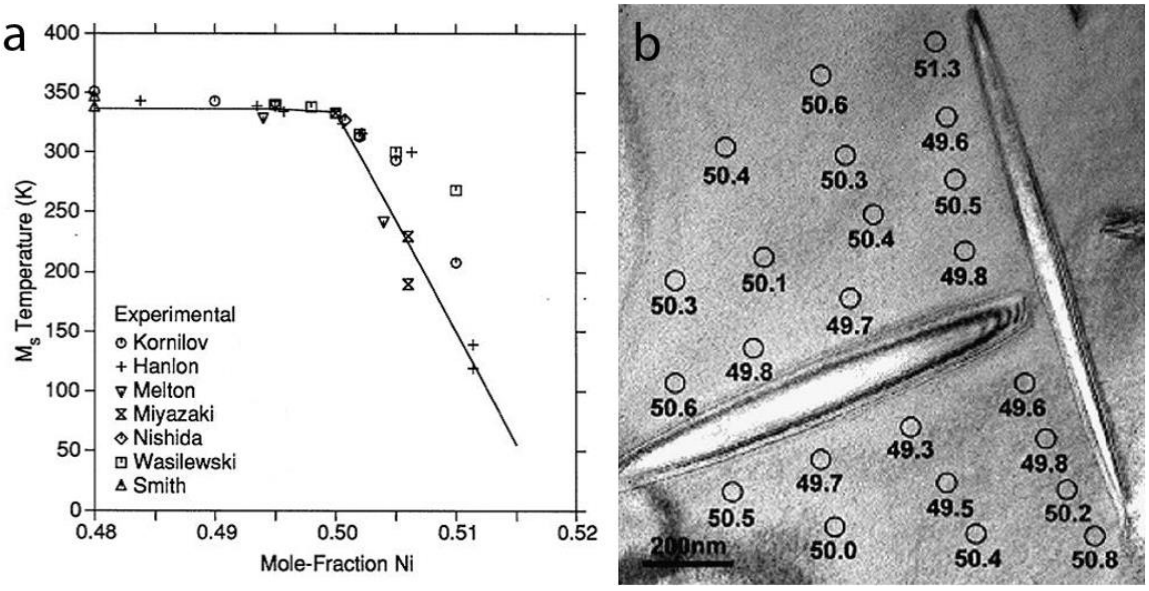

Figure 1.13 (a) M_s temperature as a function of Ni concentration for binary Ni-Ti alloys. Different symbols represent data from different authors. (b) Ni concentration gradient in the matrix surrounding two precipitates lying on two crossing $(111)_{B2}$ planes. Small circles and numbers show the measured position and the Ni concentration in atomic percent [51].

Similar to the B2-B19' transformation, the B2-R transformation also shows SME and superelasticity [65-68]. Moreover, when compared with the B19' transformation, the R phase transformation shows a very narrow hysteresis and high stability during thermomechanical cycling, which makes it more suitable for some practical applications.

From all of the findings above, it is clear that the presence of Ni_4Ti_3 precipitates in Ni-Ti alloys has a very important influence on the martensitic transformation. Their size, morphology and distribution may all affect the MT. A systematic quantitative analysis of Ni_4Ti_3 is necessary and helpful to connect different parameters for a better understanding and better control of alloy performance. This thesis will determine an effective approach to analyze the Ni_4Ti_3 precipitates in a more quantitative way and apply them to different kinds of materials, with the focus on the ARSME.

Chapter 2

Experimental methodologies

2.1 Transmission electron microscopy

2.1.1 Introduction

An electron microscope uses a beam of accelerated electrons as a probe to observe feature characteristics down to the nanometer scale. Such a high resolving power is achieved because the wavelength of an electron can be 100,000 times shorter than visible light photons. The wavelength of the source is the key parameter to determine the smallest feature that can be resolved, which is usually known as the resolution. According to different image collection methods, electron microscopy can be divided into transmission electron microscopy (TEM) and scanning electron microscopy (SEM). The theoretical origins of electron microscopy may date back to 1897 when J. Thomson first discovered electrons. In 1912, Lane discovered the phenomenon of X-ray diffraction, which established the wave property of X-rays and the method to use X-ray diffraction to determine the crystal structure of materials. In 1924, de Broglie determined that electrons had wave-like characteristics and that the wavelength of electrons is related to their energy. In 1927, Davisson and Germer confirmed the wave nature of electrons by an electron diffraction experiment. All these developments supported the possibility of using the electron as a new source to observe materials. In 1932, Ruska and Knoll developed the idea of electron lenses into a practical reality and demonstrated electron images taken on the instrument built by themselves in Berlin. This was a crucial step in the development of electron microscopy, for which Ruska received the Nobel Prize in 1986. Shortly after the invention by Ruska, Siemens and Halske started manufacturing commercial

transmission electron microscopes in Germany in 1939, followed by other companies, such as Philips (FEI/Thermo Fisher scientific), JEOL, and Hitachi after World War II.

Transmission electron microscopes and optical microscopes (visible-light microscopes) have a similar structure; in TEM, a beam of electrons is transmitted through a specimen to form an image. The electron beam is converged via an electromagnetic lens and then interacts with the specimen when the beam is transmitted through the specimen, during which an image is formed. The formed image is then magnified and focused onto an imaging device, such as a fluorescent screen or a sensor, e.g., a charge-coupled device (CCD). Figure 2.1 shows the internal structure of a conventional transmission electron microscope. The electron gun is on top of the microscope and emits an electron beam as the illumination source. The electron beam then passes through two condenser lenses, which converge the beam to reduce illumination loss. The convergence angle of the electron beam is controlled by changing the current of the lenses so that the beam could either be parallel or convergent, depending on the requirements. The beam then interacts with the specimen, and the electron wave affected by the specimen passes through the objective lens. The projection lenses magnify the image passed through the objective lens and project the image on the image recording system, which is a fluorescent screen or CCD, as mentioned before.

2.1.2 Interactions between materials and electrons

When an electron beam enters a specimen, there are a variety of possible interactions between the electrons and the atoms of the specimen. Figure 2.2 shows a brief diagram of these possible interactions. For a very thin specimen, many electrons can pass through the specimen without any interaction: these are referred to as unscattered electrons. The remaining electrons are scattered and can be divided into elastically scattered electrons and inelastically scattered electrons. These signals are used in the microscope to give detailed information about the specimen.

The elastically scattered electrons are those electrons that passed through the specimen and

interacted with the atoms yielding only a momentum transfer. These electrons carry only structural information about the specimen and they mostly contribute to conventional TEM including bright field (BF), dark field (DF) imaging and high resolution TEM (HRTEM) imaging. The inelastically scattered electrons have interacted with atoms yielding also energy transfer. The electrons transfer energy to the specimen in different ways such as phonon excitation, valance (energy band) excitation and inner shell ionization. Thereafter, the electrons exit the specimen carrying chemical information, meanwhile when an excited electron returns to its stable state, it generates secondary signals such as Auger electrons or X-rays. All these signals can be used for analytical microscopy such as energy dispersive X-ray spectroscopy (EDX) and electron energy loss spectroscopy (EELS).

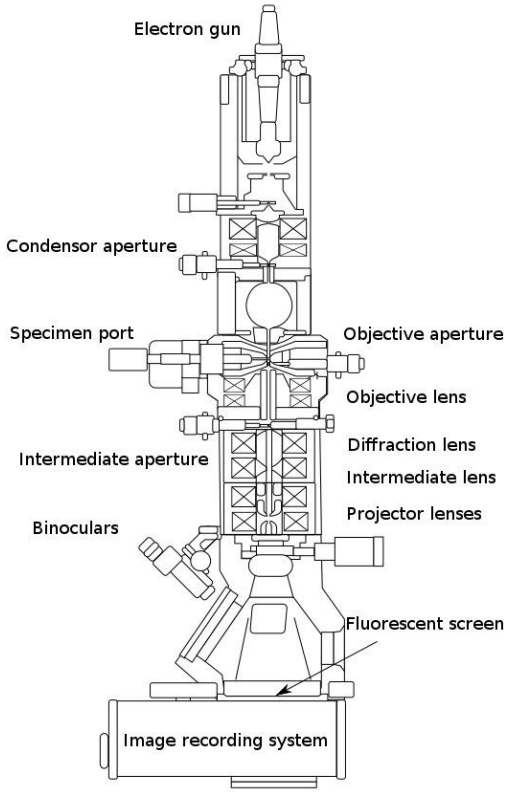

Figure 2.1 Schematic layout of the internal components in a basic transmission electron microscope [69].

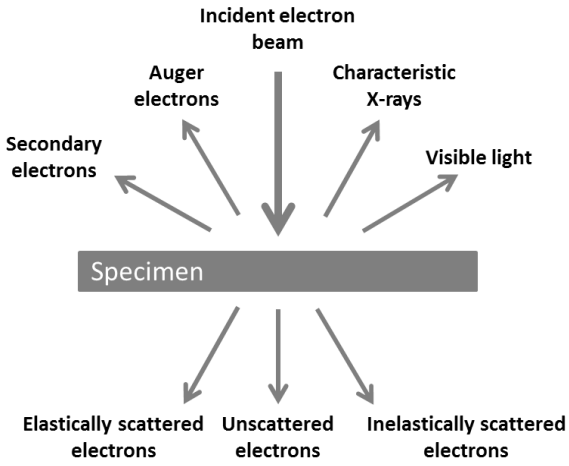

Figure 2.2 Simplified illustration of electron beam-sample interactions.

2.1.3 Diffraction

Electron diffraction is a consequence of the wave nature of electrons. When a near-parallel electron beam passes through the specimen in the microscope, the electrons are diffracted by the crystal lattice of the specimen following Bragg's law, which can be written as:

$$2d \sin\theta = n\lambda$$

where n is an integer and λ is the wavelength of the incident electron beam. The angle θ is known as the Bragg angle and defines the direction in which constructive interference of the diffracted waves can occur. The Bragg equation describes the geometric condition for diffraction to occur for a certain crystal plane (h k l) with interplanar spacing d, as indicated in Figure 2.3. According to Bragg's law, only certain scattering beams are allowed to diffract, which eventually forms the diffraction pattern at the back-focal plane of the objective lens. During the acquisition of diffraction in TEM, when the image plane of the intermediate lens is adjusted to the position of the back-focal plane of the objective lens, the diffraction patterns are recorded by a fluorescent screen or a CCD camera. The symmetry present in the diffraction pattern (DP) is related to the symmetry of the crystal, and the interplanar distances of the crystal determine the positions of bright spots in a given DP. Therefore, every DP corresponds to a certain orientation of a specific crystal, which means it is possible to

determine the space group, dimensions and even atomic site positions of a unit cell by observing the crystal structures along different crystal orientations in a tilting series. When a DP is directly observed by changing the intermediate lens position to the back-focal plane, the entire area of the specimen is illuminated with the electron beam. The DP observed in such a way is not satisfying because the TEM specimen is often buckled or twisted; moreover, the direct beam can be so intense that it could damage the viewing screen or saturate the CCD camera. Therefore, selected-area electron diffraction (SAED) is often used to obtain a DP from a specific small area of the specimen. A SAED is obtained with a reduced direct beam by inserting an aperture into the image plane of the objective lens and centering the aperture on the optic axis in the middle of the viewing screen.

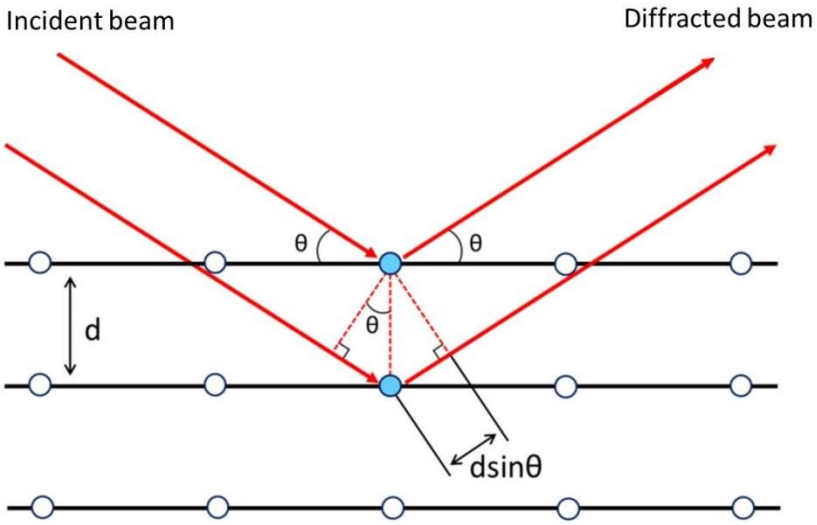

Figure 2.3 Schematic illustration of Bragg's law.

Different crystal structures can be readily distinguished with SAED. One typical example relevant to the present work is given in Figure 2.4, where the Ni-Ti B2 matrix, R phase and Ni_4Ti_3 precipitates are included. The very bright spots provide the crystal information for the Ni-Ti B2 phase, while small superspots indicate either the R phase or Ni_4Ti_3 precipitates according to their positions, which are indicated by the white arrows in the figure.

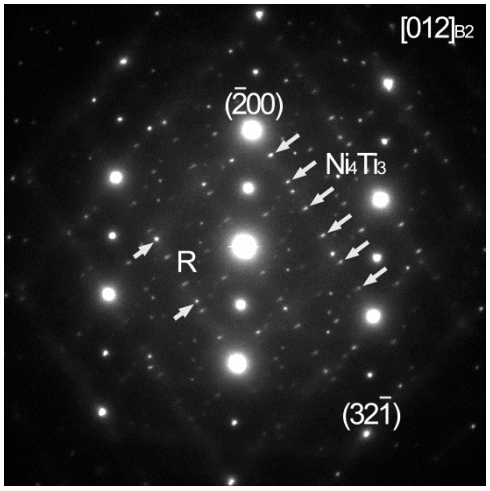

Figure 2.4 Example of a SAED pattern in $[080]_{B2}$ orientation, where the small superspots indicated by arrows originate from either R phase or Ni_4Ti_3 precipitates.

2.1.4 Conventional TEM

Due to the elastic scattering of the incident beam by the specimen, conventional TEM images can show different contrast types. The electron wave can change both its amplitude and its phase as it passes through the specimen and both changes can give rise to image contrast. The amplitude contrast includes mass-thickness contrast and diffraction contrast. The mass-thickness contrast is governed by the different scattering ability of different atoms and their integration from different thicknesses. The diffraction contrast is a special amplitude contrast where the scattering occurs only at Bragg angles. The phase contrast is from the interference of diffracted beams with different electron phase relationship.

The two most commonly used conventional TEM imaging modes are bright field (BF) and dark field (DF) imaging, which translate the electron scatter into interpretable amplitude contrast and allow the acquisition of real-space images of the specimen with different contrast. The selection of BF and DF images is based on the selection of the transmitted beam (undiffracted beam) or the diffracted beam, respectively, by placing an objective aperture at the respective position in the back-focal plane of the objective lens. Thus, these two imaging modes are also referred to as diffraction contrast imaging. In the BF image, the image is

formed by the transmitted beam (the objective aperture only includes the transmitted beam), which yields dark regions where the beam passes through a region where the orientation of the crystalline material satisfies the Bragg condition and the beam is diffracted away from the transmitted beam. For non-crystalline materials, the contrast of a BF image is influenced by the specimen thickness when diffracted electrons are shielded. In DF image mode, the image is formed by a diffracted beam, while the transmitted beam is blocked by the objective aperture. Thus, the regions that fit the Bragg condition of the selected diffracted beam have a brighter contrast in the image, while other regions remain dark. This mode is very useful to discriminate between different phases or to identify particular lattice defects in crystalline materials. Figure 2.5 is a typical example to use the BF/DF image to identify the nano-scaled Ni_4Ti_3 precipitates in a $Ni_{51}Ti_{49}$ alloy aged at 300 °C for 100 h. Since the size of the Ni_4Ti_3 precipitates in this alloy is below 10 nm, it is difficult to directly observe the precipitates in the BF image, as shown in Figure 2.5a. By selecting one of the reciprocal spots from the Ni_4Ti_3 precipitates in the SAED pattern as indicated in Figure 2.5b by a white circle, a DF image can be obtained which is formed by the used diffracted beam from the Ni_4Ti_3 precipitates, and in this DF image the Ni_4Ti_3 precipitates can be recognized more easily, as seen from Figure 2.5c.

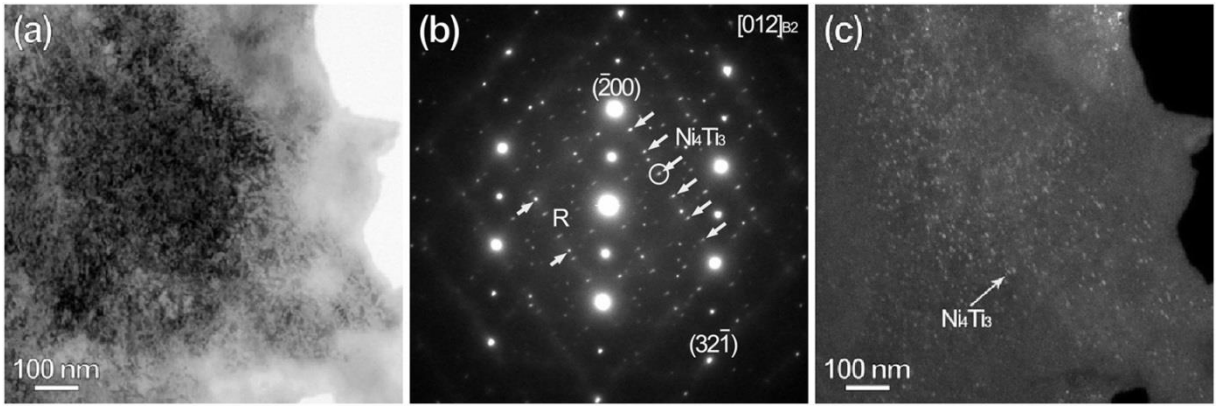

Figure 2.5 An example of conventional (a) BF and (c) DF images from a $Ni_{51}Ti_{49}$ alloy aged at 300 °C for 100 h. The DF image is taken with the reciprocal spot in the region indicated by the white circle in the SAED pattern in (b).

2.1.5 High resolution TEM

When increasing the magnification, very detailed information of the specimen can be observed as the viewing region decreases. The electron beam passing through the specimen contains both amplitude and phase information about the specimen and the diffracted beams will be further affected by the lens system. When several diffracted beams are allowed to interfere with each other, the final image is formed at the image plane of the objective lens and which reveals a two-dimensional view of the electrostatic potential of the atom columns in the specimen. Two atom columns or crystal planes can be observed separately when their spacing within the projected plane is larger than the point resolution of the microscope. Such images are called high resolution TEM (HRTEM) images. In conventional diffraction contrast imaging the electron phase information is lost, therefore, HRTEM is also referred to as phase contrast imaging.

Many factors related to the specimen and the lens system can influence a HRTEM image. The image changes for different thicknesses of the material as well as for different defocus values of the objective lens. One instance is that a white dot in a typical HRTEM image might represent the spacing between atomic columns but as thickness or defocus changes, it may be changed to represent the atomic columns itself. Moreover, the lens system in a microscope is not perfect with common aberrations such as spherical aberration (C_s), astigmatism, comma and chromatic aberration (C_c). The influence of comma and low-order astigmatism can be minimized by proper alignment, and in a normal uncorrected microscope, the major contribution that will affect the final image is the C_s aberration. This problem can be solved by using the C_s corrected microscope which can give rise to a significant improvement in point resolution.

2.1.6 In-situ TEM

Special holders have been developed that allow specimens to be modified (such as heated, cooled, strained, and twisted) inside the TEM during observation. Such holders have

expanded the possible states of materials available for observation in a TEM, and the experiments inside a TEM that use such special holders are referred to as in-situ TEM. In this study, in-situ heating and cooling holders are used so that the entire martensitic transformation process of a Ni-Ti alloy can be recorded during TEM analysis. An in-situ heating holder in a conventional TEM can go to ~1300°C, which is measured by a thermocouple attached to the cup. The holder is connected to a digital stage to manually control the temperature, and the holder can be double tilted during analysis. An in-situ cooling holder can reach the temperature of liquid N_2 by pouring liquid N_2 into the small Dewar at the end of the holder. The cooling holder is connected to a digital stage to manually control the temperature, and the holder can be double tilted during analysis. Specimen drift exists at the initial stage of temperature change in both heating and cooling holders, but the drift can be decreased to an acceptable level after a period of stabilization where a temperature change is controlled within a very small range.

2.2 Automated crystal orientation mapping in TEM

2.2.1 Introduction

During materials science studies, it is important to observe and characterize the crystal structures and phases at the atomic scale. Orientation and phase heterogeneity inside materials can lead to changes in the mechanical, physical or chemical performance via different microstructures, such as texture, boundary misorientations and twinning. Therefore, effective tools that can be used for the characterization of crystalline materials are widely embraced among researchers in materials science. A popular technique presently used to obtain orientation data is electron back-scatter diffraction (EBSD) which yields orientation imaging microscopy (OIM) (Adams et al., 1993) and is often installed on scanning electron microscopes [70, 71]. The EBSD technique acquires diffraction patterns from bulk samples in a SEM where the diffracting signal is composed of sets of Kikuchi lines because the relative positions of the Kikuchi lines are very sensitive to the crystal orientation. These signals can

be used to determine the crystal information with a rapid automated pattern analysis method [72]. EBSD collects crystal orientation and phase maps with a resolution of around 50 nm when a field emission gun is used. There are some restrictions to the EBSD method when it is used for materials analysis. The first restriction is that the quality of the Kikuchi patterns is known to be very sensitive to the surface roughness; hence, efficient mapping results require well-polished samples. The second limitation is that the Kikuchi lines disappear when there is a high level of strain and internal stress, which means that EBSD cannot resolve materials with internal stresses and strains, such as severely deformed metals. Moreover, there is a growing need for the orientation and phase characterization of materials at high resolution, such as nanocrystalline materials or small precipitates inside the materials. Consequently, an attempt to obtain orientation mapping results was extended from SEM to TEM, since in TEM, Bragg diffraction spots can be used to extract the orientation information at a much higher lateral resolution compared to the EBSD method in SEM.

The technique of Automated Crystal Orientation Mapping in TEM (ACOM-TEM) was developed to have a similar approach as EBSD but is applied on a TEM and can be used to gain crystal orientation mapping in cases where the detail cannot be resolved by EBSD in a SEM. This technique has been given different names in the literature (PACOM[73], IFPOM[74] and D-STEM/PED[75]), but these days two names are mostly used: ACOM-TEM and ASTAR^{TM}, the latter one is the commercial name of the product provided by NanoMEGAS. The ACOM-TEM collects DPs as an interesting alternative to the collection of Kikuchi lines to extract the relevant crystal information of the material in combination with recently developed computer indexing routines [76, 77]. A current ACOM-TEM system combines an electronic hardware component connected to the coils of the transmission electron microscope, which scans the nanofocused electron beam over the sample in diffraction mode, yielding a high throughput of DPs with nm resolution, and these DPs are collected by an external high-speed camera. A software tool matches the observed DPs for each scan point or pixel with a precalculated set of (kinematical) diffraction

templates for a known phase by simple cross-correlation techniques and produces phase and orientation maps of the nanograins in the entire sample, up to several microns in lateral size and including basic grain statistics and reliability information.

2.2.2 Precession electron diffraction

Because the ACOM-TEM uses DPs as the main input to obtain orientation and phase maps, it is important to obtain DPs with very high quality. A technique referred to as precession electron diffraction (PED) can be used with ACOM-TEM to improve the quality of the DPs. The PED technique was first proposed by Vincent and Midgley in 1994 [78]. When DPs are collected using precession, the incoming electron beam is precessing on a cone surface; as such, the diffraction intensities are summed over a large number of slightly deviating beam orientations, which increases the number of reflections that can be used for template matching [79]. Figure 2.6 shows a schematic diagram of precession diffraction. During precession, the incident beam is double-deflected using the usual DF scan coils in a circular hollow (radius G and angle C) about a centered zone-axis direction and the beam is de-scanned onto the back focal plane where the DP is observed [80]. A spot pattern obtained by PED looks like a conventional SAED pattern, but it results from a successive integration of the diffracted intensities passing through the Bragg condition. In comparison with conventional SAED, PED has several advantages [79, 81]:

- Multiple beam dynamical diffraction effects are reduced, especially those interactions that involve non-systematic inelastic scattering such as Kikuchi lines. This is because the diffraction patterns are collected while the electron beam is precessing on a cone surface, which means that only a few reflections are simultaneously excited and, therefore, dynamical effects are strongly reduced.
- The sensitivity to crystal orientation is reduced because integrated PED patterns can be obtained even if the crystal is not perfectly aligned along a particular zone axis.

- The PED technique can be applied to crystals with a thickness up to approximately 100 nm, because the obtained intensities resemble kinematical diffraction and are approximated by a kinematical expression in the simulation package.

The influence of precession on the study of Ni-Ti alloys in this thesis are discussed in detail in Chapter 3.

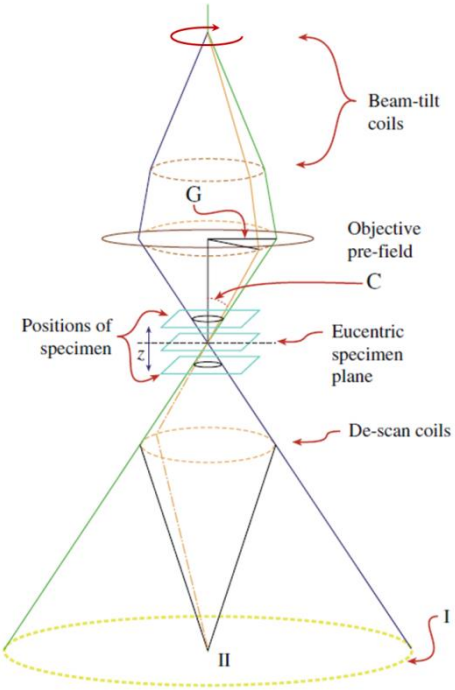

Figure 2. 6 Schematic diagram for precession diffraction [80].

2.2.3 Data acquisition

Figure 2.7 briefly shows how ACOM-TEM collects crystal orientation data in a TEM. The region of interest is first observed in the TEM (Figure 2.7a), and then an array of electron diffraction spot patterns is collected by controllably scanning the beam over the desired region, possibly including precession (Figure 2.7b). The DPs are collected sequentially with an external CCD camera that is installed in front of the TEM viewing screen (white arrow in Figure 2.7c). Both the scanning process and precession of the electron beam are controlled by the dedicated digital "DigiSTAR" unit, which is connected both to an operational computer and the microscope (Figure 2.7d). The connection to the microscope is achieved via adequate

connections to the deflector coils control boards, so the TEM does not need to possess scanning facilities itself. During the scanning of the primary electron beam, thousands of DPs are recorded and stored in the memory of the computer.

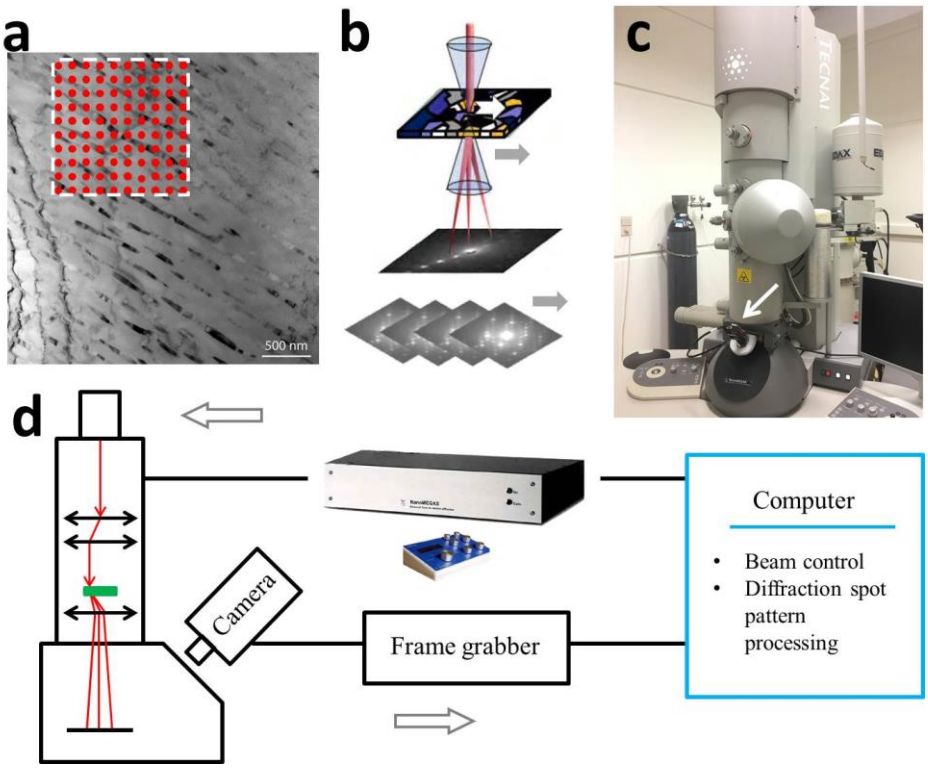

Figure 2.7 Experimental apparatus for ACOM-TEM. (a) The region of interest is scanned and (b) the spot diffraction patterns are collected with (c) an external CCD camera; the beam movement (d) is combined with precession with the help of the "DigiSTAR" device.

2.2.4 Template matching

Determining the correct crystal orientation or phase information directly from a particular DP is quite difficult, even for a single crystal, because there may be several solutions. Such a difficulty is mainly related to the symmetry problem, as there can be several solutions for a given set of angles and distances between diffracting beams. Confirming or dismissing them must use further information from the patterns, and for multiphase materials, the situation is even more complicated due to the variety of possible angles and distances. While it is rather

difficult to directly identify the exact orientation (especially for non-zone directions) or the phase of the crystal according to a given DP, it is easy to calculate the DP for a known orientation or phase. Thus, the basic way to determine the orientation and phase information with ACOM-TEM is to perform a matching process by comparing the collected DPs with preset DP templates to identify the proper orientation or phase, as shown in Figure 2.8. Figure 2.8a shows the DP collected by ACOM-TEM. The original images collected by the camera are distorted because the ACOM-TEM camera collects data from the small viewing screen in the microscope that is not perpendicular to the electron beam but has an angle of approximately 45°. Therefore, a calibrated distortion correction process is conducted before the matching process. Figure 2.8b shows the simulated diffraction template(s), which can be generated in advance and imported into the software for matching. Figure 2.8c shows a local correlation index map, which is normalized by the maximal encountered correlation index. The map is viewed before the automatic matching procedure starts, which can help to determine the distortion correction of the images and the recognition of the diffraction spots, which affects the matching quality when the automatic matching procedure starts. The map displays the correlation indexes as a grayscale, where the darkest point in the map corresponds to the selected orientation.

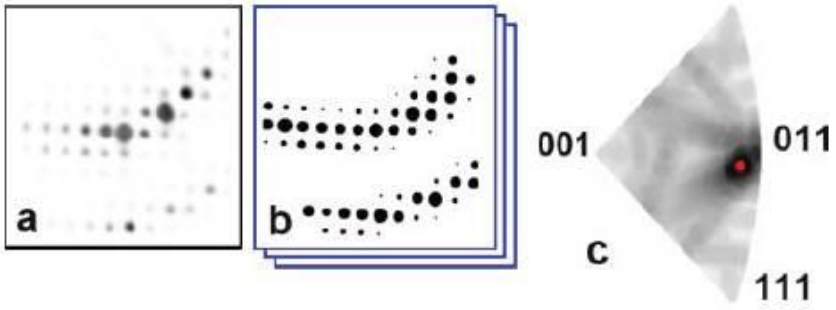

Figure 2.8 Indexing process carried out by cross-correlating (a) the experimentally acquired DPs with (b) the preset simulated diffraction templates for all possible crystal orientations and phases. (c) The quality map shows the degree of matching between experimental DPs and simulated patterns by displaying the relative values of the correlation indexes for all possible orientations as a grayscale [82].

2.3 TEM sample preparation

Materials investigated by TEM need to be electron transparent to be properly observed; thus, the thickness of TEM specimens should be thin enough to allow electrons to pass through them. In the case of conventional TEM and when dealing with most solid state materials, the thickness should be less than about 100 nm, and in the case of HRTEM, the thickness ideally should be even less than 30 nm. Different methods exist to obtain the expected thickness for different types of materials. Because this study is mainly focused on metallic SMA, the TEM specimen preparation methods for metallic materials are introduced in this chapter.

Most contemporary TEM holders adapt disk-like specimens and grids with a diameter of 3 mm. For bulk metallic materials, a 3 mm disk can be obtained by mechanical cutting and grinding. After the disc is mechanically thinned to approximately 100 μm, a final thinning process, such as electropolishing, Ar^+ ion milling or focused ion beam (FIB), can help to reach electron transparency.

2.3.1 Electropolishing

Electropolishing is a final thinning method that is only useful for electrically conductive materials, such as metals and alloys. This method has the advantage that it can produce thin electron transparent regions without any mechanical or ion damage, while the disadvantage of this method is that residual electrolyte may contaminate or even change the surface chemistry of the specimen due to insufficient cleaning right after the electropolishing step; another disadvantage is that the orientation of the TEM specimen that can be obtained is restricted by the shape of the bulk sample and following cutting methods, which cannot always be controlled.

The basic working mechanism of electropolishing is a dual electrolyte jet that is pumped onto both sides of the disk specimen via a twin-jet apparatus, where the sample acts as the anode and held in a Teflon container in between the jets. A voltage is applied to the specimen, and

the current caused by anodic dissolution of the specimen creates a polished surface rather than etching or pitting the specimen, as shown in Figure 2.9a. A laser beam or light sensor is used to detect transparency and provides a warning by sound when perforation occurs. At this warning, the electrolyte flow is cut off automatically to prevent the loss of thin regions around the perforation of the specimen. At this stage, the disk must be rapidly extracted from the electrolyte and washed in a solvent to remove any residual electrolyte film that may etch or pollute the surface [80].

Many factors can affect the quality of the specimen during electropolishing, such as the applied voltage, polishing current, flow rate, photo-sensitivity, temperature, and electrolyte solution chemistry. This study uses a mixture of 80% methanol and 20% sulfuric acid as the electrolyte solution. For Ni-Ti alloys, the electrolyte solution of methanol and sulfuric acid can obtain excellent electropolishing quality and thin regions, but the Ni_4Ti_3 precipitates are thinned faster than the Ni-Ti B2 matrix at 10°C. Thus, the electropolishing process was operated at a temperature of approximately -15°C because a low temperature decreases the preferential thinning of the precipitates and provides better results. During electropolishing, an appropriate value of the applied voltage and current is very important to ensure the polishing process instead of etching or pitting, as shown in Figure 2.9b. The current used in this study was optimized to be approximately 135 mA, and the corresponding applied voltage to generate this current for Ni-Ti alloy was approximately 20 V.

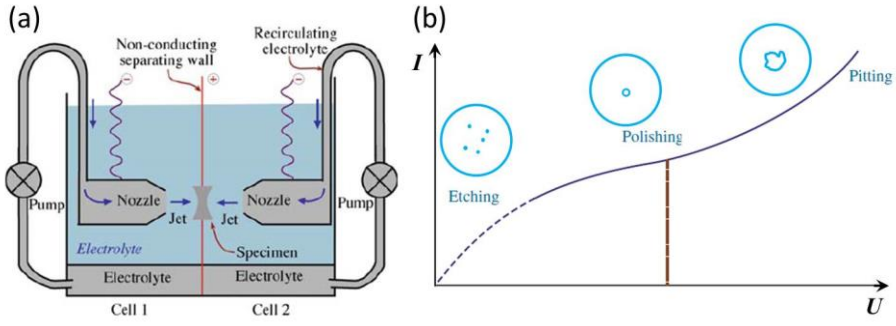

Figure 2.9 (a) Schematic drawing of a twin-jet electropolishing instrument [80]. (b) Electropolishing curve showing the increase in current between the anode and the cathode as the applied voltage is increased.

2.3.2 Focused ion beam

A FIB has a similar construction as a SEM but instead of using an electron beam as in SEM, a finely focused ion beam is used. The ion beam source is usually Ga^{+}, and the beam size is in the range of 1000 nm to 5 nm. The primary aim of most FIBs is to use the beam for material etching or material deposition, but it can also be used for imaging. However, since the ion beam is very destructive and provides a low resolution for imaging compared to an electron beam, most systems incorporate both an electron beam and an ion beam, which is then known as the FIB/SEM dual-beam system. Figure 2.10 briefly shows the structure of a dual beam system, where an electron beam column is vertically aligned in the system and an ion beam column is placed at 52° to the electron beam column. During the analysis process, the sample is placed at the cross point of the two beams, and the sample stage can rotate to the place where the sample is either perpendicular to the ion beam for cutting or perpendicular to the electron beam for better viewing.

Figure 2.10 Schematic illustration of FIB/SEM dual beam system [80].

FIB can be used to prepare TEM specimens with many different shapes as required. Figure 2.11 shows one typical TEM specimen preparation process, which is called in-situ lift-out specimen preparation. In this thesis, all FIB specimens are obtained by this method. The detailed process of this sample preparation method is shown in Figure 2.11. The first step is to find the region of interest and then deposit a Pt protective layer on the region where the

TEM lamella is going to be prepared, which is shown in Figure 2.11a. The Pt layer is very important to protect the sample from ion damage in the subsequent milling process. The second step is to mill trenches around the deposited region so that the shape of a TEM lamella forms, as shown in Figure 2.11b. The next step is to insert a microneedle for sample manipulation. The needle is glued to the lamella by Pt deposition at the edge of the lamella, and after deposition, the lamella is released from the bulk sample by cutting the other three sides, as shown in Figure 2.11c. After this step, the lamella is already separated from the bulk sample and is supported by the microneedle. Then, the lamella is lifted out from the bulk sample and moved to a grid where the sample is placed, as shown in Figure 2.11d. As the lamella touches the grid, Pt deposition glues the lamella to the grid, as shown in Figure 2.11e. After that, the connection of the microneedle and the lamella is cut off, and the final thinning process of the lamella starts. The thinning must be taken step-by-step on both sides of the lamella, and the final thinned FIB specimen can reach a thickness of approximately 50 nm, as shown in Figure 2.11f.

Compared to electropolishing, FIB has the advantage that the desired crystal orientation of the TEM specimen can be obtained easier because when selecting the region of interest, the sample stage can rotate on several axes to enable the selection of a specific direction. This advantage is very useful in the study comprising this thesis, and most of the TEM specimens which were aged under external stress used in Chapter 4 are obtained in this way with a special orientation to the bulk samples. The disadvantage of FIB for TEM specimen preparation is that ion beams can induce unavoidable defects to the material during milling, such as Ga-ion implantation and dislocations. Thus, it is better to select the proper sample preparation method depending on the desired information that needs to be obtained from the experiment.

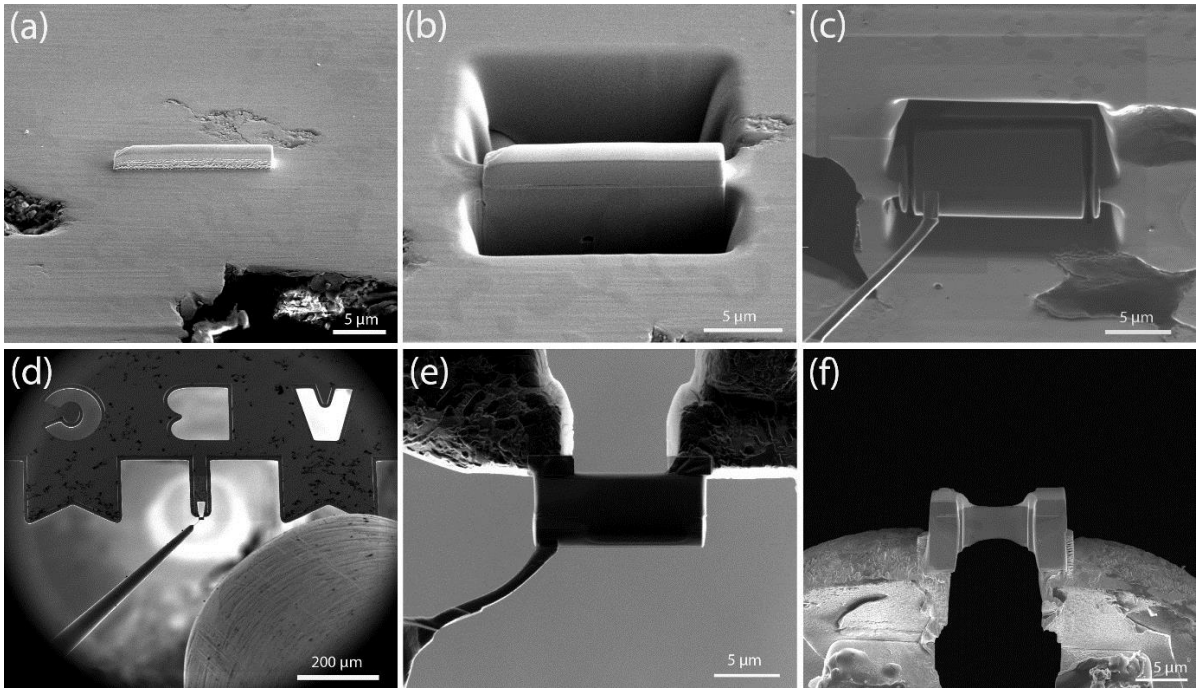

Figure 2.11 Illustration of FIB sample preparation by in-situ lift-out technique. (a) A protective Pt layer is deposited on the region of interest. (b) Trenches are milled around the lamella. (c) The microneedle is glued to the lamella, and the lamella is separated from the bulk material. (d) The lamella is lifted out from the bulk material and moved to the grid. (e) The lamella is glued to the grid. (f) The finished FIB specimen.

2.4 Geometrical phase analysis (GPA)

The geometric phase analysis (GPA) is an image processing technique which can be applied to HRTEM images to quantitatively extract information about the local two-dimensional displacement. In principle, this method could be applied to any type of lattice/fringe image, like off-axis HRTEM fringes (as in this thesis), HRSTEM image and the reconstructed exit wave lattice image etc. The basic idea behind the GPA method is that the displacement in the image at a certain point is equivalent with the geometrical phase in the same point. The displacement can be obtained from the inverse Fourier transform produced by selecting a Bragg spot in the Fourier transform of a HRTEM image. A lattice image I(r) can be expressed by the sum of inverse Fourier transform of the Bragg "spots", ***g:***

$$I(\boldsymbol{r}) = \sum_{g} H_g(\boldsymbol{r})\exp(2\pi \boldsymbol{i}\boldsymbol{g} \cdot \boldsymbol{r})$$

The integration of inverse Fourier transforms becomes a summation because images are always composed of discrete pixels. Each Fourier coefficient stands in the real space for a set of lattice fringes, which can be treated as a position dependent amplitude and phase component. Thus, the inverse Fourier transform of a single Fourier coefficient can be defined by

$$H'_g(\boldsymbol{r}) = A_g(\boldsymbol{r})exp\left[2\pi \boldsymbol{i}\boldsymbol{g} \cdot \boldsymbol{r} + iP_g(\boldsymbol{r})\right]$$

The phase component $P_g(\boldsymbol{r})$ here is called the geometric phase, because it is obtained from the raw-phase image by subtracting the factor $2\pi \boldsymbol{g} \cdot \boldsymbol{r}$ and it describes the position dependent lattice deviation. If there are local deviations of the spacing between the lattice fringes, there will be changes to the geometric phase which can be visualized and interpreted [83]. A standard procedure of GPA analysis is as follows: the first step is to calculate the Fourier transform of the input image. Second, select and mask a reciprocal fringe vector **g´** (i.e., the "averaged" **g** of the whole image) with a mask function. After performing the inverse Fourier transform of the mask filtered image, the amplitude and phase component are extracted. The amplitude component is an envelope to the Fourier coefficient and it will be discarded in the following procedure. The raw phase component **g´** contains an average effect of the masked pixels. A more accurate value of the vector **g** can be calculated by selecting a reference area in the image and by minimizing with respect to **g** [83, 84]. In other words, the phase image is refined in such a way that the selected reference area has a zero geometric phase. Such a refinement is important in GPA as it returns the accurate **g** vector for further calculations. Afterwards, the strain is calculated from the derivatives of the phase image. The final results obtained after the GPA analysis are coloured maps, which will show the two-dimensional ε_{xx}, ε_{yy} and $\varepsilon_{xy}=\varepsilon_{yx}$, respectively the strain along the *x* and *y* axis and the shear strain.

Chapter 3

Optimization of automated crystal orientation mapping in a TEM for Ni_4Ti_3 precipitation in all-round Ni-Ti shape memory alloys

3.1 Introduction and material preparation

3.1.1 Introduction

The attempts for finding new applications of Ni-Ti alloys are still continuing even after half a century's investigations of this material. In the present work, we have focused on the characterization of a type of Ni-Ti SMA which is aimed to be used as an artificial sphincter for human implantation. Such a sphincter assists the opening and closing of veins, bowels, etc. as shown in Figure 3.1 [85]. A Ni-Ti artificial sphincter will have several advantages over existing ones which use conventional materials and a complicated control system. These advantages include good corrosion resistance, good implantation tolerance, simple structure and easier controllability [86]. The design is based on the all-round shape memory effect of Ni-Ti which was first reported by Nishida and Honma [6]. As already mentioned in chapter 1, the ARSME is actually a special and remarkable case of the TWSME describing the behaviour of an alloy which remembers one shape in its parent phase and the shape will dramatically change to the opposite side when temperature decreases to below the phase transformation temperature, as shown in Figure 1.8 in chapter 1. The ARSME effect can always be repeated in following heating and cooling processes after proper treatment of the alloy. Similar to conventional TWSME, the mechanism of ARSME effect is mainly

controlled by the existence of Ni_4Ti_3 precipitates in the Ni-Ti alloy [44].

The effect of Ni_4Ti_3 precipitates on the ARSME is mainly due to the particular growth and orientation of the precipitates during the training process. The sample experiences various types of loading in different regions during bending [53, 87], i.e., a tensile stress on the upper side and a compression stress on the lower side. The difference in stress direction directly causes a difference in preferential orientation of the Ni_4Ti_3 precipitates and these differences will contribute the ARSME effect by controlling the phase transformation. Therefore, a good characterization tool can lead to a better understanding of anisotropic precipitation mechanisms in this alloy which can improve functional properties of the material.

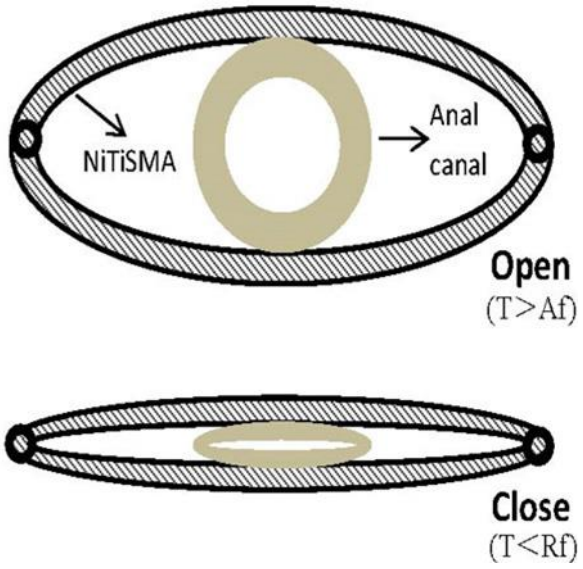

Figure 3.1 An illustration of an application of Ni-Ti as artificial sphincter [85].

In this respect TEM is capable of reaching the needed magnifications and resolution, as well as obtaining information in the real and reciprocal space for observation of the precipitates. Unfortunately, current day TEM data is often limited to averaged information over large numbers of (nano) grains as obtained by wide-beam diffraction techniques or to detailed atomic scale data on a few grains or selected defects as obtained by high-resolution imaging techniques. There is thus often a gap in information between the very small atomic scale and the potentially rather large unit containing the nanofeatures or crystallographic defects. As a

result, there is a risk of missing the important scale of configurations of nanofeatures appearing in many of today's advanced materials. Moreover, although the obtained data on individual grains or defects can be extremely detailed these days, the lack of good statistical information often leads to severe oversimplification when the observed nano/microstructure needs to be correlated with the functional and mechanical properties acting at higher length scales.

This current problem for TEM can be overcome using recently introduced Automated Crystal Orientation and Phase Mapping [79] method revealing the grain-by-grain configurations of nanofeatures in large regions. As already introduced in chapter 2, this method is comparable to, e.g., micro-scale Orientation Imaging Microscopy (OIM) as obtained using EBSD in a SEM. The application of such techniques in the TEM, however, provides a leap in resolution down to the nm scale, opening a whole new field of innovative research. Moreover, along with automated OIM comes a variety of nanostatistical methods, which yield quantitative information never obtained before at this length scale and working speed.

In this work, ACOM-TEM was used as the main method for the investigation of Ni_4Ti_3 precipitates in the Ni-Ti alloy and different parameters of this technique were optimized. Despite the fact that already a large amount of research has been done on Ni_4Ti_3 precipitates, quantitative information such as size, distribution, orientation, etc. of ensembles of nanoscale Ni_4Ti_3 precipitates at larger scale is still missing in the literature. Since this is the first attempt to apply this technique on precipitates in Ni-Ti alloys, the initial goal in this part is the optimization of experimental and computational ACOM-TEM parameters to obtain more reliable data to identify and quantify the different phases in Ni-Ti alloys, with the emphasis on the Ni_4Ti_3 precipitates. In the end also some concrete results will be presented with respect to the actual sample under investigation.

3.1.2 Material preparation

The alloys used in this study were prepared from electrolytic nickel (purity ≥ 99.9%) and

titanium sponge (purity ≥ 99.7%) through arc melting followed by rapid solidification via suction casting. The as-casted alloy stripe has a size of 70×8×0.5 mm^3 and a nominal composition of Ni51at%-Ti. A solid solution treatment was applied to homogenizing the composition at 850°C for 3h under Ar (purity 99.9%) protective atmosphere and followed by water quenching. After solid solution, the alloys went through the aging treatment at 400 °C for 100h to introduce the Ni_4Ti_3 precipitates in the alloys.

In the present work, a Tecnai G2 microscope equipped with a FEG with a minimum spot size of 1.6 nm for the 20 μm condenser aperture and selecting the microprobe mode has been used. From the data acquired by ACOM-TEM, orientation as well as phase maps can be obtained together with quantitative information of precipitates such as size, distribution, volume fraction etc.

3.2 Optimization of ACOM-TEM

3.2.1 Optimization method and extraction of quantitative data

As discussed in chapter 2, the application of ACOM-TEM is based on obtaining and identifying a series of diffraction spot patterns collected from a region of interest, so the whole process includes two parts: DP acquisition and indexation of collected DPs. Thus, the reliability of the final results is based on that of the separate steps and their combination. In most cases, the default settings of the ACOM-TEM technique are sufficient to obtain proper orientation and phase maps. However, the present Ni-Ti alloy proved to be more demanding case, for several reasons.

In the present $Ni_{51}Ti_{49}$ sample, the area of interest contains both Ni-Ti B2 matrix and Ni_4Ti_3 precipitates. The reciprocal space of the B2 matrix is that of the common body centred cubic structure but without systematic extinctions due to the ordering of the two kinds of atoms. The reciprocal space of Ni_4Ti_3 precipitates which has rhombohedral structure shares several basic reflections with that of the Ni-Ti B2 matrix, but rows of superspots appear in between

the basic reflections along the $<321>_{B2}$ directions and dividing the length of this vector into seven equal parts [46]. In other words, in kinematical conditions these superspots are the only sign to distinguish between the B2 matrix and precipitates, and for nanoscale precipitates these superspots have very weak intensity.

Since the final orientation and phase maps are a combination of both experimental data acquisition and calculation of templates, multiple parameters have to be taken into account in order to optimize the ACOM-TEM technique. At first, the software automatically provides a so-called degree of matching parameter Q_i introduced to characterise the overall correlation index for a given diffraction template *i*. The software uses this parameter to determine the best template calculated with fixed settings to match with a given DP taken under fixed conditions:

$$Q_i = \frac{\sum_{j=1}^{m} P(x_j,y_j)T_i(x_j,y_j)}{\sqrt{\sum_{j=1}^{m} P^2(x_j,y_j)}\sqrt{\sum_{j=1}^{m} T_i^2(x_j,y_j)}} \quad (1)$$

where P(x,y) is the intensity function which represents the values from the experimentally collected data and $T_i(x,y)$ is the template function which describes the intensity function for every template *i* [88]. The summation is extended over the *m* nonzero reciprocal space points contained in the template. These two functions and their related parameters will be discussed below in more detail.

In this template matching technique, the template with the highest Q_i is selected for a given solution. However, due to the fact that ambiguities are quite frequent, some unreliable measurements of a particular orientation cannot be avoided. Therefore, the degree of confidence should be characterized for each identification, for which a so-called reliability index R is defined as follows:

$$R=100\left(1-\frac{Q_2}{Q_1}\right) \quad (2)$$

where Q_1 and Q_2 represent the two highest values of Q_i for distinct solutions of the template.

If Q_1 is much higher than Q_2, then R will be large (ultimately till 100), which means only this Q_1 solution fits best and the result is deemed reliable. When Q_1 and Q_2 are quite close in value, R could be very small (close to 1), which indicates that several solutions are all possible for the indexing or at least hard to discriminate and the orientation and phase determination obtained by Q_1 is not very reliable. Since Q_i and R are calculated for each pixel in the real space image, the so-called reliability maps, with R values ranging from 1 till 100, can be produced. Conventionally, brighter colours mean higher R values [88].

The above defined matching and reliability parameters are a measure on the precision of the match with fixed settings for a single DP (i.e., for each pixel) but does not provide an absolute indication on the final accuracy of the data which can further be optimized by changing the settings, both in the experiment and calculation. In order to discriminate results quantitatively between different settings, the χ^2 method which is widely used to quantify the similarity between two comparable objects is selected as the measurement of image representability. Because the goal of this research is to investigate the Ni_4Ti_3 precipitates in the Ni-Ti alloy, the recognition of precipitates in the image is the main concern. Length, width and perimeter are three parameters chosen to describe the shape of each precipitate and to compare different precipitates. For each precipitate, it is also possible to measure these three values manually so a reduced χ^2 function can be defined as follows:

$$\chi^2 = \frac{1}{n}\sum_{i=1}^{n}\left[0.316\frac{(l_i-l_{i0})^2}{l_{i0}^2} + 0.052\frac{(w_i-w_{i0})^2}{w_{i0}^2} + 0.632\frac{(p_i-p_{i0})^2}{p_{i0}^2}\right] = \frac{1}{n}\sum_{i=1}^{n}\chi_i^2 \quad (3)$$

where *n* stands for the number of precipitates measured in one image and χ_i^2 corresponds with one single precipitate. *l*, *w* and *p* represent length, width and perimeter, respectively. The length and the width of the Ni_4Ti_3 precipitate in the 2D images in this study essentially correspond to the maximum and minimum Feret diameters of the precipitate, which are determined as the largest or smallest distances between the two parallel lines that touch the edge of the precipitate and restricting the precipitate respectively, as shown in Figure 3.2.

Since the length and perimeter of the precipitate are measured with higher relative precision than the width, respective weights of 0.316, 0.052 and 0.632, are added based on each length ratio to the sum of *l*, *w* and *p* values. The subscript *0* stands for the manually measured values using conventional (BF) TEM images and *i* denotes the parameter measured from the ACOM-TEM results. Therefore, l_i, w_i and p_i are the values of length, width and perimeter of the i^{th} Ni_4Ti_3 precipitate obtained from the ACOM-TEM images and l_{i0}, w_{i0} and p_{i0} are the corresponding parameters for the same precipitate as obtained from the conventional (BF) TEM images. As the subscript *i* varies from 1 to n, a series of χ_i^2 values can be obtained and the average value of the sum of these χ_i^2 is recorded as χ^2: as commonly applied, a smaller χ^2 value thus means a higher similarity between these two sets of measurements. This helps to optimize the parameters to achieve the best orientation and phase maps similar to original TEM results.

Throughout this chapter, 8 different precipitates (see below) were selected in a phase map to analyse the influence of the technical parameters. Therefore, n in equation (3) equals 8 and χ^2 is the average over 8 different values. The 8 selected precipitates were chosen for their clear appearance in the conventional BF images so that the manual measurement of their length, width and perimeter will have only small uncertainties. The measurement is performed in ImageJ© by drawing the outline of each precipitate using polygon tools, from which the length, width and perimeter values can be obtained automatically.

In order to study the overall characteristics of the sample, the selected 8 precipitates should represent a diversity of size and orientation. Therefore, the statistical dispersion of the 8 χ_i^2 values is an important parameter and a standard deviation σ of χ_i^2 is introduced to describe the dispersion of these 8 values as shown in equation (4).

$$\sigma = \sqrt{\frac{1}{8}\sum_{i=1}^{8}(\chi_i^2 - \chi^2)^2} \quad (4)$$

So the larger the σ is, the less stable the matching between the BF image and the

ACOM-TEM result will be when applying the optimized parameters for precipitates with other sizes and shapes.

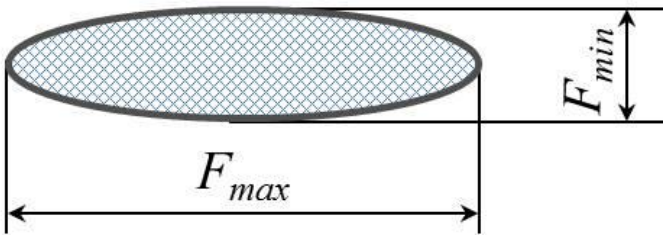

Figure 3.2 Illustration of maximum and minimum Feret diameters of a Ni_4Ti_3 precipitate, F_{max} and F_{min}, respectively.

3.2.2 Diffraction pattern acquisition (Intensity function P(x,y))

The parameters controlling the acquisition of DPs are strongly related to the microscope operation. They include the semi-angle cone of precession (when PED is applied), the acquisition speed and related exposure time, the convergence angle of the electron beam, the probe size and so on. Any changes of these parameters can affect the quality of the acquired DPs with respect to the intended automated mapping.

Precession electron diffraction was first proposed by Vincent and Midgley in 1994 [78]. When DPs are collected using precession, the incoming electron beam is precessing on a cone surface and as such diffraction intensities are summed over a large number of slightly deviating beam orientations which increases the number of reflections that can be used for the template matching and removes strong dynamical effects from the DPs, even for thicker samples up to 100 nm [79]. An example hereof is seen in Figure 3.3. The semi-angle of the cone is referred to as the "precession angle" and is the main parameter which affects the quality of the DPs and the subsequent determination of the orientation and phase maps [89]. The reduction of dynamical effects is important since the ACOM-TEM software does not take dynamical effects into account. The increase of the number of recorded reflections is useful since it can reduce ambiguity in the recognition, especially for low-index zones [90, 91].

Thus, concerning the indexing efficiency, the first attempt to reduce this ambiguity should start from DP collection so as to produce better DPs with less ambiguity problems. This is achieved with the change of reflection intensity in the collected DPs when precession is applied. Figure 3.3 shows two DPs of a precipitate collected using ACOM-TEM without precession (Figure 3.3a) and with precession angle of 0.8° (Figure 3.3b). The DPs were collected along an off-zone axis, which is very common when scanning large regions using the ASTAR application. Numbers on the left side of the spots indicate their intensity, while some weak dots are still visible but not labelled. It can be seen that the number of visible spots increases in the DP acquired with precession and the reflections from high angle crystallographic planes become clearer. Moreover, the intensity of all reflections also changes when precession is used. The average intensity of 8 labelled spots in Figure 3.3a is 133.1 while in Figure 3.3b the average intensity of 14 labelled spots is 100.7. Thus, the intensity of the labelled spots is relatively higher when no precession is used, indicating that precession can bring down the average intensity of a diffraction pattern which allows for a better recognition [92].

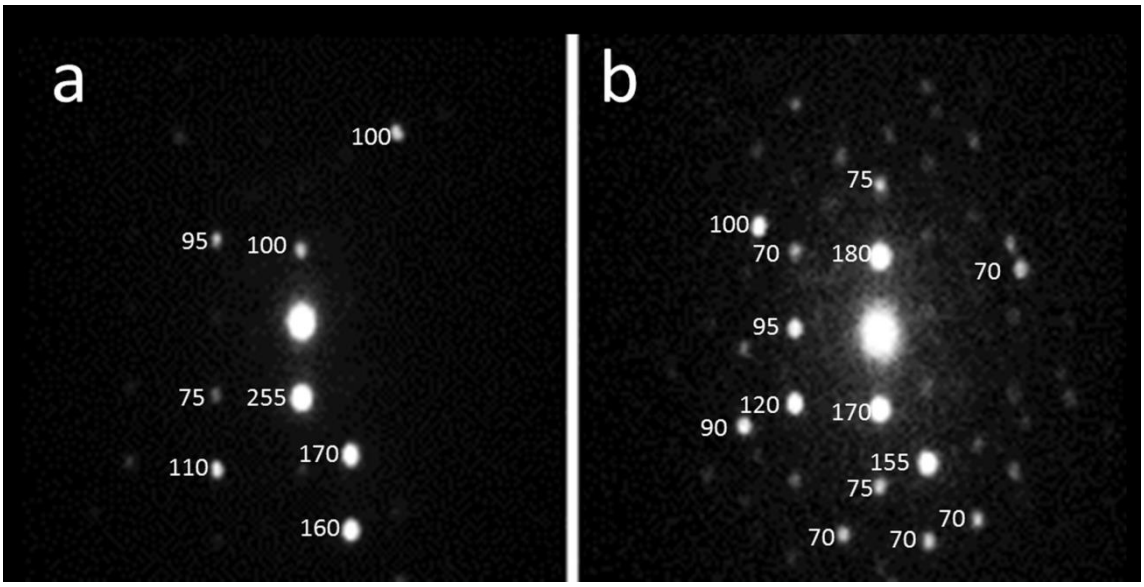

Figure 3.3 The acquired diffraction patterns using ASTAR. (a) without precession and (b) with precession angle of 0.8°.

Table 3.1 shows results of the influence of precession on the phase mapping. Figure 3.4 presents phase mapping results taken with different precession angles (0°, 0.2°, 0.4° and 0.8°) and a BF image is also shown as the reference image in Figure 3.4e (the latter also numerates the precipitates selected for the calculation of χ^2 in equation (3)). The large black spots in Figure 3.4e are contaminated regions which are used as reference regions in phase maps. According to Table 3.1, the best match between the calculated phase map and the original TEM image is reached without using precession or with a small precession angle of 0.2° (smallest χ^2 values) but the σ, indicating the goodness of fit for various sizes of precipitates, is best in the case of the 0.2° precession angle. For higher angles both values strongly increase with increasing precession angle. This may at first be a surprise, since, as shown above, the superspots are better seen in higher precession modes and one would thus expect a better match with the Ni_4Ti_3 structure.

Table 3.1 Average χ2 value and standard deviation (σ) for different precession angles. Other acquisition parameters are constant: C2 = 30μm; spot size #9; scanning speed = 50 fps

Precession angle (degree)	0	0.2	0.4	0.8
χ^2	0.43%	0.48%	0.83%	0.97%
σ	0.33%	0.25%	0.76%	0.79%

The main reason for the loss in recognition of the present nanoscale precipitates in the precession mode is the lower spatial resolution compared with using the ACOM-TEM without precession. Indeed, when a still electron beam illuminates a pixel in the matrix but very close to the precipitate-matrix interface, no Ni_4Ti_3 superspots will be visible, but when this position is illuminated by a precessing beam also intensity from the neighbouring precipitate will be added to the DP and the superspots will be recognized by the software as precipitate structure, although the center of the beam was still outside of the precipitate. Figure 3.5 illustrated the decrease of resolution caused by precession. When tilting the beam during the precession, for some tilt angles part of the beam will pass through the precipitate

and cause superspots to appear for that particular orientation (e.g., case c). Since the final diffraction pattern obtained by precession is the sum of all patterns obtained along the different tilt angles (a + b + c + …) the overall pattern will also contain those superspots, even though the center of the beam is located next to the precipitate. As a result, when applying the phase mapping procedures, the precipitate will appear larger than its real size. This effect becomes more prominent when increasing the precession angle.

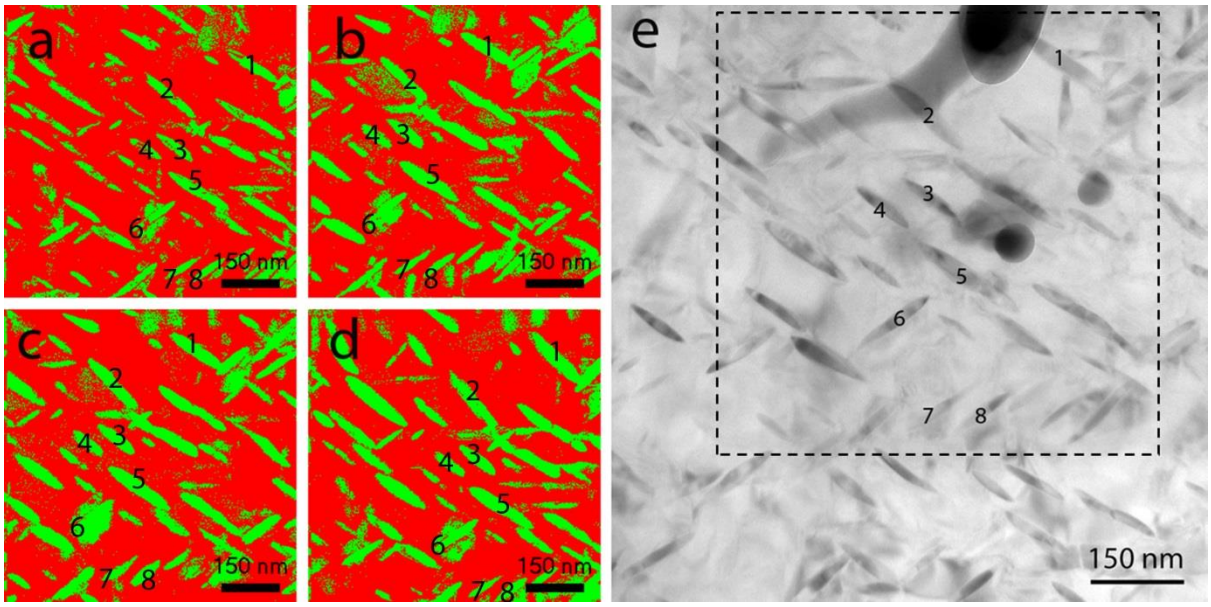

Figure 3.4 The phase mapping of Ni_4Ti_3 precipitates with different precession angles: (a) 0, (b) 0.2, (c) 0.4 and (d) 0.8° taken from the region shown in the TEM BF image of (e) and including the 8 selected precipitates to calculate χ^2, as indicated.

Therefore, the average size of recognized Ni_4Ti_3 will be larger than that in reality and this difference can be observed from Figure 3.4a to 3.4d. Similar to the χ^2, the σ value also increases with precession angle, which indicates that a higher precession angle leads to a higher uncertainty for the indexing of precipitates. Consequently, using the precession angle of 0.2˚ one can already improve the quality of DPs while keeping sufficient spatial resolution. The optimized precession angle of 0.2˚ depends on the actual sample. This means that in this study this angle fulfils the needs of observing the Ni_4Ti_3 precipitates within the Ni-Ti B2 matrix but may not be suitable for other materials. This could be because the aim of using the

precession can be different. For common studies performed with ACOM-TEM, the interest is often on the orientation information such as grain orientation or twins, therefore, the precession is used to enhance the orientation information from diffraction patterns which requires bigger precession angles, while the loss in resolution will not affect the quantification of such information. However, in the present study, the influence of the precession on the resolution can not be ignored while the orientation information is less critical due to the known crystallographic relationship between the matrix and precipitates. In principle one could maybe even further improve the χ^2 and σ values in Table 3.1, but judging from the small difference in σ between no precession and 0.2° the gain when compared with respect to the 0.2° angle would not outweigh the large amount of extra work, certainly if one wants to find the absolute minimum for σ.

The spot size and convergence angle of the electron beam are two other major variables affecting the spatial resolution or pixel size of the ASTAR results. The condenser lenses (C1 and C2) affect the spot size and the C2 condenser aperture size affects the convergence angle of the beam. The resulting spot size of the electron beam defines the minimum value for the spatial resolution of the technique. In principle, a smaller spot size for the scan leads to a higher spatial resolution, but since the intensity of the beam is also reduced, so will the diffraction spots hamper the automatic recognition of the pattern. Therefore, different spot sizes and C2 condenser apertures were used to reach the optimized spatial resolution, defined as the FWHM of the spot recorded on the CCD, and shown in Table 3.2 (an image of the set of apertures is shown in Fig. 3.6). It is seen that a 10 μm C2 aperture provides a relatively lower spatial resolution despite the variation of spot size and precession, which is due to the parallel incident beam caused by a small C2 aperture. Thus, 30 μm and 20 μm apertures are preferred for data collection in view of higher spatial resolution. The combination of C2 aperture, precession angle and spot size gives a variety of spatial resolution which can be further optimized as function of the actual microstructure of the sample.

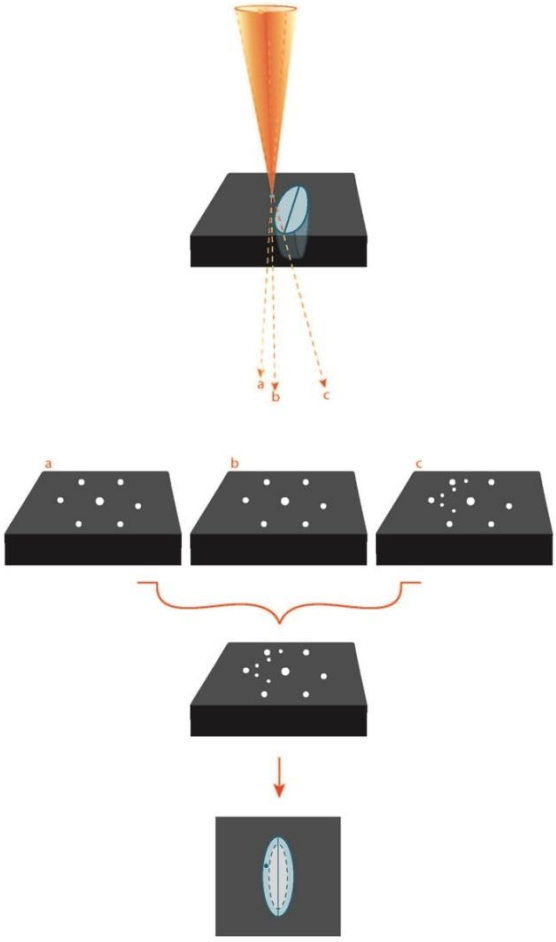

Figure 3.5 An illustration of the effect of precession on spatial resolution.

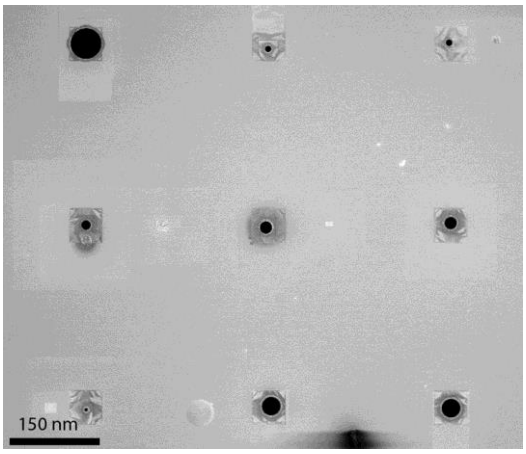

Figure 3.6 Si_3N_4 foil with 9 C2 apertures produced by FIB and ranging from 5 till 50 micron in diameter.

Table 3.2 Spatial resolution (nm) of ASTAR with different spot sizes and C2 apertures with and without precession.

Precession angle	Spot size # / C2 aperture	7	8	9	10
0°	30 μm	3.7	2.8	1.8	1.4
	20 μm	2.7	2.1	2.0	1.9
	10 μm	3.7	3.6	3.5	3.0
0.2°	30 μm	3.9	3.1	2.7	2.7
	20 μm	3.0	2.7	2.5	2.4
	10 μm	3.7	3.6	3.6	3.6

Based on the results of Table 3.2, different ASTAR data are acquired using the optimized parameters to study both χ^2 and σ values in the final maps. The parameters are used in which the spatial resolution is close to 2.5 nm and step size of 2.5 nm was used to cover the entire selected region. The precession of 0.2° was also used to acquire these maps. The comparison of both χ^2 and σ values are presented in Table 3.3. The results show that the combination of a 30 μm C2 aperture with spot size #9 gives the smallest value for both χ^2 and σ. It should further be noticed that the thickness of the sample plays an important role and affects the intensity of DPs. Therefore, the optimized setting obtained in Table 3.3 can be changed for thicker samples, i.e. when the sample is thicker, 30-8 would be better because a brighter incident beam could be provided, and when a sample is thinner, 20-9 will be more suitable with weaker beam intensity. According to Table 3.3, all these three combinations have smaller χ^2 and σ value, which means there will be no major variation of accuracy in the final indexing. The reason that the sample thickness affects the quality of the DPs is mainly due to the dynamical scattering and the energy absorption of inelastic scattering of the incident beam. In this study, the effect of dynamical scattering is reduced by precession, which means absorption is the major influence. Therefore, as the sample thickness increases, the intensity of the DPs will decrease, which requires a larger C2 aperture as well as a bigger spot size in

order to increase the intensity of the incident beam and to maintain the intensity of the DPs.

Figure 3.7 and Table 3.4 show the influence of scanning speed on the final ASTAR maps. The optimized parameters (Table 3.3) were used to acquire these maps. Three scanning speeds were chosen as 25 fps, 34 fps and 50 fps, which correspond to exposure times of 40 ms, 30 ms and 20 ms, respectively. Figure 3.7 shows the effect of scanning speed on the quality of the DPs with line profiles taken along the red arrows in the acquired DPs. With the decrease of the scanning speed, the signal to noise ratio of the acquired spots and the number of visible spots increases, which will both lead to better indexing. It is obvious that the quality of DPs improves with the decrease of scanning speed and Table 3.4 quantitatively shows the influence of scanning speed on the ASTAR maps. As expected, slower scanning speed increases both accuracy (χ^2) and data stability (σ): data stability is already strongly improved when changing speed from 50 fps to 34 fps, while shape accuracy increases fast when changing speed from 34 fps to 25 fps. For the study of a Ni-Ti alloy with precipitates, a relatively large region is required for analysis, which means improving the data quality by scanning at smaller regions is not a good option because the useful sample information will be decreased when the scanning region is decreased which will eventually decrease the accuracy for quantitative analysis. For a typical 1 μm × 1 μm image it takes about 106 mins to acquire the data with a scanning speed of 25 fps and a step count of 2.5 nm. This acquisition time almost reached the achievable time limit in this experiment, because the experiment was carried out on an in-situ heating holder heated to 50 °C during the data acquisition process in order to eliminate the influence of the R phase. During in-situ heating, sample drift can not completely be avoided which limits the total time for data acquisition. Thus, a scanning speed slower than 25 fps will induce a dramatic time for acquisition and sample drifting could become a serious problem while the improvement of indexing accuracy is very limited because 25 fps already gives strongly improved χ^2 and σ values.

Table 3.3 Average χ^2 value and standard deviation (σ) for different combinations of C2 aperture and spot size.

C2 aperture-spot size	30-8	30-9	30-10	20-7	20-8	20-9
χ^2	0.43%	0.42%	0.61%	2.57%	0.57%	0.57%
σ	0.29%	0.26%	0.80%	3.07%	0.43%	0.30%

Table 3.4 Average χ^2 value and standard deviation (σ) of the ACOM-TEM maps acquired in different scanning speeds, other parameters kept constant: C2 = 30 μm; spot size #9; precession angle 0.2°.

Scanning speed	50 fps	34 fps	25 fps
χ^2	0.80%	0.74%	0.41%
σ	0.90%	0.37%	0.25%

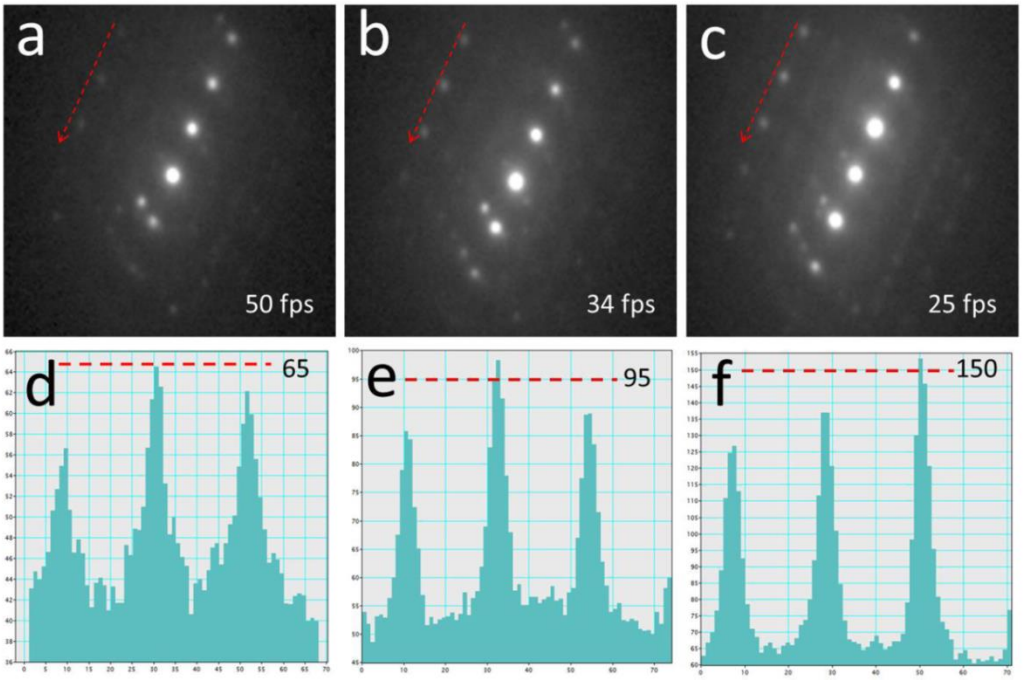

Figure 3.7 Acquired DPs using ASTAR with different scanning speeds (a) and (d) 50 fps; (b) and (e) 34 fps; (c) and (f) 25 fps; (d) (e) and (f) line profile of the corresponding arrow shown in (a) (b) and (c), respectively.

3.2.3. Template generation and calculation (Template function Ti(x,y))

Template generation and calculation parameters are directly associated with the ASTAR software and include template generating parameters such as excitation error, intensity scale etc. and diffraction pattern indexing parameters such as distortion correction constant, camera length and noise threshold. Most of these parameters can be modified off-line and they play an important role in the final ACOM-TEM maps.

For most cases, default settings for template generation work well, as seen from the example shown in Figure 3.8 in which $NiTi_2$ precipitates are distributed at grain boundaries in an aged Ni-Ti B2 sample. Both structures are well recognized and distinguished by the software, even when using the default settings. Although $NiTi_2$ has a very large lattice parameter (a=1.132nm, cubic) with 136 atoms in the unit cell yielding fairly dense DPs, this complexity in the DPs does not cause any difficulty in the indexing step. This is because the DPs generated by Ni-Ti B2 and $NiTi_2$ are quite different and without overlapping spots. Thus, despite the fact that the acquired DPs will never represent the complete generated patterns, the indexing results can be good. In contrast, Ni-Ti alloys containing Ni_4Ti_3 precipitates in a Ni-Ti B2 matrix have common spots which make it difficult to generate sharp maps. One way to improve the quality of the maps is to optimize the parameters of the template generation.

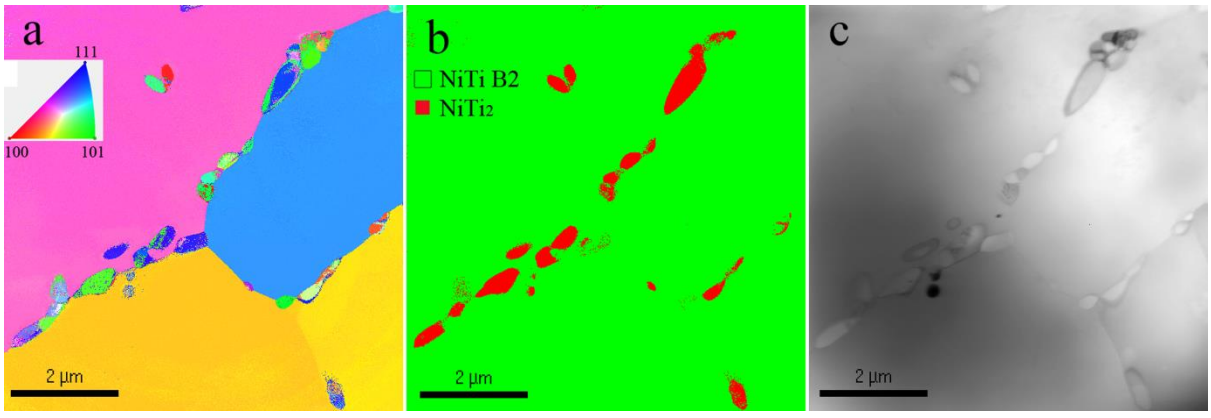

Figure 3.8 ACOM-TEM and conventional TEM images of Ni-Ti sample with $NiTi_2$ precipitates at grain boundaries: (a) orientation mapping, (b) phase mapping, (c) conventional TEM BF image.

When the Bragg condition is not fully satisfied for a given reflection, the spot appears weak in the DP. The allowed excitation error is one of the important parameters in the template generation process and is defined as the allowed deviation from the perfect Bragg condition for a certain reflection to be included in the template. The excitation error value is represented as the distance from the reciprocal lattice point **G** to a point on the Ewald sphere measured along the vertical direction to the upper surface of the specimen. In the template generation software, this value is set from 0 to 1. Excitation error 1 allows for a maximum number of reciprocal space points (around 20000 in the case of Ni_4Ti_3 at 200kV), and when it is approaching 0 only the (000) spot will be visible since all other spots will slightly deviate from the Ewald sphere and will not be included due to a small excitation error. Table 3.5 shows the effect of excitation error on the quality of ACOM-TEM phase maps in the Ni-Ti alloy (and using the optimized parameter values from the above DP acquisition part). When decreasing the allowed excitation error value, the spots in higher-order Laue zones (HOLZ) are eliminated, consequently decreasing the quantity of spots involved in the generated templates for the indexing. For the experimentally acquired DPs, the number of visible spots is normally lower when compared with the templates. This difference in number of HOLZ points between real and simulated DPs will influence the indexing results which will thus strongly depend on the excitation error. Figure 3.9 shows four phase mapping results with different excitation error values obtained from the region indicated by the dashed line in Figure 3.9e. It is clear that when the excitation error equals 1, which is also the default value, the recognition of precipitates becomes very difficult. Increasing the excitation error greatly improves the quantity of higher order spots in the templates and these spots are hardly visible in the acquired DPs. Also, the difference between these calculated DPs are actually quite narrow, so that when matching them with the experimental DPs, very similar Q_i values are obtained, which in the end lowers the reliability and adds noisy spots in the maps. When the excitation error becomes too small, the templates generated contain insufficient reflections to properly complete the indexing. In Table 3.5, a smaller σ value means that more precipitates

can be recognized with clear outlines, leading to smaller variation between each measurement when measuring different precipitates, while a large χ^2 means that the size of these precipitates have some variation compared to the values obtained from conventional BF images. According to Table 3.5, an excitation error of 0.2 fits best with the original shape of the precipitates based on the average χ^2 value and standard deviation σ as defined above.

Table 3.5 Average χ^2 value and standard deviation (σ) with different excitation errors, acquisition parameters kept constant: C2 = 30 μm; spot size #9; precession angle 0.2˚, scanning speed 50 fps.

Excitation error	0.1	0.15	0.2	0.25	0.3	0.5	1
χ^2	2.33%	1.42%	0.42%	1.21%	1.61%	1.42%	40.42%
σ	2.57%	1.50%	0.26%	1.36%	1.59%	1.28%	14.01%

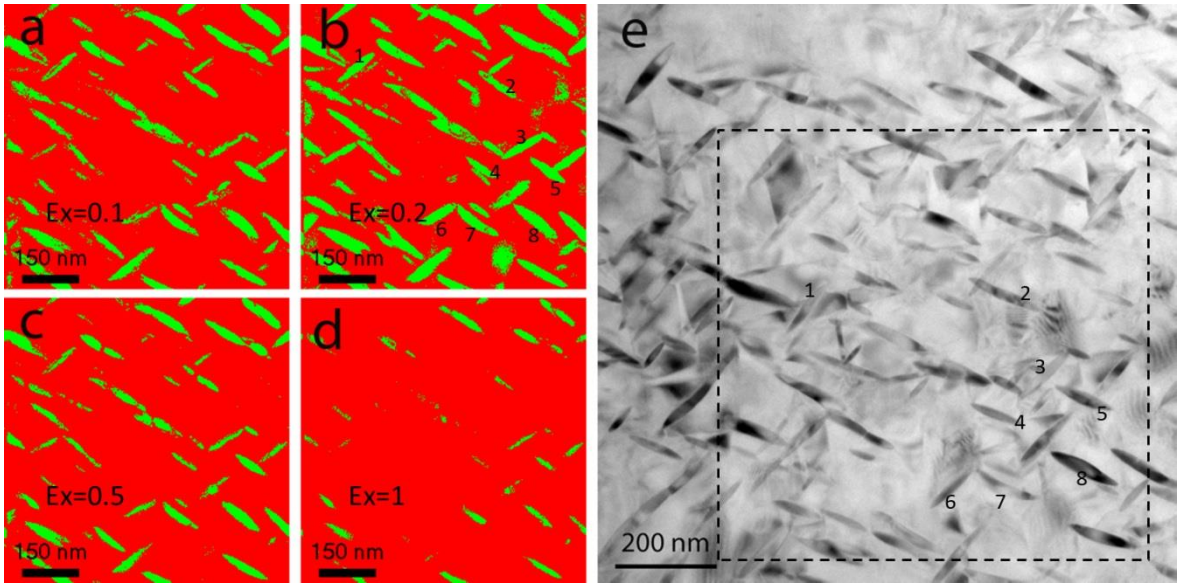

Figure 3.9 The phase mapping of Ni4Ti3 precipitates in Ni-Ti alloy with different excitation errors: (a) 0.1, (b) 0.2, (c) 0.5 and (d) 1 taken from the same region shown in the TEM BF image of (e) and including the 8 selected precipitates to calculate χ^2, as indicated.

The intensity scale (IS), which is defined as the intensity ratio between different spots in

calculated DPs and is defined between 1 (default) and 100 (all reflections have equal intensity), is another parameter that affects the accuracy of ACOM-TEM final maps. The intensity difference between different spots in a DP is a combination between scattering conditions such as orientation and thickness of the crystal and scattering factors of different elements involved. However, since the thickness of the sample is often not known and dynamical scattering cannot completely be ruled out and absorption is not taken into account, the default IS setting is often insufficient for a good match. Increasing the IS (start from default value 1) has the effect of enhancing the weakest reflections compared to the strongest one. Table 3.6 shows the effect of the IS value on the quality of obtained phase mapping based on the calculated average χ^2 value and standard deviation (σ) (using the above obtained optimized values for the acquisition parameters). Additionally, Figure 3.10 shows four phase mapping results with different IS values obtained from the region indicated by dashed line in Figure 3.10e. An IS of 14 provides the optimized results and similar shape of precipitates compared with the original TEM image, as seen in Figure 3.9b. The default IS value of 1 reveals the worst result for the phase mapping, with the boundaries of several precipitates being blurred when compared with Figure 3.10b, 3.10c and 3.10d. This indicates that the intensity ratio in the acquired DPs is smaller than the default IS value. Therefore, increasing IS will gradually decrease the intensity ratio between weakest and strongest reflections in the simulated DPs and at a certain value, it will fit with the collected DPs. In Table 3.6, when IS is higher than 14, the change in the average value of χ^2 is less obvious than the case when IS is smaller than 14. A smaller IS value means a higher ratio between high intensity and low intensity spots, which will enable templates to match weaker intensity spots with higher sensitivity, therefore causing blurred boundaries and large areas of noisy spots, as is indeed the case in Figure 3.10a. Apart from IS = 14, IS = 12 and IS = 16 also show smaller σ values, but their χ^2 are relatively large, which indicates that the intensity ratio in these two conditions are already getting close to the actual value of the collected DPs, but still not the best condition. The smaller σ value indicates that most of the precipitates can be recognized

already with clear outlines, while large χ^2 indicate that the size of these precipitates still has some variation compared to the values obtained from conventional BF images. Thus, the application of an IS value of 14 for Ni_4Ti_3 precipitates provides the best result for the phase mapping.

The template generation angular step (step counts) is the third parameter to discuss. In the template generation software, all the templates are generated with an angular step of the order of 1˚. Increasing the step count provides more generated templates so that the degree of overlap between two successive templates increases and thus can improve the indexing result. However, this improvement also depends on the lattice structure and symmetry of the calculated unit. For example, for a cubic lattice, due to the high symmetry, the templates covering two standard triangles (one basic and one a cross-check) on the stereographic projection map are sufficient to be used for indexing, which requires approximately 3000 templates to be generated [93] with a relevant step count of 80. Thus, due to the lower symmetry of Ni_4Ti_3 precipitates (rhombohedral crystal structure), larger angles need to be covered with templates at an angular step of 1˚, and a higher step count is required.

Table 3.6 Average χ^2 value and standard deviation (σ) with different intensity scales (other template generation and acquisition parameters kept constant: excitation error = 0.2; C2 = 30 μm; spot size #9; precession angle 0.2˚, scanning speed 50 fps).

Intensity scale	1	8	12	14	16	20	50	100
χ^2	2.09%	1.39%	1.33%	0.42%	1.02%	1.00%	1.18%	1.19%
σ	1.95%	1.86%	0.80%	0.26%	0.62%	1.18%	1.43%	1.76%

Table 3.7 Average χ^2 value and standard deviation (σ) with different step counts (other template generation and acquisition parameters are kept constant: excitation error = 0.2; IS = 14; C2 = 30 μm; spot

size #9; precession angle 0.2°, scanning speed 50 fps).

Step count	50	100	120	200
χ^2	2.70%	1.92%	0.42%	1.88%
σ	1.99%	2.19%	0.26%	1.87%

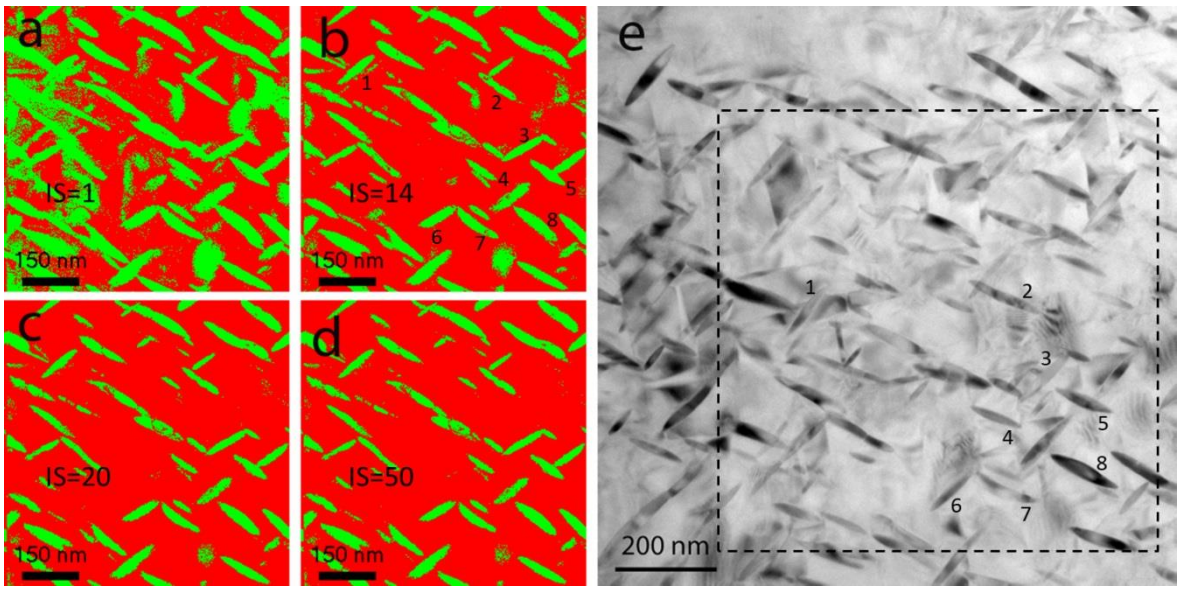

Figure 3.10 The phase mapping of Ni4Ti3 precipitates in Ni-Ti alloy with different intensity scales: (a) 1, (b) 14, (c) 20 and (d) 50 taken from the same region shown in the TEM BF image of (e) and including the 8 selected precipitates to calculate χ2, as indicated.

Table 3.7 shows the influence of different step counts. The generated templates with step counts of 50 and 100 are insufficient, as seen from the higher χ^2 value. For a step count of 120, the result is much better but when the step count increases to 200, the χ^2 value becomes higher again while it also causes a longer calculation time. The latter is a consequence of a large amount of templates which are involved in the calculation. As a result, the degree of overlap between two successive templates becomes too high, which will cause the appearance of similar Q_i values complicating the interpretation of the reliability values.

3.3 Optimization results

The above obtained optimized parameters of experimental and calculated DP of Ni_4Ti_3 were applied to a feedback test. For the template generation these are excitation error 0.2, intensity scale 14 and step count 120, for the data collection these are precession angle 0.2°, spot size #9, 30 μm C2 aperture and 50 fps scanning speed. For the B2 matrix phase, the template generation was performed using the default and optimized values. Still, for a complete indexing process in which the data acquisition and template generation results are combined, several other parameters are also involved. However, it was found that those parameters have limited influence on the final results when compared with the parameters discussed above. Thus, all parameters which were not discussed above are kept as default values throughout this article. These parameters include: smoothing radius 5, centre shift 10, softening loop 1, spot radius 5, noise threshold 10, gamma 0.5 and fast matching using 10 test counts.

The result of the feedback test using the above optimized values for the Ni_4Ti_3 precipitates and default values for the B2 matrix is shown in Table 3.8. χ^2 and σ values are small which means the shape of the precipitates is properly displayed. The phase map result for this case and the corresponding reliability map are shown in Figure 3.11a and 3.11b, respectively. Despite the shapes of the precipitates being properly represented, the overall phase map is not perfect. Large areas of miss-indexed noisy spots appear on the matrix region of the map. In the reliability map, precipitates have higher reliability (brighter regions) compared with other regions of matrix. Concerning the fact that optimization of template generation was only finished for precipitates, this reliability image gives an impression that the indexing of the matrix may play an important role. Thus, a new optimization was also made on template generation for the Ni-Ti B2 phase and the result can be seen in Table 3.8. The parameter of default setting for Ni-Ti B2 is: excitation error 1, intensity scale 1 and step count 50. Despite that B2 structure has smaller lattice parameter for matrix indexing, excitation error 1 is still too large to be applied. Hence excitation error will be reduced in the optimized template. As for step count, it was discussed in the optimization of step counts of precipitates already that

for cubic structure, the step count should reach 80 to ensure a complete indexing. Optimized template for B2 changed excitation error from 1 to 0.5 and step count from 50 to 80, while the intensity scale keeps unchanged because the matrix is less sensitive to the intensity changes in DPs. The mapping result of optimized B2 template is shown in Table 3.8 and Figure 3.11. Comparing Figure 3.10a and 3.10c, phase mapping with optimized B2 template displays cleaner matrix with much less miss-indexing regions. The mean intensity values of two reliability maps, Figure 3.11b and 3.11d, which represent default and optimized reliability maps, respectively, are measured 87.4 and 108.4, respectively. According to the definition of reliability in the software, higher intensity value indicates a higher reliability for the indexing results. Thus, it is clear that new template for the B2 matrix improves the reliability of indexing. In Table 3.8, the change in B2 template has very limited effect on the indexing result of Ni_4Ti_3 precipitates. The χ^2 slightly increases meanwhile σ decreases, but both of them are in very small variation range. Hence it can be concluded that the optimized B2 template improves the indexing accuracy in the matrix without a large influence on the precipitates.

Using the above optimized parameters, the 2D images of orientation and phase mapping results obtained from Ni-Ti alloys can be used to quantitatively study the size and distribution of Ni_4Ti_3 precipitates under different aging conditions and which will be discussed in detail in next chapter.

Table 3.8 Feedback result applying optimized parameters. For P(x,y), spot size #9, C2 = 30μm, precession angle 0.2˚, scanning speed 50 fps.

	Ni-Ti B2 Template Default	Ni-Ti B2 Template Optimized
χ^2	0.60%	0.67%
σ	0.70%	0.68%

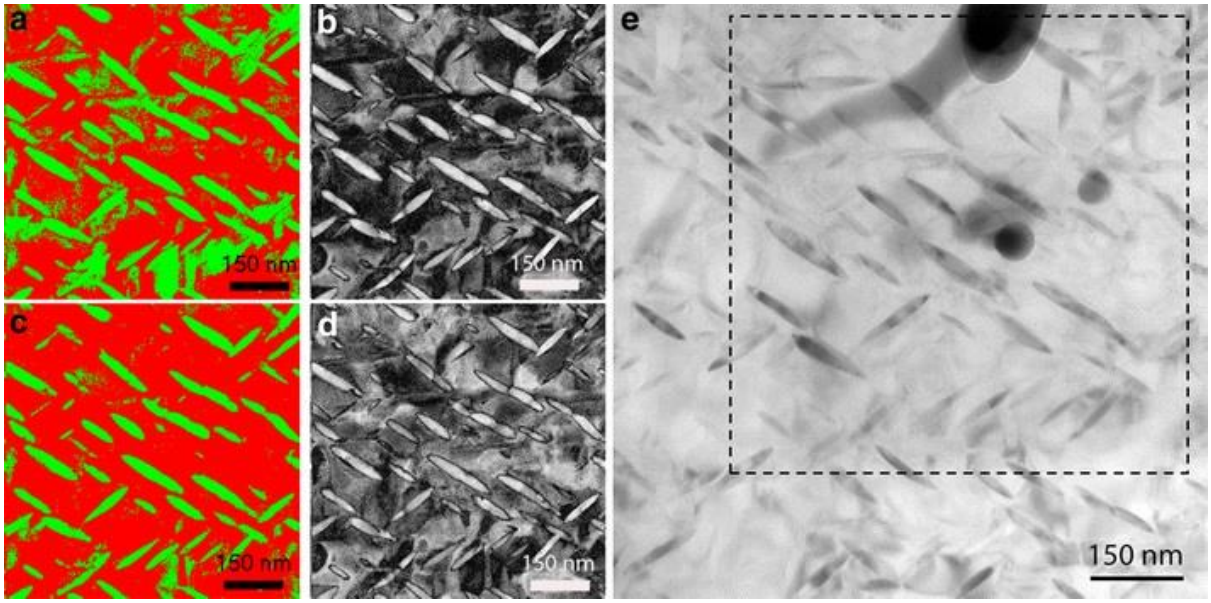

Figure 3.11 The phase mapping of Ni_4Ti_3 precipitates in Ni-Ti alloy with different Ni-Ti B2 template generations: (a) default template, (c) optimized template, and reliability maps (b) default template and (d) optimized template, all taken from the same region shown by dashes in the TEM BF image of (e).

The final optimized result is a combination of all optimized parameters, therefore it is not easy to conclude which parameter plays the main role. In the beginning of the optimization process when only one parameter is concerned, the results show a tendency that a particular value yields the best results possible, but these results are still not good enough overall. It is possible to discuss this issue by comparing the χ^2 and σ values to give a rough estimation. In the data collection part, the influence of precession is bigger than other data collection parameters, due to the strong improvement to the quality of DPs. In the template generation

part, all parameters have a similar effect, changing either of them will lead to a decrease of image quality. In this study, the basic idea of the optimization is to adjust the quality of the DP and template to distinguish the weak superspots of Ni_4Ti_3 precipitates from the matrix, which is different from the common goals of data acquisition of ACOM-TEM, which is often more focused on the orientation information. Therefore, such an optimization process in this study can be also applied to similar conditions that aim for the distinction of different spots in DPs. Among all these parameters, template generation parameters are really specific for the Ni_4Ti_3 precipitates while data acquisition parameters can more readily be applied to similar cases with other materials.

4. Conclusions

Automated Crystal Orientation and Phase Mapping in the TEM were used to obtain quantified orientation and phase maps of nanoscale Ni_4Ti_3 precipitates in a Ni-Ti all-round shape memory alloy. In order to properly and quantitatively determine the distribution of the precipitates using ACOM-TEM, different acquisition, template generation and indexing parameters were used and optimized to achieve reliable maps. The results show that the precession (even for small angles) is an important additional technique because it increases the reliability of indexing the acquired DPs from precipitates. In a Tecnai G2 instrument the combination of 30 μm or 20 μm C2 aperture with spot size #8 or #9 provides high quality DPs, however, with the optimal combination affected by sample thickness. A relatively slow scanning speed of around 25 fps improves the DP quality. For template generation, default settings need to be changed for both the Ni-Ti B2 matrix and Ni_4Ti_3 precipitates. The templates of the Ni_4Ti_3 precipitates should be generated with an excitation error of 0.2, an intensity scale around 14 and a step count of 120. For the templates of the Ni-Ti matrix, the optimized excitation error equals 0.5, the intensity scale 1 and step count 80.

Chapter 4

Quantitative investigation of Ni_4Ti_3 precipitates in all-round Ni-Ti shape memory alloys by ACOM-TEM technology

4.1 Introduction and material preparation

4.1.1 Introduction

As mentioned in the first chapter, Ni_4Ti_3 precipitates can strongly affect the phase transformation temperatures and shape memory behavior in Ni-rich Ni-Ti alloys. When Ni_4Ti_3 precipitates are induced by aging, they will not only affect the transformation behavior by inducing internal strain fields but also by depleting Ni around the precipitates. Both of these effects have been quantitatively investigated using advanced electron microscopy techniques [51, 94]. Ni depletion in the matrix leads to a decrease of the M_s temperature, while internal strain fields promote the formation of the R phase, the transformation strain of which is smaller than that of martensite and better matches the strain fields surrounding the precipitates [41, 51, 95, 96]. However, the influence of Ni depletion depends strongly on the diffusion of Ni, which can be greatly influenced by the distribution and the size of the Ni_4Ti_3 precipitates. The internal strain field of the precipitates is also closely related to their size [94]. The maximum expansive strain, which is located at a distance *d* from the interface of the precipitates and the matrix, will increase with the precipitate size as long as the coherency between precipitates and matrix is retained. For example, for smaller precipitates with a dense distance distribution of approximately 40 nm, a 20 nm unstrained matrix region is

observed. Thus, the variation in the size and distribution of Ni_4Ti_3 also has strong effects on the internal stress fields. Due to the combined interaction of Ni_4Ti_3 precipitates, a quantitative determination of the influence of aging on the microstructure and the transformation behavior will provide a better understanding of the anisotropic precipitation mechanism, which can then be used to improve the functional properties of the material.

This chapter describes the all-round shape memory effect induced by constrained aging in $Ni_{51}Ti_{49}$ alloys, which raises another issue focusing on the influence of the external stress on the nucleation and growth of Ni_4Ti_3 precipitates. While some studies on the influence of the external stress during aging were already discussed in the first chapter, most of the current studies are focused on a certain crystal orientation in single crystal alloys. How Ni_4Ti_3 variants will nucleate and grow in polycrystalline alloys where the crystal orientation and external stress direction are not fixed in each grain remains unexamined.

ACOM-TEM, which was already introduced in detail in chapter 2, is a new technique that can be used to collect both orientation data and morphological data for the Ni_4Ti_3 precipitates after the optimization process described in chapter 3. From the phase maps acquired by ACOM-TEM in this study, it will be very easy to distinguish the Ni-Ti matrix and precipitates, allowing for a quantitative calculation of the properties of the Ni_4Ti_3 precipitates in a rapid and effective manner. The crystal orientation information of the Ni-Ti matrix and Ni_4Ti_3 precipitates obtained from the orientation maps can be used to calculate their relationship with the external stress during constrained aging, and this calculation with external stress can in turn help to identify the orientation relation of each Ni_4Ti_3 variant with the matrix.

This chapter describes the quantitative investigations of the Ni_4Ti_3 precipitates from both orientation distribution and phase distribution data. The phase distribution study improves the understanding of the relationship of the aging parameter with the growth of the Ni_4Ti_3 precipitates and shape memory properties, while the orientation distribution study explains

how Ni_4Ti_3 variants will adjust under external stress during their nucleation and growth process in these multi-grain samples.

4.1.2 Material preparation

The $Ni_{51}Ti_{49}$ alloys used in this study were prepared by the arc melting method using electrolytic nickel (purity >99.9%) and titanium sponge (purity >99.7%). The melting process was repeated six times for every ingot in a non-consumable vacuum arc melting furnace connected to a vacuum casting part with a water-cooled thick copper mold. The dimensions of the Ni-Ti ingots after melting and casting are 70 × 8 × 0.5 (length × width × thickness) mm^3. To homogenize the composition of the alloys, a solid solution treatment at 850°C for 3 h under an Ar (purity 99.9%) protective atmosphere followed by water quenching was applied. After the solid solution treatment, constrained aging was applied to introduce the TWSME of the alloy. Ni-Ti stripes were placed in a specially designed arch mold with a diameter of 48 mm and underwent different aging time and temperature treatments; the structure of the mold for constrained aging is shown in Figure 4.1a. According to conventional engineering mechanics, the stress conditions of the bent stripes vary over the cross-section of the stripe with tensile stress on the outer side of the bending ring and compressive stress on the inner side, as indicated in Figure 4.1b. Meanwhile, a comparison batch was prepared under the same thermal conditions but without stress assistance. The TWSME of these constrained aged alloys was studied by Li et al. which showed that different aging conditions lead to different shape change behaviors [105]. The recovery ratio of the strip, as defined and used by Li et al. to describe the shape change of the alloys between different temperature states, will also be used in this study to link the shape change behavior to the microstructure of the materials. The recovery ratio *r* is defined as follows:

$$r = \frac{\theta_p - \theta_m}{\theta_d} \times 100\%$$

where θ_p and θ_m are the arc angles of the Ni-Ti alloy strip in the parent and martensite

phase, respectively, θ_d is the arc angle of the Ni-Ti alloy strip in the constrained state, as shown in Figure 4.2.

Phase transformation temperatures were studied by DSC (Q200, TA), and the microstructure of the alloy was investigated by TEM (Tecnai G2, Thermo Fisher scientific) and ACOM-TEM was applied for the quantitative analysis of both orientation and phase distribution of the Ni_4Ti_3 precipitates. TEM specimens were prepared both by twin-jet electropolishing and FIB depending on the region in the bulk ingot to be sampled. Electropolished specimens are from the unconstrained samples and FIB specimens are from the constrained samples. Figure 4.1c shows two typical positions where FIB specimens were taken, with the first position A perpendicular to the stress direction of the stripe and the second position B parallel to the stress direction. The FIB specimens were taken from both tension and compression sides of the stripe as indicated in Figure 4.1c.

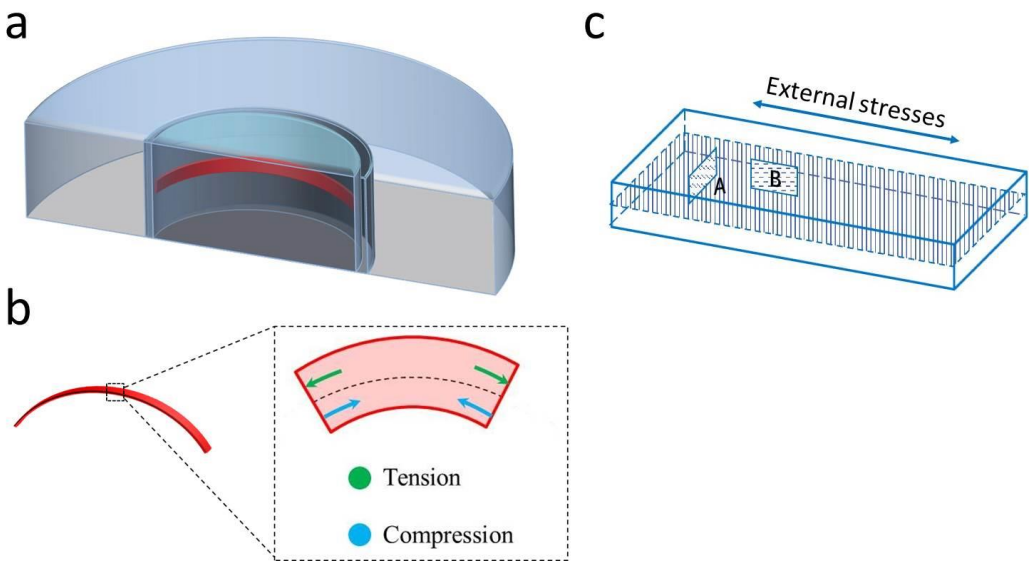

Figure 4.1 (a) A brief illustration of the constrained aging mold with Ni-Ti alloy stripe inside, (b) the distribution of external stress in the stripe, (c) FIB sample positions of constrained aged Ni-Ti stripes.

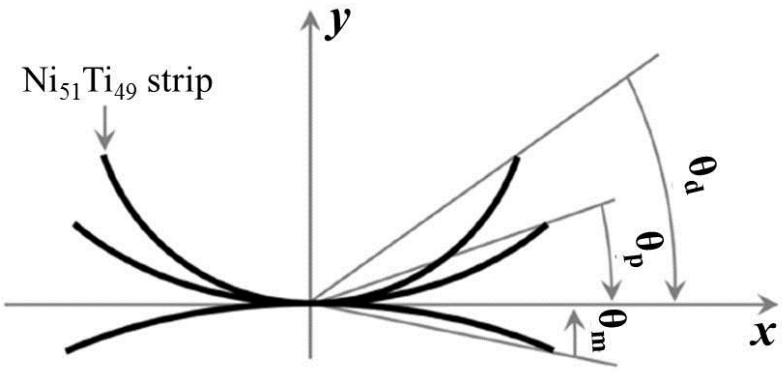

Figure 4.2 An illustration of the parameters used for the calculation of two-way shape memory recovery ratio of the Ni-Ti alloy strip.

4.2 Quantitative study of Ni_4Ti_3 precipitates in a $Ni_{51}Ti_{49}$ all-round shape memory alloy by TEM phase imaging

4.2.1 Statistical methodology

Since the distribution of Ni_4Ti_3 precipitates inside the alloy is three-dimensional (3D) and the results acquired by ACOM-TEM are two-dimensional (2D), it is necessary to establish a correlation between the 2D images and the 3D structures. One possible and effective solution is to apply stereological theory in this analysis. Stereology is an effective approach for extracting quantitative information about a 3D material from the measurements made on 2D planar sections of the material. Stereology deals with the methods of making quantitative estimations on the value of a geometrical feature within the object of interest, the object being the piece of material to be studied. These features used for quantification are usually geometrical elements, e.g., the number, length, surface area and volume depending on the actual spatial dimensions. The properties of these geometrical elements in 3D space can be quantified by placing grids of various dimensions randomly into the space and recording the manner in which they intersect with the structures of interest. The basic equation for the quantitative determination of a geometrical feature is given by $V_V = A_A = L_L = P_P$, where V is the volume, A is the area, L is the line, P is the point and V_v is the volume fraction of the

given phase within a reference volume v. Subscripts have the same meaning for V, A, L and P. Thus, the equation describes the mathematical relationship from the observed feature for the interactions between the grids of various dimensions and a sectional profile of an object. This equation allows the extraction of geometric quantitative information of the 3D features from the lower-dimensional images. Applying this equation to the present study, the relationship $V_V = A_A$ can be used to study the volume fraction of 3D materials by calculating the ratio of the sectional profile area of an object to the area of the entirely investigated section, where the sectional profile area is the phase mapping image collected with ACOM-TEM. However, since the 2D images are obtained in TEM and TEM specimens have a thickness which can not be ignored, the 2D images can be considered as projections of 3D objects. Therefore, a correcting factor is needed to relate V_V with A_A, which can be described as: $V_V = k_t\,(V_V) \bullet A_A$, in which k_t is the correction factor that can be described as:

$$k_t(V_V) = 1/(1 + \frac{t}{4} \bullet \frac{\bar{S}}{\bar{V}})$$

where t is the thickness of the TEM specimen. In this study, all TEM specimens were prepared with FIB which yields samples with very similar thickness of 70 nm and which is thus considered constant. $\bar{S}$ and $\bar{V}$ are the average superficial area and average volume of a single precipitate, respectively. In this study, the precipitates have lenticular shapes. Since the ratio between the F_{max} and F_{min} is large, the lenticular shape can be approximated by a thin cylinder, the thickness of the cylinder δ equals to the minimum Feret diameter F_{min} of the precipitate, while the diameter of the cylinder D equals to the maximum Feret diameter F_{max}:

$$\bar{S} = \frac{1}{2}\pi D^2 + \pi D\delta, \qquad \bar{V} = \frac{\pi}{4} D^2 \delta$$

Therefore, the correction factor $k_t(V_v)$ can be expressed as:

$$k_t(V_V) = 1/[1 + t(\frac{1}{2\delta} + \frac{1}{D})].$$

With this correcting factor, it is possible to calculate the volume fraction of the precipitates from 2D images obtained with ACOM-TEM [97]. This correction factor is calculated with the assumption that the precipitates in the 3D structures have the same or similar size, which is assumed to be the case for stress assisted samples, as will be discussed later. For the stress-free aged sample, the variation in size can lead to a further decrease in volume fraction. The alternative direct method of transmission electron tomography, which is often used to build and quantify 3D structures, could not be applied in this case due to the dimensions of the precipitates embedded in a matrix which implies too large samples for current day electron tomography.

4.2.2 Quantitative calculating methods

Figure 4.3 shows the results for a stress free sample aged at 400°C for 100 h. Figure 4.3a shows the phase map obtained from the ACOM-TEM collection and treatment, and Figure 4.3b shows the conventional TEM bright field image where the region of the phase map is indicated by a dashed square. In such phase maps one can clearly distinguish the Ni_4Ti_3 precipitates from the Ni-Ti B2 matrix, enabling the use of such phase maps for quantitative shape and fraction analysis via image processing software such as ImageJ©. In the present maps, the Ni-Ti B2 phase is always considered as the background. In Figure 4.3a, the volume fraction of the Ni_4Ti_3 precipitates is 18.7% when measured directly using ImageJ© without any modification process. However, the image quality is not perfect, and the influence of the noise spots in the matrix and inside the precipitates must be considered. After noise reduction in both the matrix and the precipitates, the precipitate volume fraction is reduced to 17.7%. The quality of the image can be described by the variation of both corrections of noise reduction in matrix and precipitates. If σ is defined as the deviation of a volume fraction value calculated from the image with and without noise reduction, then σ can be described as:

$$\sigma = |(\bar{v} - v_{-}), (\bar{v} - v_{+})|_{max},$$

where $\bar{v}$ is the volume fraction with noise reduction in both the matrix and the precipitates;

v_- is the volume fraction value with noise reduction only in the matrix, and v_+ is the value with noise reduction only in the precipitates. The noise reduction v_- eliminates the dispersed noisy dots in the matrix by setting a threshold value so that the regions smaller than the threshold value will be wiped away from the matrix. The noise reduction v_+ counts the small holes inside the Ni_4Ti_3 precipitates as one piece of the precipitate. The quality of the phase map can thus be judged from the value of σ where a higher σ indicates a higher map quality, which means fewer noise spots in the image. According to the above equation, the volume fraction of a 400°C 100 h stress-free sample shown in Figure 4.3a is (17.7 $\pm$ 1.5)%.

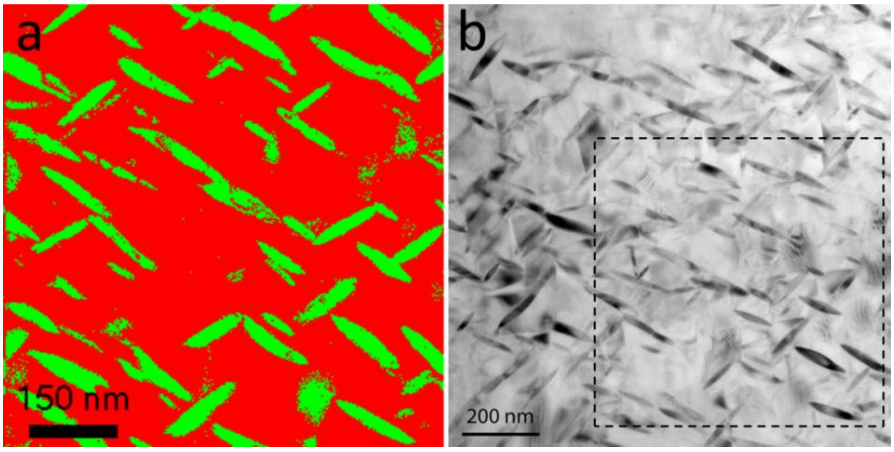

Figure 4.3 Stress-free sample aged at 400°C for 100 h. (a) Phase map taken from the region of the dashed square in b. (b) Conventional TEM bright field image.

4.2.3 Size and shape of Ni_4Ti_3 precipitates

Figures 4.4, 4.5 and 4.6 show the results for the samples aged under constrained conditions; for each of these, both tensile and compression sides were investigated. Further quantitative studies on the size and distribution of Ni_4Ti_3 precipitates are based on these phase maps. To investigate the effect of the aging conditions on the precipitates, quantitative data for the size and distribution of individual Ni_4Ti_3 precipitates must be acquired and analyzed. Maximum Feret diameter, minimum Feret diameter and aspect ratio are used to measure the difference in size of individual Ni_4Ti_3 precipitates. The maximum and minimum Feret diameters have been introduced in section 3.2.1 and correspond to the length and width of the precipitates in

this study. Aspect ratio is used to describe the geometrical shape of a particle and is the ratio of its size in different dimensions. In this study, the aspect ratio is the ratio between the Feret length and width of Ni_4Ti_3 precipitates. The average values of these parameters are presented in Table 4.1. Figure 4.7 shows the histogram of the maximum Feret diameter and aspect ratio of the alloys constraint-aged under different aging conditions and obtained from the phase map images, as shown in Figures 4.4, 4.5 and 4.6. The number of precipitates used for measuring and drawing the histogram in Figure 4.7 differs in different phase map images, ranging from 32 to 107 (the exact number of precipitates in each of the images Figure 4.4a,b, 4.5a,b and 4.6a,b is, respectively: 55, 107, 58, 63, 75, 32). In these figures, some short segments are shown in the phase maps, which are also included for quantitative calculation. Comparing these short segments with the corresponding TEM BF image, it can be seen that most of the segments belong to the Ni_4Ti_3 precipitates, but they have relatively weaker signals which decrease the quality of the DPs collected in the corresponding region, which eventually leads to the appearance of short segments instead of a long and complete particle. Therefore, the segments indeed belong to some precipitates, but appear as short parts instead of long and complete precipitates. For a precipitate that should be presented as a complete one but in fact shown as several segments, the total volume is still close to the sum of these segments but the average size is decreased, which means such segments influence the quantification on the size of precipitates but the influence on volume fraction of the precipitates is relatively small. As a result, the average size of the precipitates will decrease but the volume fraction will only slightly decrease due to this effect.

Table 4.1 Average sizes of Ni_4Ti_3 precipitates with standard error in alloys with different aging conditions.

		Maximum Feret diameter (nm)	Minimum Feret diameter (nm)	Aspect ratio
400°C 100 h	Tension	157 ± 13.7	23 ± 0.9	6.6 ± 0.4
	Compression	149 ± 11.0	27 ± 1.1	5.2 ± 0.3
	Stress free	90 ± 7.1	24 ± 1.4	3.8 ± 0.2
450°C 10 h	Tension	104 ± 11.6	20 ± 1.2	4.8 ± 0.3
	Compression	116 ± 8.3	23 ± 0.8	4.9 ± 0.2
450°C 100 h	Tension	237 ± 23.3	44 ± 2.2	5.1 ± 0.4
	Compression	204 ± 38.1	34 ± 3.4	5.2 ± 0.6

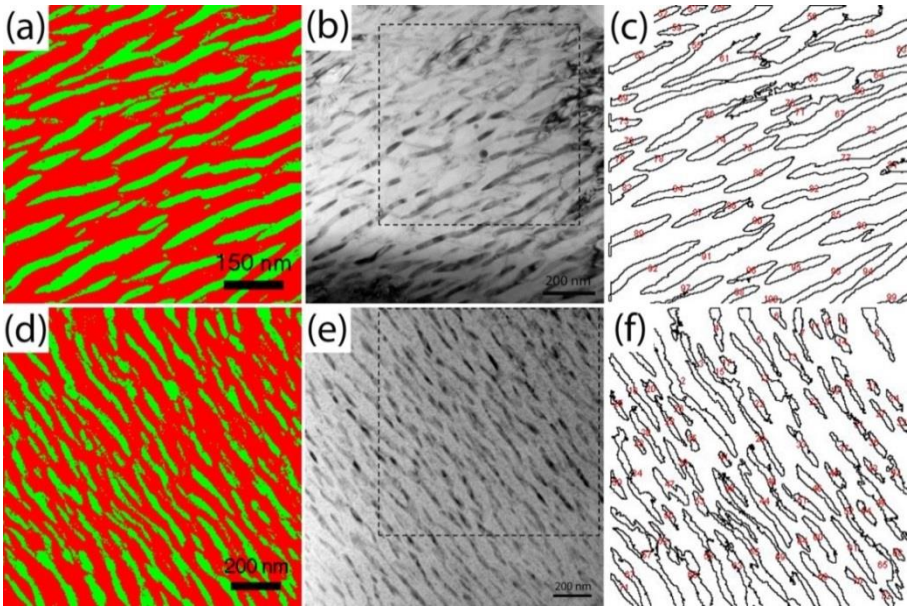

Figure 4.4 Constrained sample aged at 400°C for 100 h. (a) (d) Phase maps taken from the regions marked by dashed squares in (b) and (e), respectively. (b) (e) Conventional TEM bright field images; (b) from the tensile stress side and (e) from the compressive stress side. (c) (f) Outline maps obtained by Image J calculation indicating the recognition of precipitates, from (a) and (d), respectively.

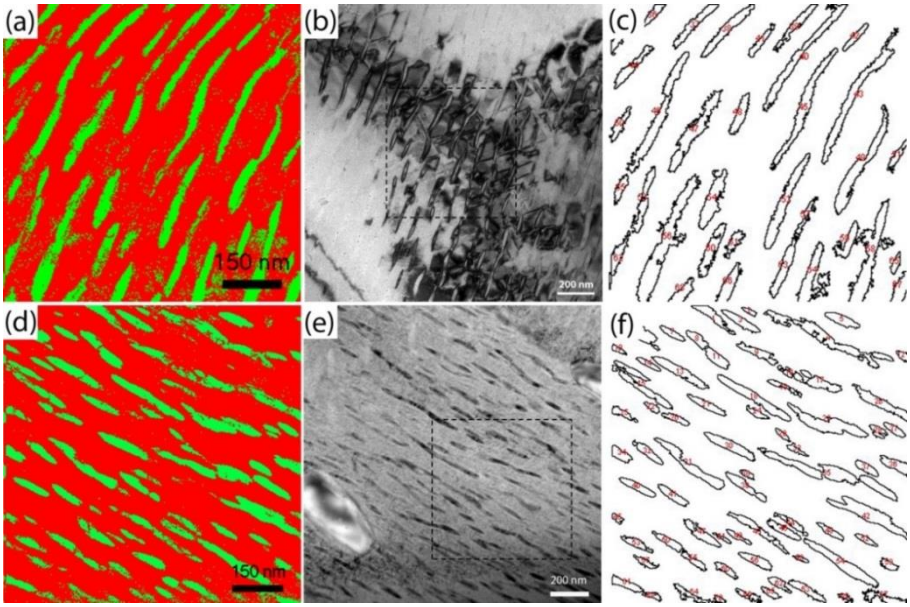

Figure 4.5 Constrained sample aged at 450°C for 10 h. (a) (d) Phase maps taken from the regions marked by dashed squares in (b) and (e), respectively. (b) (e) Conventional TEM bright field images; (b) from the tensile stress side and (e) from the compressive stress side. (c) (f) Outline maps obtained by Image J calculation indicating the recognition of precipitates, from (a) and (d), respectively.

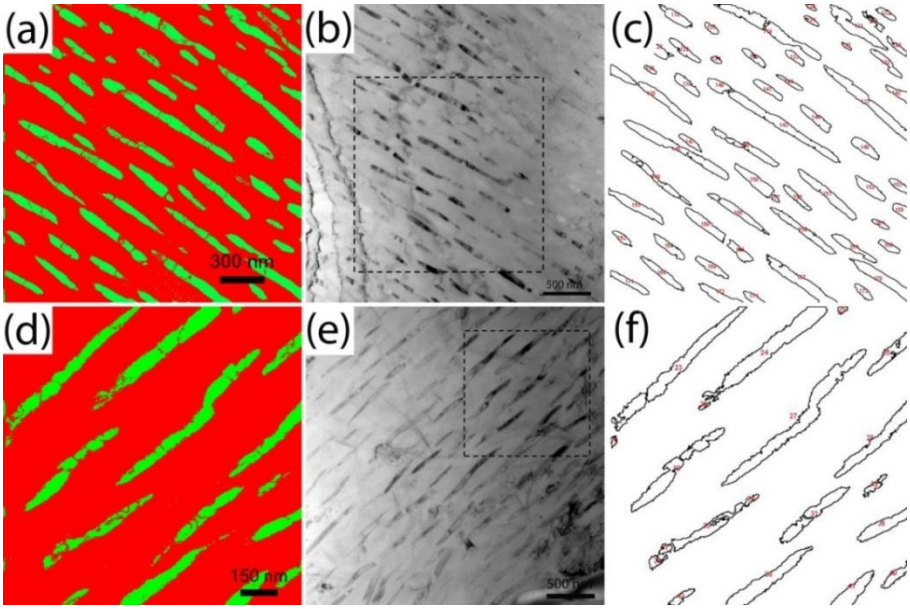

Figure 4.6 Constrained sample aged at 450°C for 100 h. (a) (d) Phase maps taken from the regions marked by dashed squares in (b) and (e), respectively. (b) (e) Conventional TEM bright field images; (b) from the tensile stress side and (e) from the compressive stress side. (c) (f) Outline maps obtained by Image J calculation indicating the recognition of precipitates, from (a) and (d), respectively.

Figures 4.7a and 4.7b show the variation of the maximum Feret diameter. From Figure 4.7a, it can be concluded that on the compression side of the alloy, the length of most precipitates is between 20 and 120 nm; when either the aging time or the temperature is increased, some precipitates with longer length start to appear, but the majority of the precipitates still remain under 120 nm. The appearance of these long precipitates may be due to end-to-end mergers between the two smaller precipitates, which become close to each other during precipitate growth; thus, a merged precipitate shows a much higher length in the viewing direction than regular individual precipitates. The preferential growth of a single Ni_4Ti_3 variant caused by constrained aging increases the likelihood that two precipitates will merge into a single precipitate since they have the same habit plane. In TEM observation, due to the influence of specimen thickness, there is also the possibility that two precipitates are overlapping along the viewing direction and should thus not be considered as one large precipitate. In the current work, the latter possibility is small because the viewing direction is not randomly determined but with a certain direction which decreases such effects. As illustrated in 4.1.2 and Figure 4.1c, the FIB specimens are prepared parallel or perpendicular to the external stress direction, and, as will be shown in section 4.3, the (111) habit plane of the precipitates is either parallel or perpendicular to the external stress direction which means that they are close to parallel with the viewing direction, reducing the possibility of overlapping along the viewing direction.

Figure 4.7b shows the length distribution of the Ni_4Ti_3 precipitates on the tensile side of the alloy. Similar to the compression side, an increase in either the aging time or temperature will lead to the appearance of longer precipitates that are a small fraction of the total amount of the precipitates. In addition to the similarity between the compression and tensile side, it was also found that the average length of the precipitates, as shown in Table 4.1, increased slightly on the tensile side compared to the compression side, and this difference in the precipitates' length contributes to the result that the volume fraction on the tensile side is higher than that on the compression side.

Figures 4.7c and 4.7d show the variation histogram of the aspect ratios under different aging conditions, which describes the ratio of the precipitates' length and width and provides more detail on the shape of the precipitates. This is a relevant parameter since it was reported that material with precipitates with higher aspect ratios which show a lenticular shape in 2D images will exhibit TWSME, while material with precipitates with lower aspect ratios and smaller sizes will exhibit an abnormal TWSME during the transformation process [98]. Figure 4.7c indicates that the aspect ratios are quite stable on the compression side for which the aspect ratios of most precipitates are in the range of 2-6 despite the different aging conditions. Figure 4.7d shows the results obtained on the tension side, and it is observed that the distributions of the aspect ratios are very similar to those on the compression side with the difference that the alloy aged at 400°C for 100 h exhibits a slightly higher aspect ratio compared to the alloys aged at 450°C for 10 and 100 h.

Table 4.1 shows the average value of maximum/minimum Feret diameter and aspect ratio of the Ni_4Ti_3 precipitates. The maximum and minimum Feret diameter slightly increase when aging time or temperature increase, and the aspect ratio stays almost constant. This implies that increasing the aging time or temperature from 400°C to 450°C or from 10 h to 100 h will lead to the growth of Ni_4Ti_3 precipitates in length and width, but the shape of the precipitates does not change too much. Figure 4.7 and Table 4.1 quantitatively shows the effects of the aging conditions on the size and shape of Ni_4Ti_3 precipitates. According to Table 4.1, The impact of aging temperature has a higher impact than aging time on the size of the precipitates. When aging temperature increases with about 7% (i.e., from 400°C to 450°C but counted in K) for the same 100 h the size of the precipitates increases with 35% to 50%, while when aging time increases with a factor of 10 from 10 h to 100 h at the same temperature of 450°C, the size of precipitates doubles. This shows that the aging temperature has a stronger impact than the aging time.

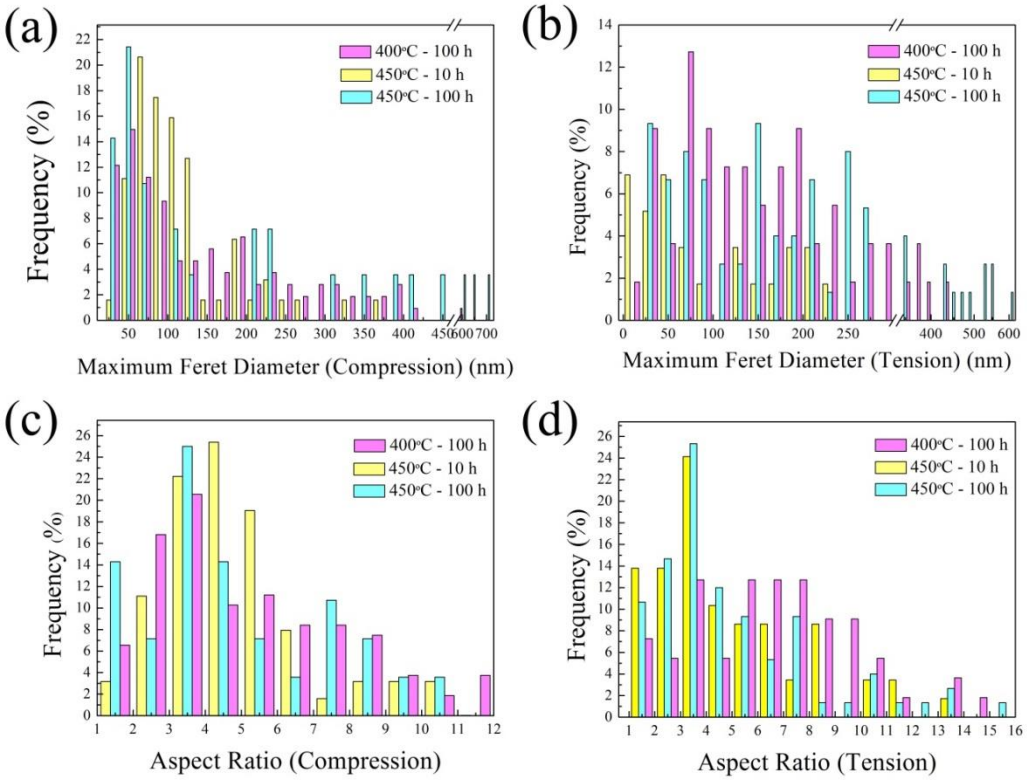

Figure 4.7 Maximum Feret diameter and aspect ratio of the Ni_4Ti_3 precipitates in constraint-aged alloys. Maximum Feret diameter for (a) the compressive stress side and (b) the tensile stress side. Aspect ratio for (c) the compressive stress side and (d) the tensile stress side.

4.2.4 Volume fraction of Ni_4Ti_3 precipitates

The volume fractions of the precipitates from these images are collected in Table 4.2 calculated with the equation in 4.2.1. An examination of all of these values shows that the sample aged at 400°C for 100 h under constrained conditions has the highest Ni_4Ti_3 density on both sides of the Ni-Ti alloy stripe. This result coincides with the highest recovery ratio observed under this aging condition [99], as is also indicated in Table 4.2. It can be understood that a higher density of Ni_4Ti_3 precipitates will enhance the impact of the stress fields around the coherent precipitates and provide a higher shape recovery force during the transformation process. When aging temperature is increased from 400°C to 450°C, the volume fraction of the Ni_4Ti_3 precipitates decreases, which is mainly because the solubility of Ni in the matrix is increased and less precipitates can nucleate and grow compared to the

alloy with lower aging conditions. Aging time also affects the volume fraction in the matrix but its influence is smaller compared to the temperature. When aging time increases, the growth of precipitates continues, which leads to the increase of the size of the precipitates as discussed in section 4.2.3, and eventually the volume fraction of the precipitates increases.

Table 4.2 Volume fraction of the Ni_4Ti_3 precipitates in the matrix from different samples.

	Tension side（%）	Compression side（%）	Recovery ratio (%) [99]
400°C - 100 h	10.6 ± 0.1	10.3 ± 0.2	92.86
450°C - 10 h	6.3 ± 0.1	5.8 ± 0.1	88.10
450°C - 100 h	8.6 ± 0.1	6.3 ± 0.1	42.86
400°C - 100 h stress free	5.5 ± 0.5		–

4.2.5 Spatial distribution of Ni_4Ti_3 precipitates

The spatial distribution of the Ni_4Ti_3 precipitates can be described by the interparticle spacing between each precipitate. The interparticle spacing of the Ni_4Ti_3 precipitates is calculated by the local thickness algorithm via an open-source plugin in ImageJ© software. At a given point in the Ni-Ti matrix region on a phase mapping image, the diameter of the largest sphere that fits completely inside the matrix region and includes the given point is defined as the local thickness of this given point. Since this method is not model based, it is unnecessary to make assumptions on the structural type, thus it is possible to assess a mean interparticle spacing value from the image, quantify the spread of the interparticle spacing from standard deviation and compare these values between different samples [100].

Figure 4.8 shows how the local thickness algorithm is applied on different samples to study the interparticle spacing between the Ni_4Ti_3 precipitates, with the calculated results presented in Table 4.3. The results show that among all of the aging conditions, aging at 400°C for 100 h leads to the smallest interparticle spacing, and aging at 450°C for 100 h leads to the largest interparticle spacing in constraint-aged alloys. This variation tendency of the interparticle

spacing coincides with the variation in the recovery ratio and volume fraction. Thus, it can be concluded that the alloy constraint-aged at 400°C for 100 h can obtain the highest recovery ratio since the highest volume fraction of Ni_4Ti_3 precipitates is observed, which can provide the highest internal strain field for the transformation process. The increase in the volume fraction of the Ni_4Ti_3 precipitates in the alloy under different aging temperatures is mainly achieved via the decrease of the interparticle spacings rather than the change in the size and aspect ratio of the precipitates. The changes in the distribution of the Ni_4Ti_3 precipitates also can be observed by measuring the number density of the precipitates, as shown in Table 4.4. Table 4.4 shows the number density of precipitates per 1000 × 1000 nm^2 and the results indicate that the number density on the tension side is usually higher than on the compression side, which can be explained by the notion that on the compression side more precipitates are well aligned and thus have a higher possibility to merge leading to a decrease of the number density. The main reason that the precipitates are well aligned on the compression side rather than tension side is because the external stress is perpendicular to the [101] habit plane of Ni_4Ti_3 precipitates, while on the tension side the external stress is parallel to the {111} habit plane. Indeed, when the external stress is parallel to the {111} habit plane, two orientation variants of the Ni_4Ti_3 precipitates can fulfil this relation with the external stress direction, but when the external stress is perpendicular to the {111} habit plane, only one variant is possible for the precipitates to fulfil the perpendicular relation with the external stress. Thus, on the compression side there is a higher possibility that the same Ni_4Ti_3 variant will appear and these precipitates will more rapidly touch and merge, and on 2D images these overlapped precipitates resemble one precipitate. The stress-free sample has the highest number density among all samples. This can be explained by the smaller size as well as the random distribution of the precipitates in the stress-free sample when compared to the constrained aged sample. A higher number density indicates that the nucleation rate of the precipitates in the stress free sample is high. However, when nucleated precipitates continue to grow the possible size that precipitates can reach is limited due to the random distribution of different

Ni_4Ti_3 variants. Therefore, the stress free aged sample has the largest number density, but smallest average size and volume fraction, which is accompanied with a larger interparticle spacing. From Table 4.4, it can be concluded that the change of number density has the same tendency as that of the interparticle spacing, which proves that the change of volume fraction is mainly achieved via the decrease of the interparticle spacings rather than the change in the size and shape of the precipitates. The distribution of Ni_4Ti_3 precipitates also shows differences under tensile and compression stress conditions during constrained aging process. It is concluded that tensile stress promotes the nucleation and growth of Ni_4Ti_3 precipitates since, according to our quantitative data, the length, aspect ratio, and volume fractions are all slightly higher on the tensile side than on the compression side. This difference can be explained based on the preferential growth of the Ni_4Ti_3 precipitate variants under external stress during the aging process. It is known that when aging under compressive stress, the Ni_4Ti_3 variant that has the $\{111\}_{B2}$ habit plane perpendicular to the stress direction will grow preferentially, while under tensile stress state, the Ni_4Ti_3 variant that has the$\{111\}_{B2}$ habit plane parallel to the stress direction will grow more effectively [62, 63, 102]. Since in constraint-aged alloys, all of the Ni_4Ti_3 precipitates are well-aligned and parallel, the change in the interparticle spacing will depend on the external stress condition. When compressive stress is applied, the change in the interparticle spacing will be restricted due to the interaction between the external stress and the internal stress caused by the precipitates. However, in a tensile stress aged alloy, the stress will not restrict the change in the interparticle spacing, leading to the higher density of the Ni_4Ti_3 precipitates, as shown in the schematic illustration of Figure 4.9.

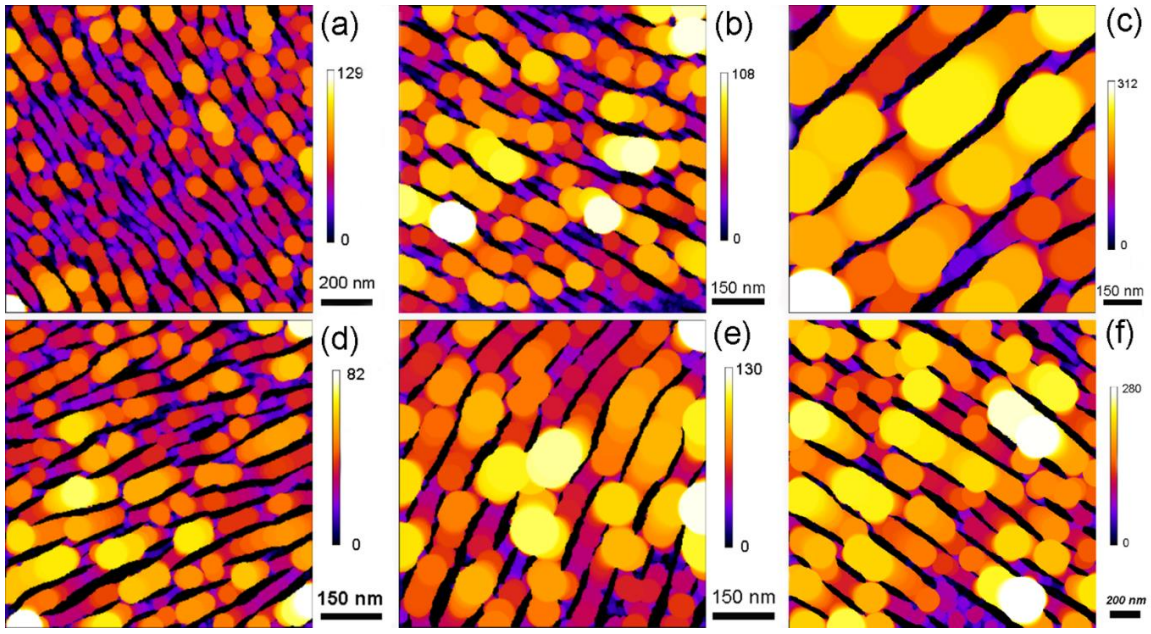

Figure 4.8 Interparticle spacing of Ni_4Ti_3 precipitates calculated by the local thickness method. (a) (b) and (c) Compressive stress sides for the samples aged at 400°C for 100 h, at 450°C for 10 h and at 450°C for 100 h, respectively. (d) (e) and (f) Tensile stress sides for the samples aged at 400°C for 100 h, at 450°C for 10 h and at 450°C for 100 h, respectively.

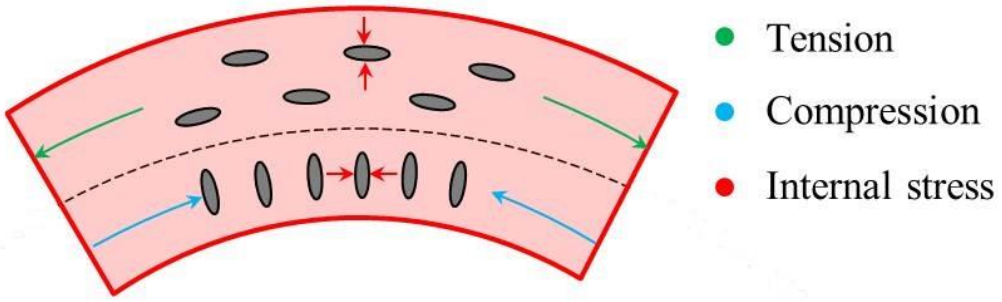

Figure 4.9 Schematic illustration of the relation between internal stress induced by precipitates and external stresses.

Table 4.3 Interparticle spacing of Ni_4Ti_3 precipitates in alloys with different aging conditions.

		Maximum (nm)	Mean (nm)	Standard Deviation (nm)
400°C - 100 h	Tension	82	32	22
	Compression	129	41	26
	Stress free	145	66	41
450°C - 10 h	Tension	130	63	35
	Compression	107	50	31
450°C - 100 h	Tension	278	146	81
	Compression	312	173	86

Table 4.4 Number density of Ni_4Ti_3 precipitates in alloys with different aging conditions.

Number density / 1000 × 1000 nm^2	400°C - 100 h			450°C - 10 h		450°C - 100 h	
	Tension	Compression	Stress free	Tension	Compression	Tension	Compression
	60	36	66	47	72	19	9

4.2.6 Influence of external stress during aging

Table 4.1 also shows the values for the volume fraction of the stress-free aged alloy, which are much lower than those for the alloy aged under the same time and temperature but with external stress. Thus, a quantitative comparison between the Ni_4Ti_3 precipitates aged with and without external stress under same aging time and temperature is also studied. Ke et al. [103] have simulated the influence of compressive stress on the size and shape of the Ni_4Ti_3 precipitates and found that the volume fraction of the precipitates will increase with increasing compressive stress, while the length and aspect ratio of the precipitates will only slightly increase but will remain below those in the unstressed state.

Figure 4.10 shows the quantitative experimental comparison of the results for the

stress-assisted and stress-free aging processes with both samples aged at 400°C for 100 h. Figure 4.10a shows the histograms of the lengths of the precipitates aged under tensile stress, compressive stress and without stress, respectively. The histograms indicate that most precipitates have similar lengths under all three conditions, while some precipitates with greater length can be observed in the constraint-aged alloys. However, since when the alloy was constraint-aged, precipitates were well-aligned in a parallel state, the likelihood that two precipitates will connect to form one larger precipitate increases. Taking this into account, it can be concluded that the variations in the precipitate length under different stress-assisted aging conditions are limited. For the stress free samples, since the growth of different Ni_4Ti_3 variants is along different directions, the appearance of large precipitates is less likely as their growth will be more easily halted by other precipitates when compared to the constrained aged condition where precipitates are aligned so they can all grow in the same direction. Figure 4.10b presents the histogram showing the comparison of aspect ratios, and it is observed that the precipitates in the compressive stress aged and stress-free aged alloys have very close aspect ratios, while the precipitates in the tensile stress aged side show slightly higher aspect ratios. Figure 4.10c shows how the local thickness method is applied for calculating the interparticle spacing for the stress-free aged alloy and the corresponding results are listed in Table 4.3. It is clear that the interparticle spacing of the Ni_4Ti_3 precipitates in the stress-free aged alloy is much higher than that in the constraint-aged alloys, coinciding with the result that the volume fraction of the precipitates in the stress-free aged alloy is much lower than in the constraint-aged alloys. The main origin of this difference in the volume fraction of the Ni_4Ti_3 precipitates is related to the orientation of the alloys and stress directions. Li et al. [104] reported that suction-cast alloys have very strong $<001>_{B2}$ fiber texture that will not be reduced by the subsequent aging process, and they have calculated the nucleation and growth of the Ni_4Ti_3 precipitates variants that are constraint-aged based on this $<001>_{B2}$ texture condition. They found that when the alloy has a $<001>_{B2}$ texture, the constraint stress will always be parallel to the $\{001\}_{B2}$ planes. According to their calculation,

two possible well-aligned Ni_4Ti_3 precipitate variants can occur rather than only one possible variant that occurs in the conditions where the relationship between the stress direction and grain orientation is completely random. Thus, the quantitative data obtained in our work is in accordance with the theoretical calculations carried out by Li et al., and the constraint-aged Ni_4Ti_3 precipitate variants have a higher probability of appearing in the matrix, eventually leading to the higher volume fraction of the precipitates compared to the stress-free aged alloys.

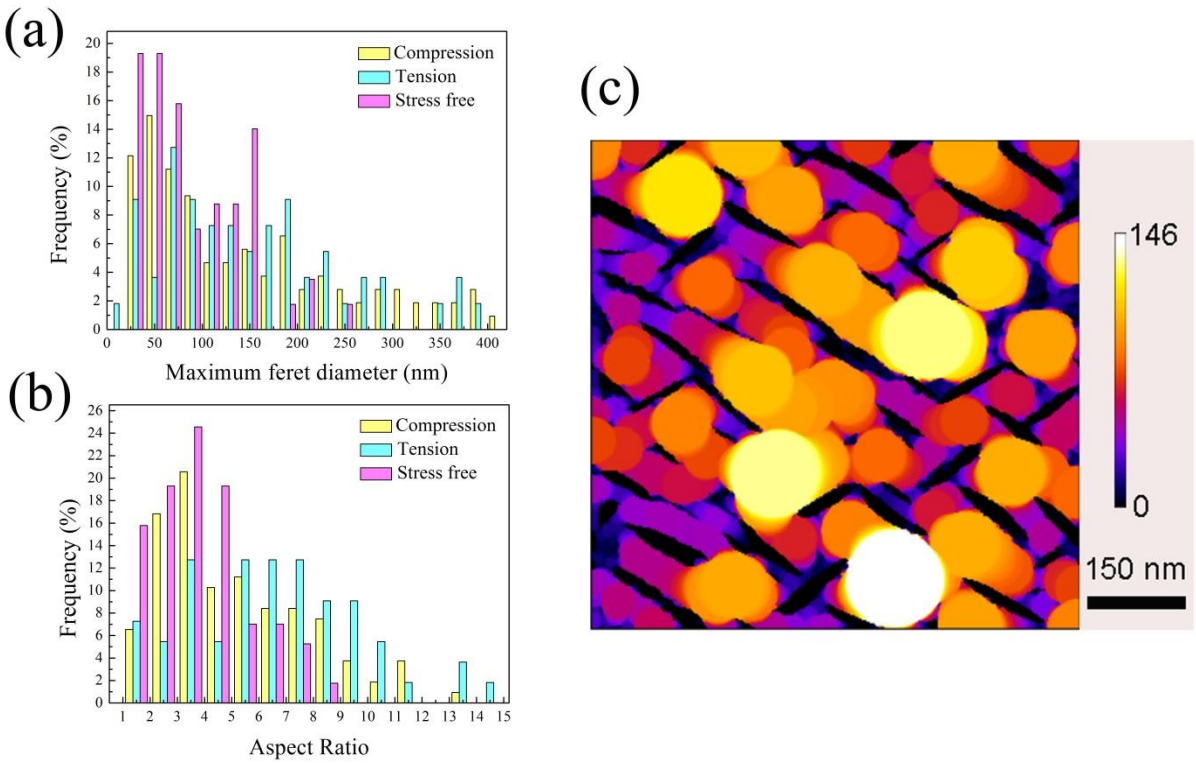

Figure 4.10 Quantitative histogram of the influence of the stress during aging on the Ni_4Ti_3 precipitates. (a) Maximum Feret diameter, (b) aspect ratio, (c) interparticle spacing.

4.3 Quantitative study of Ni_4Ti_3 precipitates in a $Ni_{51}Ti_{49}$ all-round shape memory alloy by TEM orientation mapping

4.3.1 Determination of the crystal orientation from the ACOM-TEM data

As already introduced in chapter 2, ACOM-TEM can display orientation maps from the observed TEM samples by collecting the diffraction patterns and matching them with preset

templates.

The original data of the crystal orientation obtained from ACOM-TEM is expressed in terms of the Euler angle; however, since the direction of the external stress has to be expressed in accordance with the crystal orientation in order to study their geometrical relationship, Miller indices are introduced as the spatial reference frame to express the orientation for further calculation. Thus, it is necessary to convert the Euler angles into Miller indices to express the crystal orientation of both the Ni-Ti B2 matrix and the Ni_4Ti_3 precipitates. When an Euler angle is converted into Miller indices, the final results are not unique but rather depend on the selection of different reference frames, so the definition of a fixed reference frame is the first step that must be carried out before the Euler angle is converted into Miller indices. Darbal A.D et al. suggested a frame of reference of the ASTAR device, in which *x* = horizontal (3 o'clock direction), *y* = vertical (12 o'clock direction) and *z* = normal (normal to the plane of the page) [101], as shown in Figure 4.11a; this reference frame is used in this study together with the conversion method from the Euler angle to Miller indices. In this study, the Textool© software was used to perform this conversion, giving the results in the form of one (*h k l*) plane and one [*u v w*] direction. Thus, matching the (*h k l*) plane and [*u v w*] direction with the reference frame of the ASTAR shown in Figure 4.11a, it can be concluded that the (*h k l*) plane is the observation plane of the acquired orientation images (the plane of the page), which corresponds with the *z* direction in ASTAR as the surface-normal direction; and the [*u v w*] direction corresponds with the *x* direction in the ASTAR reference frame. Figure 4.12 illustrates how this conversion and matching is performed from the ASTAR data. Figure 4.12a shows a screenshot from the data view interface of the ASTAR software that shows the Euler angle of each pixel on the top middle part indicated by a red circle; the observation region in this image is indicated by the black arrow on the top left side of the orientation map, and the diffraction pattern of this corresponding pixel can be seen in the window labeled *view 2*. The diffraction patters seen in this window is distorted because the camera and phosphor screen are not placed perpendicularly, as already mentioned in Chapter 2. The conversion

process from Euler angle into Miller indices is illustrated in Figure 4.12b, showing that the orientation of the selected pixel in Figure 4.12a is in the ($\bar{1}\ \bar{1}\ \bar{3}$) zone axis and the direction is [3 0 $\bar{1}$]. Figure 4.12c shows the diffraction patterns of the (1 1 3) zone axis in Ni-Ti B2, and both the normal diffraction patterns taken from conventional TEM diffraction and the distorted diffraction pattern are displayed; the normal diffraction pattern was adjusted to the same distortion ratio as the diffraction patterns shown by ASTAR. The white arrows in the diffraction patterns indicate the [$\bar{3}$ 0 1] spots. Since the [$\bar{3}$ 0 1] direction in the (1 1 3) zone axis is equal to the [3 0 $\bar{1}$] direction in the ($\bar{1}\ \bar{1}\ \bar{3}$) zone axis, it is observed that the 3 o'clock horizontal direction is the [3 0 $\bar{1}$] direction, indicating that the reference frame discussed above fits well in this conversion process between Euler angle and Miller indices.

From the above discussion it is already clear that the [*u v w*] direction which was converted from the Euler angles is the 3 o'clock direction on the orientation mapping image as the default reference frame. However, this default reference frame can be rotated in the Mapviewer software using the File/Preference menu. A 90° counterclockwise rotation can be directly imposed, and after this rotation, the [*u v w*] direction will be along the 12 o'clock direction, as shown in Figure 4.11b. This rotation operation of the reference frame is applied because it will simplify the calculation process of the relation between the reference frame and the external stresses. Therefore, in what follows, the reference frame will always undergo a 90° rotation in order to keep the [*u v w*] direction along the 12 o'clock direction on the TEM or mapping images and this rotation will not explicitly be mentioned again.

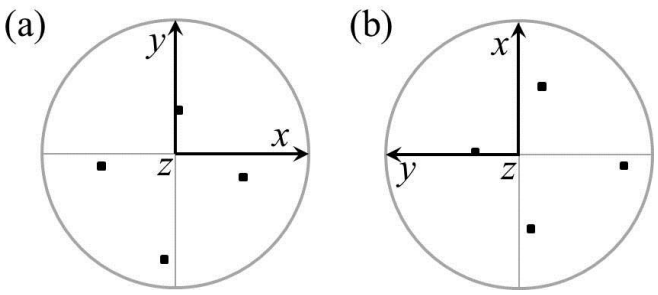

Figure 4.11 An example of a 111 pole figure in the ASTAR frame of reference. (a) Original reference frame, and (b) 90° counterclockwise rotated reference frame.

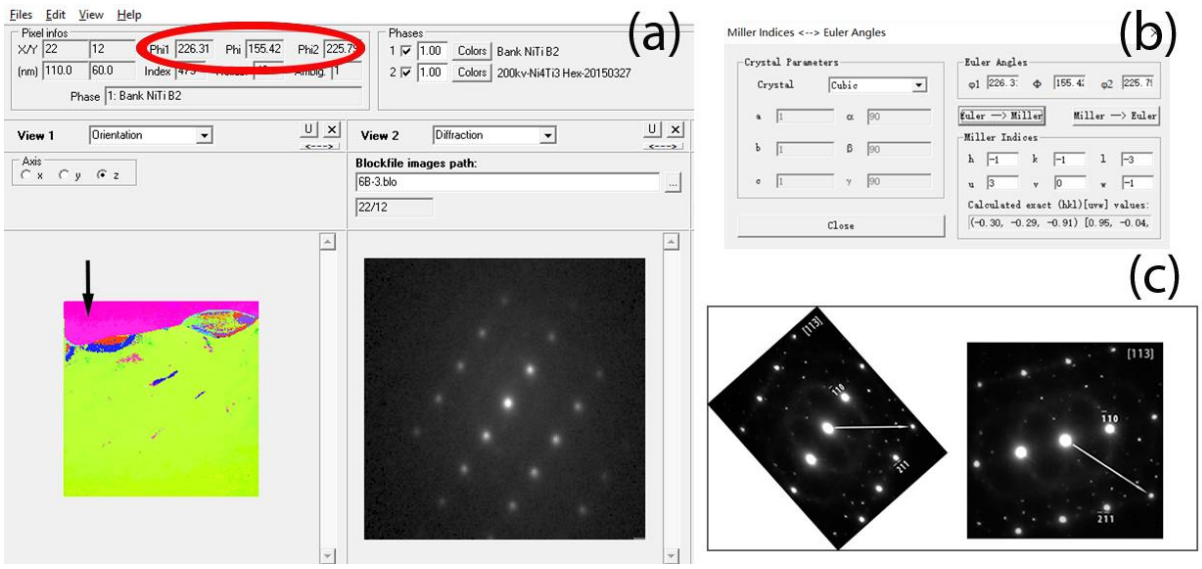

Figure 4.12 An illustration of the conversion from Euler angle into Miller indices and determination of the reference frame: (a) screenshot from the Mapviewer software showing Euler angle, orientation map and diffraction patterns, (b) screenshot from the Textool software showing the conversion from Euler angle to Miller indices, (c) normal and distorted diffraction patterns of [113] Ni-Ti B2 in accordance with the diffraction pattern shown in (a).

4.3.2 Relation between external stress and microstructure observed by TEM

In this study, the influence of external stress on the nucleation and growth of the Ni_4Ti_3 precipitates in a polycrystalline alloy during aging was studied by ACOM-TEM, with the results displayed as nanoscale orientation maps. However, the direction of the external stress applied during aging was described on the macroscale as shown in Figure 4.1c. Hence, it is necessary to link the direction of the external stress to the orientations of the TEM specimens in order to investigate the relationship between the stress and the Ni_4Ti_3 variants. This was achieved by cutting the TEM specimens from specific directions on the Ni-Ti alloy stripes by using FIB for TEM specimen preparation. Figure 4.13 shows the relation between external stress and the different TEM specimen positions. Figure 4.13a shows how two FIB samples (A and B) are orientated in the bulk Ni-Ti alloy stripe while Figures 4.13b and 4.13c show how these two FIB samples are placed in the TEM for observation. Both sample A and B has one green edge in Figure 4.13, which is used to record the change of FIB sample's orientation

from the bulk alloy to the TEM. The red colour in the figure always indicates the direction of external stress. In these two figures the z axis is the direction of the incident beam and the xy plane is the plane of the phosphor screen where the TEM images are recorded.

It can be seen from Figure 4.13a that for specimen A, the stress direction is perpendicular to the plane of the FIB specimen which is the z direction in Figure 4.13b while for specimen B the stress direction is parallel to the plane of the specimen. Meanwhile, in Figure 4.13a, the stress direction is parallel to the green edge of specimen B and according to Figure 4.13c, this becomes the x direction.

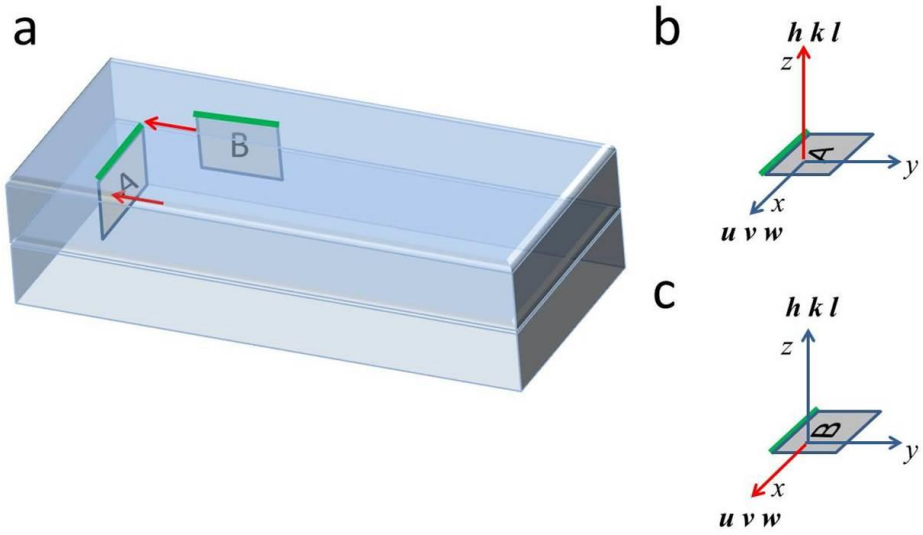

Figure 4.13 An illustration of the relation between external stress and crystal orientation in different FIB samples (A and B). (a) FIB sample positions of constrained aged Ni-Ti stripes, red arrows indicate stress directions. (b) reference system for sample A, and (c) reference system for sample B.

Since the specimens are viewed along the *z* direction, the observed image is on the *xy* plane with *x* is 6 o'clock direction while *y* is 3 o'clock direction on the image. According to the discussion in section 4.3.1, the *x* direction is the [u v w] direction when the crystal orientation is converted from Euler angles into Miller indices, and the *z* direction is the [h k l] direction which is the surface normal of the (h k l) plane. The relation between external stress and

Miller indices of the crystal can thus be determined based on these relations. For specimen A, the z direction is both the direction of external stress and the [h k l] viewing direction, as shown in Figure 4.13b, hence it is possible to use the [h k l] direction to represent the direction of external stress in specimen A. For specimen B, the x direction is both the direction of external stress and the [u v w] direction, as shown in Figure 4.13c, hence it is possible to use the [u v w] direction to represent the direction of external stress in specimen B.

4.3.3 Influence of external stress during aging on the growth of Ni_4Ti_3 precipitate variants when external stress has a random relationship to the crystal orientation of the Ni-Ti B2 grains

The goal of this study is to determine the geometrical relationship between the external stress and the orientation of the Ni_4Ti_3 precipitates and the Ni-Ti B2 matrix. The external stress is applied at the macro-scale and is directly related with the geometry of the bulk Ni-Ti alloy strip, while the orientation of the Ni_4Ti_3 precipitates is defined from micro-scale and related to the grain orientation. Therefore, the key idea to relate these two bases from different scales is to set them at the same scale. In this study, the direction of the external stress is expressed in Miller indices which means, in this way, the information of external stress is expressed at the micro-scale. In the process of expressing the external stress by Miller indices, one of the possible reasons to cause an uncertainty in the relation is that the correlation between the direction of the bulk material and TEM images is inaccurate. This problem has very small influence in this study because all TEM samples are prepared by site- and orientation-specific FIB which means that the relation between the bulk material and TEM samples can be controlled during TEM sample preparation. When the FIB sample is mounted on a dedicated TEM grid and placed into a TEM, the relation between the observed image to the TEM samples can be matched easily according to the shape of the FIB sample on the grid. The main error that may occur is when putting the FIB samples into the TEM holder by hand, but

also this influence can be minimized since FIB samples have clear features to determine their orientation in the holder. An estimate of the possible misorientation was made by measuring the orientation of a selected sample in the holder, as seen in Figure 4.14 and was found to be at most 3°. Therefore, relating the macro-scale stress to the local stress will not cause too large errors and the Miller indices acquired from the TEM results can thus be used to represent the direction of the external stresses.

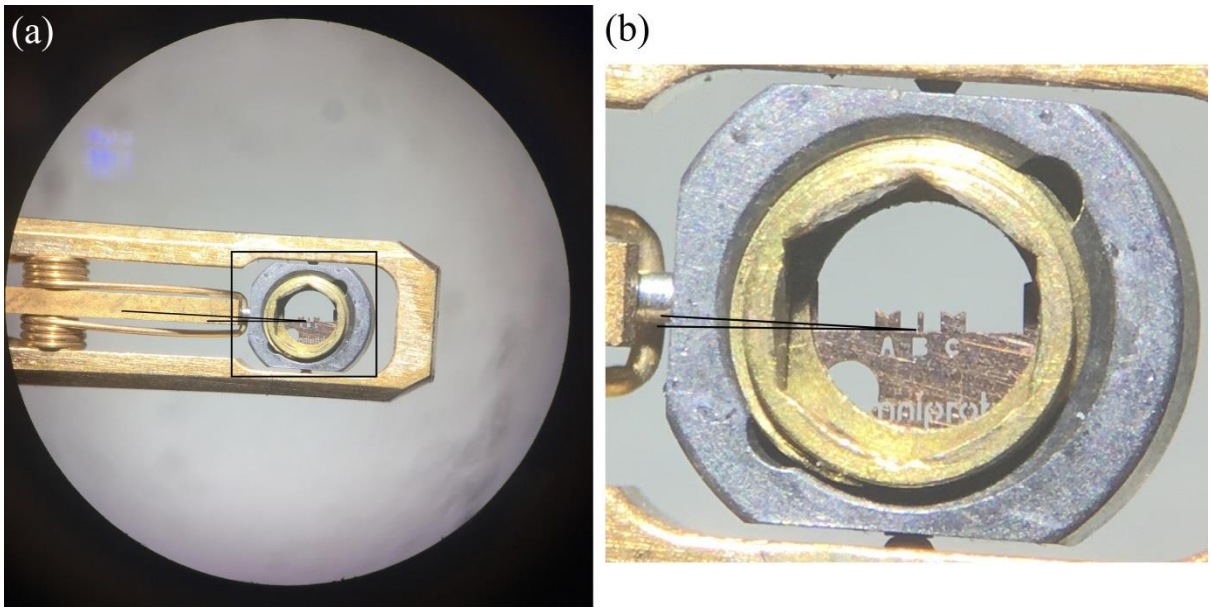

Figure 4.14 An illustration of a FIB sample on the TEM grid placed in the TEM holder. (b) Magnified image from the region indicated by black rectangle in (a). Two black lines indicate the direction of FIB sample and axis of TEM holder, respectively, showing a slight misorientation.

Following the discussion in 4.3.1 and 4.3.2, the orientations of the stress, precipitates and matrix can all be expressed by Miller indices. Thus, the angle between the stress and precipitate and between the stress and the matrix can be calculated mathematically. The crystal orientation relationship between the precipitates and the matrix is described as $(001)_H$ // $\{111\}_{B2}$, $[010]_H$ // $[\bar{2}\,\bar{1}\,3]_{B2}$, where the subscript H refers to the hexagonal lattice of the Ni_4Ti_3 precipitate and B2 to the cubic structure of the matrix [105]. Since the $(111)_{B2}$ plane is the central habit plane of the precipitates and the precipitate is mostly flat in the direction

perpendicular to this plane, using this plane as the reference plane to compare the angles with external stress will simplify the calculation process. As discussed above, the external stress can be expressed either by the surface normal of the (h k l) plane or by the [u v w] direction in different TEM samples, so the calculation will use either the (h k l) or [u v w] values. It is easy to prove that the angle of the two surface normal directions is equal to the angle of the corresponding planes, so the angle of the two (h k l) planes, which can be calculated directly from the crystallographic software, will be used to replace the angle in the two surface normal directions. Figure 4.15 shows the orientation maps of all the samples involved in this study. The orientation maps have the same scanning regions as the phase maps shown in Figures 4.3, 4.4 and 4.5, with different colors representing the variation of the orientations based on the pole figures.

Two orientation maps will be explained in the following discussion as examples to directly describe in detail how the calculations were conducted. The first example uses the data from the alloy aged at 450°C for 10 h on the tensile side, the orientation map of which is displayed in Figure 4.15b. The stress direction in this orientation map is perpendicular to the observation plane which means that the stress direction can be represented by the (h k l) values from the converted Euler angles. From the orientation map, the Euler angles for both the Ni-Ti B2 matrix and Ni_4Ti_3 precipitates can be read directly and after converting these two sets of Euler angles, the Miller indices of the B2 matrix and the Ni_4Ti_3 precipitates are then expressed as follows: in the Ni-Ti B2 matrix, the crystal orientations are (2 0 3) and [3 1 $\bar{2}$] in the cubic structure while in the Ni_4Ti_3 precipitate, the orientations are (8 0 1) and [0 2 $\bar{3}$] in the hexagonal structure. Thus, $(2\ 0\ 3)_{B2}$ and $(8\ 0\ 1)_H$ will be used to represent the external stress direction in the cubic and hexagonal structures, respectively. The angle between the Ni_4Ti_3 precipitate and external stress can be calculated as the angle between the two plane of $(0\ 0\ 1)_H$ and $(8\ 0\ 1)_H$, and is 76.5°. This angle between the external stress and the Ni_4Ti_3 precipitate indicates that during the constrained aging process the preferentially grown precipitates tended to have a relatively larger angle to the stress direction under the tension

stress.

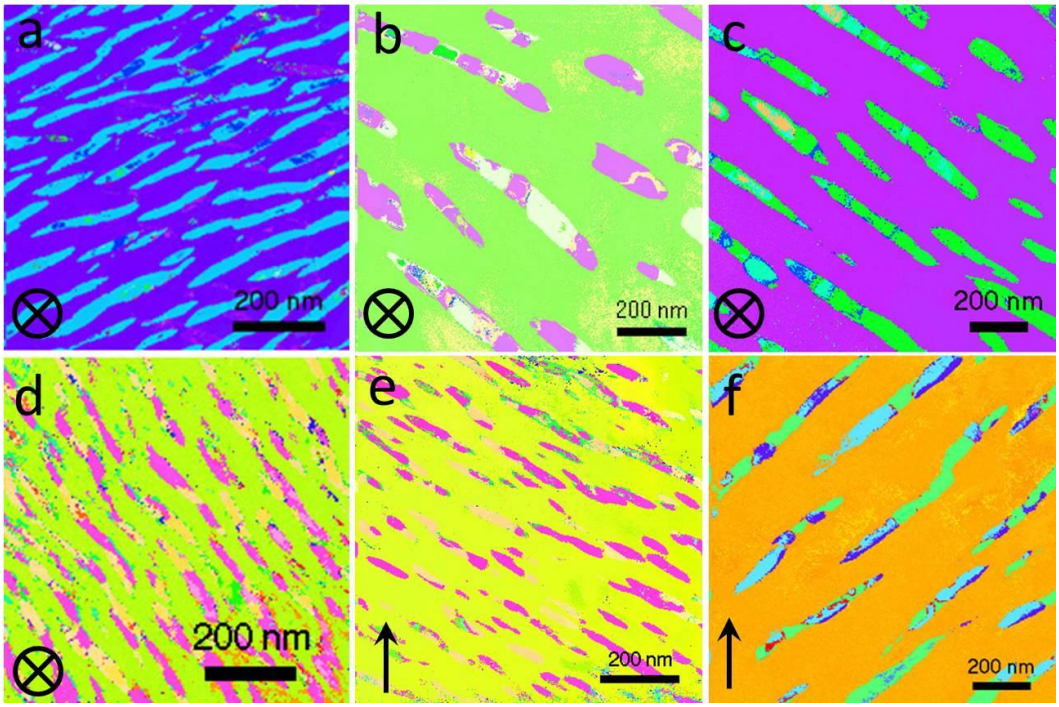

Figure 4.15 Orientation maps of the Ni-Ti alloys constrained-aged at various aging times and temperatures, corresponding to the phase map images in Figures 4.3-4.5: (a) and (d) aged at 400°C for 100 h, (b) and (e) aged at 450°C for 10 h, (c) and (f) aged at 450°C for 100 h, (a), (b) and (c) are under tension stress, (d), (e) and (f) are under compression stress. The direction of external stress is indicated at the left bottom corner of the image with black arrows.

The orientation in the B2 structure can be used to determine the exact Ni_4Ti_3 variant by comparing the angles between $\{1\ 1\ 1\}_{B2}$ and stress with the angle between the Ni_4Ti_3 precipitate and stress. In the cubic structure of this example, the angle between $(2\ 0\ 3)_{B2}$ and $(1\ 1\ 1)_{B2}$ is 36.81°, the angle between $(2\ 0\ 3)_{B2}$ and $(1\ \bar{1}\ \bar{1})_{B2}$ is 80.79°, the angle between $(2\ 0\ 3)_{B2}$ and $(1\ \bar{1}\ 1)_{B2}$ is 36.81° and the angle between $(2\ 0\ 3)_{B2}$ and $(\bar{1}\ \bar{1}\ 1)_{B2}$ is 80.79°. This means that if all four different Ni_4Ti_3 variants could appear, two of them would have larger angle (80.79°) with external stress during constrained aging, while the other two variants would have the smaller angle (36.81°). In fact, only the variants which have the largest angle with the external stress will grow during constrained aging while the growth of the other

variants will be suppressed.

The second example uses the data from the alloy aged at 450°C for 10 h on the compression side with the corresponding orientation map displayed in Figure 4.15e. The stress direction in this orientation map is vertical on the image as indicated by the black arrow, which means that the stress direction can be represented by the [u v w] values from the converted Euler angle; the subsequent angle calculation will be based on the [u v w] values. It must be mentioned that in a hexagonal structure, the surface normal of the (0 0 1) plane is the [0 0 1] direction. After converting the Euler angle into Miller indices for this example, the B2 matrix and Ni_4Ti_3 precipitates can be expressed as follows: in the Ni-Ti B2 matrix, the crystal orientations are (1 0 2) and $[\bar{2}\ \bar{1}\ 1]$ in the cubic structure, while for the Ni_4Ti_3 precipitate, the orientations are $(\bar{7}\ \ 0\ \ \bar{1})$ and $[\bar{1}\ \bar{1}\ 7]$ in the hexagonal structure. In this case, $[\bar{2}\ \bar{1}\ 1]_{B2}$ and $[\bar{1}\ \bar{1}\ 7]_H$ will be used to represent the external stress direction in the cubic and hexagonal structures, respectively. The angle between $[0\ 0\ 1]_H$ and $[\bar{1}\ \bar{1}\ 7]_H$ is 17.5°. This indicates that during the constrained aging process, the preferentially grown precipitates tend to have a relatively smaller angle to the stress direction under compression stress.

Orientation maps from the alloys aged at 400°C for 100 h and at 450°C for 100 h on both the tension and compression sides were obtained and were calculated in a similar manner as described above. The Miller indices converted from Euler angles of all of these orientation maps are shown in Table 4.5, where the bold printed numbers indicate the values that will be used to represent the external stresses in the corresponding orientation maps; these values were used in the calculation of the relation between the stresses and the Ni-Ti B2 matrix and Ni_4Ti_3 precipitates, and the calculated results are shown in Table 4.6.

Table 4.5 Miller indices converted from Euler angles of the orientation maps under different aging conditions.

		B2		Ni_4Ti_3	
		(*h k l*)	[*u v w*]	(*h k l*)	[*u v w*]
400°C, 100 h	Tension	**(1 1 3)**	[5 2 $\bar{3}$]	**(9 $\bar{3}$ 1)**	[0 1 6]
	Compression	**($\bar{5}$ $\bar{1}$ $\bar{6}$)**	[3 $\bar{1}$ $\bar{2}$]	**(0 $\bar{1}$ $\bar{1}$)**	[$\bar{1}$ 0 0]
450°C, 10 h	Tension	**(2 0 3)**	[3 $\bar{1}$ 2]	**(8 0 1)**	[0 2 $\bar{3}$]
	Compression	(1 0 2)	**[$\bar{2}$ $\bar{1}$ 1]**	($\bar{7}$ 0 $\bar{1}$)	**[$\bar{1}$ $\bar{1}$ 7]**
450°C, 100 h	Tension	**(1 1 3)**	[$\bar{3}$ 1 1]	**(3 $\bar{1}$ 0)**	[1 3 $\bar{3}$]
	Compression	(1 0 3)	**[6 3 $\bar{2}$]**	($\bar{2}$ $\bar{3}$ $\bar{1}$)	**[0 1 $\bar{4}$]**

Table 4.6 Relationship between the external stress, Ni-Ti B2 matrix and Ni_4Ti_3 precipitates.

T = tension C = compression		B2 (Cubic)					Ni_4Ti_3 (Hexagonal)	
		Stress	Angle				stress	Angle
			(111)/ [111]	($1\bar{1}\bar{1}$) / [$1\bar{1}\bar{1}$]	($1\bar{1}$1) / [$1\bar{1}$1]	($\bar{1}\bar{1}$1) / [$\bar{1}\bar{1}$1]		(001) / [001]
400°C 100 h	T	(1 1 3)	29.5°	58.5°	58.5°	80.0°	(9 $\bar{3}$ 1)	76.5°
	C	($\bar{5}$ $\bar{1}$ $\bar{6}$)	28.4°	81.6°	42.8°	90°	(0 $\bar{1}$ $\bar{1}$)	27.7
450°C 10 h	T	(2 0 3)	36.8°	80.8°	36.8°	80.8°	(8 0 1)	76.6°
	C	[$\bar{2}$ $\bar{1}$ 1]	61.9°	61.9°	90°	19.5°	[$\bar{1}$ $\bar{1}$ 7]	17.5°
450°C 100 h	T	(1 1 3)	29.5°	58.5°	58.5°	80.0°	(3 $\bar{1}$ 0)	90°
	C	[6 3 $\bar{2}$]	54.7°	65.6°	85.3°	24.9°	[0 1 $\bar{4}$]	28.8°

In Table 4.6, the angle between the habit plane of the Ni_4Ti_3 precipitates and the external stress is shown in the column labelled Ni_4Ti_3 (hexagonal), and a clear tendency is observed: under the compression conditions, the angle is smaller, and under the tensile conditions, the

angle is larger. The column B2 (cubic) shows the possible distribution of all of the four Ni_4Ti_3 variants in view of the cubic structure and expressed in relation to the external stress. If the alloys were aged without the external stress, all four Ni_4Ti_3 variants could grow as indicated in the four columns under B2/Angle; however, the applied external stress during aging suppressed the growth of three variants, and only the remaining variant could grow preferentially in the regions observed in this study. By comparing all of the four possible Ni_4Ti_3 variants as described in the cubic structure to the real observed Ni_4Ti_3 variant as described in the hexagonal structure, it is easy to find which Ni_4Ti_3 variant grew preferentially, while its relationship with the external stress is obtained at the same time. From the data presented in Table 4.6, it can be concluded that under the tensile conditions, the Ni_4Ti_3 variant that has the largest angle with stress will grow, while under compression conditions, the Ni_4Ti_3 variant with the smallest angle with stress will grow. Errors exist when determining the direction of external stresses since the determination of the stress direction was based on the position of the TEM specimens in the holder, and this position could be changed slightly because the horizontal line in the TEM holder is measured by the naked eye. Moreover, when the Euler angle is converted into Miller indices, the number of decimal places was reduced for the final values, also giving rise to a deviation in the calculation of the angles. Taking all these effects into account, the error of the final angles can numerically be estimated as ±5°, but this error remains small enough to allow the determination of the Ni_4Ti_3 variants based on these angles. Despite the ±5° calculation error of the angles, it is still possible to determine from the data in Table 4.6 that when the alloy was constrained-aged at 400°C for 100 h, the $(\bar{1}\ \bar{1}\ 1)$ Ni_4Ti_3 variant will grow preferentially on the tensile side, and the (1 1 1) variant will grow preferentially on the compression side, as was confirmed by comparing the angle obtained from the hexagonal structure to the four angles obtained from the cubic structure. On the tensile side of the alloy, which was constrained-aged at 400°C for 100 h, the $(\bar{1}\ \bar{1}\ 1)$ variant has the largest angle with external stress compared to the other three variants, and on the compression side, the (1 1 1) variant has the smallest angle with

external stress compared to the other three variants. Similar situations can be observed for the alloys constrained-aged at 450°C for 10 h and 100 h.

When alloys were constrained-aged in this study, there was a random relationship between the external stress and the crystal orientation of every grain. From the results presented in Table 4.6, it can be concluded that in the alloys where the relationship between the crystal orientation of the grains and the external stress applied during aging was random, the Ni_4Ti_3 variant that has the largest angle with the external stress will grow preferentially under tensile stress, and the variant that has the smallest angle with the external stress will grow under compressive stress, which confirms the earlier works on single crystals [43, 61, 63].

4.4 Discussion

4.4.1 Texture in the alloy

In the present material treatments, the curvature of the iron mold used for the constrained aging process was specially designed to introduce a strain of 1% for the Ni-Ti alloy stripes placed inside the mold, and according to practical tests and literature [106], this strain is the maximum elastic strain for such size metal stripes under such deformation condition. From conventional mechanics, it is known that the stress distribution in a bent alloy stripe varies in different regions. A neutral plane, which feels no strain during bending, exists in the middle of the stripe and parallel with the surface planes. On one side of this neutral plane, a positive strain is introduced by the tensile stress, while on other side of the neutral plane, a negative strain is introduced due to the compressive stress on this side, as shown in Figure 4.1b. The stress value varies in different regions inside the stripe, with a higher stress level occurring closer to the surface of the alloy. This study did not discuss the influence of the stress levels but rather focused on the heterogeneity of the Ni_4Ti_3 precipitates, unlike many studies reported in the literature that were discussed in Chapter 1. When the Ni-Ti alloy stripes were casted in a copper mold, the rapid solidification process induces a strong texture in the alloy.

Such strong {001} solidification texture was confirmed in this case by XRD and EBSD analysis [99], and this texture affected the final properties of the Ni-Ti alloy in different ways. On the one hand, the texture appeared due to the rapid solidification process of the alloy stripe, since the shape of the stripe is 70 × 8 × 0.5 (length × width × thickness), the fastest solidification occurs on the thickness (0.5 mm) direction. Such process leads to the appearance of small size grains growing along the thickness direction as well as the supersaturation of Ni in the Ni-Ti B2 matrix, both effects favoring the formation of relatively small and dispersive distributed Ni_4Ti_3 precipitates because small size grains restrict the size of precipitates and supersaturation of Ni in B2 promotes the nucleation of precipitates. The strong texture greatly reduced the heterogeneity of crystal orientations in the alloy, yielding most grains having very close orientations, which promotes the accuracy of a quantitative estimation of Ni_4Ti_3 precipitates. Although the measured grains are limited, these grains always show a $[001]_{B2}$ crystal orientation, from which we deduce that these grains can represent most of the grains in this study. On the other hand, the texture affects the appearance of different Ni_4Ti_3 variants. Li. et al. found that the possible variants which can grow during constrained aging in the {001} textured alloy are restricted [104]. In this study, only one variant of Ni_4Ti_3 precipitates grows inside one grain when external stress has a random relation with grain orientation, but considering a sum of various grains, all four variants would have the opportunity to appear if there is no texture in the alloy. However, the {001} texture will lead to the stress direction parallel to <uv0> which means the stress direction is always parallel to the {001} plane. After a series of calculations by considering all situations, it was concluded that a maximum of two variants instead of four will appear inside the alloy in different grains during constrained aging condition. Therefore, the existence of {001} texture in the alloy can promote the formation of small Ni_4Ti_3 variants well orientated with only one or two variants, which finally leads to a higher recovery ratio of TWSME in this study.

4.4.2 R phase transformation temperature

The differences in the R phase transformation temperature caused by the different aging time and temperature were investigated by Li et al. [99]. Figure 4.16 shows the DSC curves of a $Ni_{51}Ti_{49}$ alloy after constrained aging at different aging time and temperature. The red curves are partial DSC results which are used to separate the reverse transformation peak of R phase from that of martensite. This work showed that among all of the constraint-aged alloys in this study, the 400°C and 100 h aged alloy presents the highest R phase transformation temperature, and the 450°C and 10 h aged alloy presents the lowest R phase transformation temperature. R_s, R_f, R_s' and R_f' all show the same tendency for the influence of the aging treatment; therefore, these four parameters will not be discussed separately, and instead, R_s will be used in the following discussion to represent the R phase transformation temperature. The effects of the aging time and temperature on the R phase transformation were investigated in a stress-free aged $Ni_{51}Ti_{49}$ alloy [107], showing that for aging at higher temperatures (400°C - 500°C), R_s is constant with increasing aging time while increasing aging temperature will lead to the decrease in equilibrium R_s. The influence of the aging temperature on R_s is mainly due to the solubility of Ni in the Ni-Ti matrix under different temperatures; indeed, a higher aging temperature results in a higher solubility in the matrix and lower R_s temperature, thus explaining that the R_s temperature of 400°C and 100 h aged alloy is higher than the R_s temperatures of the alloys aged at 450°C for both 10 h and 100 h. The quantitative results obtained on the volume fraction of the Ni_4Ti_3 precipitates also correspond to the change of R_s temperature. For the 400°C and 100 h aged alloy the highest volume fraction of Ni_4Ti_3 precipitates is observed, which leads to a decrease of Ni concentration in the matrix, which yields an increase in the R_s temperature [95, 107]. Therefore, the alloy with a highest volume fraction of Ni_4Ti_3 precipitates will show the highest R_s temperature.

When the aging time was prolonged from 10 h to 100 h at 450°C, the situation is slightly different in that the R_s temperature increased slightly while the volume fraction is decreased in which a decrease in R_s temperature should be expected. This phenomenon could be caused

by the continuous growth of the Ni_4Ti_3 precipitates at prolonged aging times. The main difference between the distributions of the Ni_4Ti_3 precipitates aged at 450°C for 10 h and 100 h is the difference in the interparticle spacing that changed from 63 nm to 146 nm on the tension side when the aging time is prolonged from 10 h to 100 h, as indicated in Table 4.2. Since the standard deviation of the interparticle spacing under this parameter has a large variation range as the aging time increases, it is concluded that some of the Ni_4Ti_3 precipitates merged into larger precipitates while others did not. Preferentially grown and well-aligned precipitates are favorable for this merging process compared to the stress-free conditions where all of the variants with different orientations grow freely. When the alloy is aged from 10 h to 100 h, some of the smallest precipitates start to dissolve and merge with the larger ones, leading to the increase of both the size of precipitates and their average interparticle spacing. As aging continues, this yields an inhomogeneous distribution of Ni concentration that the Ni concentration around the Ni_4Ti_3 precipitates will be higher than in the matrix, thus lead to the slightly increase of R_s temperature.

The stress field around the precipitates influences the shape change behavior of the alloy. From Table 4.2 it can be observed that the recovery ratio decreased from 88.10% or 92.86% to 42.86% when aging time is increased from 10 h to 100 h at 450°C, or aging temperature is increased from 400°C to 450°C for 100 h, respectively. When comparing the alloys aged at 400°C for 100 h and 450°C for 10 h, the difference in recovery ratio between the two samples is resulting from the difference in volume fraction. The sample which has a higher volume fraction leads to a higher recovery ratio in the shape change behaviour because higher stress fields are induced in the matrix favoring the shape change behaviour. However, the condition between the samples aged at 450°C for 10 h or 100 h is different. In this condition, the volume fraction increased as aging time increased, but the recovery ratio dramatically decreased over 50%. This vast change in the recovery ratio is caused by the quick increase in size of Ni_4Ti_3 precipitates. This indicates that when the size of the precipitates continues growing as aging time increases at such a level, the lattice of the precipitates starts to lose

coherency with the lattice of the matrix, which decreases the stress field surrounding the precipitates and finally leads to the decrease of the recovery ratio of the alloy.

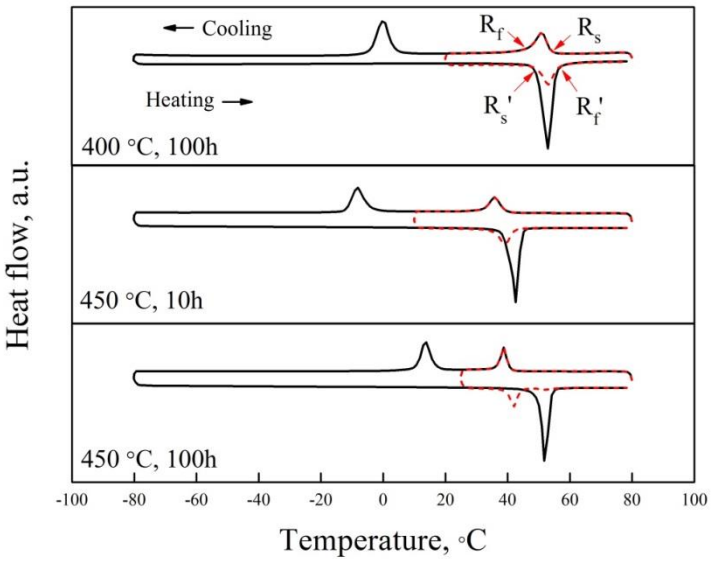

Figure 4.16 Full DSC (black) and partial DSC (red) curves of $Ni_{51}Ti_{49}$ alloy after constrained aging at different aging time and temperature.

4.4.3 Influence of the Ni_4Ti_3 precipitates on the composition of the B2 matrix

In this study, different volume fractions of the Ni_4Ti_3 precipitates were observed in different samples and such a variation of the volume fraction will imply composition differences in the respective B2 matrices. In this section the composition of the B2 matrix with different volume fractions is calculated and the influence on the transformation temperatures and shape change behaviors is discussed.

The nominal composition of the Ni-Ti alloy in this study is Ni51at.%Ti, expressed in atomic percent, which corresponds with Ni56wt.%Ti, expressed in weight percent. Calculating the relation between the volume and the weight of the alloy also needs the information of unit cell density, which can be calculated with the equation :

$$Density\ \rho = \frac{(number\ of\ atoms/cell) \cdot (atomic\ mass)}{(volume\ of\ unit\ cell) \cdot (Avogardo\ constant)}.$$

Therefore, the unit cell density of the B2 matrix and the Ni_4Ti_3 precipitate can be calculated

as follows:

$$\rho_{matrix} = \frac{(1)\cdot(58.693)g/mol + (1)\cdot(47.876)g/mol}{(26.946\times10^{-24})cm^3\cdot(6.022\times10^{23})/mol} = 16.229\ g/cm^3,$$

$$\rho_{precipitate} = \frac{(8)\cdot(58.693)g/mol + (6)\cdot(47.876)g/mol}{(182.390\times10^{-24})cm^3\cdot(6.022\times10^{23})/mol} = 6.890\ g/cm^3.$$

The sample that was constrained aged at 400°C for 100 h revealed the highest volume fraction of Ni_4Ti_3 precipitates according to Table 4.1, with 10.6% on the tension side and 10.3% on the compression side. One example calculation here takes the alloy's tension side constrained aged at 400°C for 100 h as a whole part for the calculation.

Assume that the total volume of the alloy on tension side is V, then the total mass M, as well as the mass of matrix m_{matrix} and the mass of precipitates $m_{precipitate}$ can be expressed as:

$$M = m_{precipitate} + m_{matrix} = 6.890\times0.106V + 16.229\times(1-0.106)V = 15.239V.$$

$$m_{matrix} = 14.509V, m_{precipitate} = 0.730V,$$

Since the nominal weight percent between the Ni and Ti is 0.56/0.44, the total mass of Ni and Ti in the alloy can be expressed as:

$$m_{Ni} = 0.56M = 8.534V,$$

$$m_{Ti} = 0.44M = 6.705V.$$

In Ni_4Ti_3 precipitates, the weight percent between Ni and Ti is Ni62wt.%Ti, therefore, the mass of Ni and Ti in Ni_4Ti_3 precipitates can be expressed as:

$$m_{Ni\ in\ precipitate} = m_{precipitate}\times62\% = 0.453V,$$

$$m_{Ti\ in\ precipitate} = m_{precipitate}\times38\% = 0.277V.$$

Now the mass of Ni and Ti in the matrix can be calculated as:

$$m_{Ni\ in\ matrix} = m_{Ni} - m_{Ni\ in\ precipitate} = 8.081V,$$

$$m_{Ti\ in\ matrix} = m_{Ti} - m_{Ti\ in\ precipitate} = 6.428V.$$

Therefore, the weight ratio between Ni and Ti in the matrix is 8.081V/6.428V = 1.257, which is Ni55.7wt.%Ti. After converting this weight percent into atomic percent, the final composition in the matrix is Ni50.6at.%Ti. This confirms that the composition in the matrix decreases compared to the nominal composition, which is due to the depletion of Ni from the matrix into the precipitates and the maximum Ni concentration variation from the nominal

composition is thus 0.4at.%. The change in the Ni concentration affects the martensite transformation temperatures but has very little effect on the R-phase transformation temperature and shape change behavior of the alloy. Moreover, as discussed before there will be a certain amount of inhomogeneity in the precipitate distribution inside the alloy after the aging process, which should be taken into account.

It is possible to measure the composition of the matrix using other techniques such as STEM-EDX (scanning transmission electron microscopy – energy-dispersive X-ray spectroscopy) or EELS (electron energy loss spectroscopy), but the quantification accuracy of these techniques is insufficient enough to distinguish the present Ni concentration variation which is below 1% based on the above calculation. The quantification of EDX can reach around 5~7% after a ZAF (Z = atom number effect, A = self-absorption effect, F = fluorescence effect) correction process which is performed on the measured X-ray intensities [118]. The quantification accuracy of EELS typically not exceeds 3% when it is applied to Ni-Ti alloys according to the study made by Yang et al. [51]. However, there are still other techniques which can reach the accuracy for the composition study in this case, WDS (wavelength-dispersive X-ray spectroscopy) is one of the alternative techniques that can reach a higher accuracy of around 1% [108], and APT (atom probe tomography) can reach an even higher accuracy down to atomic scale since Ni and Ti have very similar field evaporation parameters (4.435 eV for Ni and 4.855 eV for Ti) so they have a similar efficiency to be evaporated and detected. However, in the available experimental instruments at EMAT do not support such analysis. Therefore, it is not possible to validate the volume fraction by measuring the composition of the matrix in this study.

In this study, different microstructures have different length scales which need different techniques to obtain statistical information. In the present $Ni_{51}Ti_{49}$ alloy, the size of Ni_4Ti_3 precipitates is below hundreds of nm, and the grain size is around tens of micron. For such scales it is possible to reveal the Ni_4Ti_3 precipitates with TEM and ACOM-TEM. The FIB slice-and-view technique also can be used to study the microstructure of the precipitates and

matrix, and can include a larger observation region which can include more grains with a lower resolution compared to TEM. For the information of texture, it can be observed both from smaller scale or larger scale by different techniques. EBSD (Electron backscatter diffraction) can indicate the texture information on the scale of hundreds of micron, while XRD (X-ray diffraction) or neutron diffraction can reveal texture information from macro-scale bulk materials of mm or even larger scale.

4.5 Conclusions

The ACOM-TEM technique was applied to a Ni-Ti shape memory system for a quantitative study of Ni_4Ti_3 precipitates to acquire both orientation and phase distribution information. This technique can provide clear visual phase and orientation information inside the alloy from a microscopic point of view. Phase maps can be used to distinguish the Ni_4Ti_3 precipitates from the matrix in a convenient and effective manner, enabling quantitative analysis of the relationship between the precipitates and treatment parameters, which may affect the appearance and distribution of the precipitates. Orientation maps can be used to determine the Ni_4Ti_3 variants and their relation with the other factors such as the external stress in this study.

In the constrained-aged $Ni_{51}Ti_{49}$ alloy, the highest Ni_4Ti_3 precipitates density leads to the highest recovery ratio in ARSME, which is observed in the alloy aged at 400°C for 100 h under constrained stress. The highest volume fraction of the Ni_4Ti_3 precipitates observed is approximately 10.6% on the tension side and 10.3% on the compression side. In the constrained aging process which can induce ARSME, the influence of the aging time and temperature on the volume fraction appears mainly to be due to the changes in the interparticle spacings rather than due to the changes in the size or the shape of the Ni_4Ti_3 precipitates. When external stress was applied during aging without a fixed relation to the crystal orientation of the grains, the preferential growth of Ni_4Ti_3 precipitates will appear

such that the Ni_4Ti_3 variant that has the largest angle with the external tensile stress will grow preferentially, and the Ni_4Ti_3 variant that has the smallest angle with the external compression stress will grow preferentially, confirming earlier work on single crystals.

Chapter 5

TEM investigation of nano-sized Ni_4Ti_3 precipitates in a low-temperature aged $Ni_{51}Ti_{49}$ shape memory alloy

5.1 Introduction and material preparation

5.1.1 Introduction

As discussed in the first chapter, there are several ways to induce the TWSME in Ni-Ti shape memory alloys, and TWSMEs are usually induced by a training process. Unlike other training processes that induce the TWSME by creating dislocations or selected martensite variants, a constrained aging process induces the TWSME by preferentially growing Ni_4Ti_3 precipitate variants, and eventually, only one Ni_4Ti_3 orientation variant appears instead of four variants. The preferential growth of Ni_4Ti_3 variants is closely related to the distribution of external stress during the constrained aging process. Such a TWSME induced by constrained aging usually shows a special shape change, in which the curvature of the arc shaped strips will reverse when martensitic transformation occurs, and this special shape transformation behavior is known as ARSME (all round shape memory effect).

Recently, an abnormal TWSME induced by low-temperature constrained aging was observed by Li et al., in which the shape change of the alloy strip during martensitic transformation was different than that of normal constrained aged Ni-Ti alloys [98]. Li et al. found that when aging was applied at relatively low temperatures, the strip will bend towards the constrained direction region during the martensitic transformation upon cooling, rather than away from

the constrained direction region as observed for normal ARSME. Figure 5.1 illustrates the mechanism of this abnormal TWSME and shows the combined action between the residual stress field produced by the constrained aging and the stress field produced by the coherent Ni_4Ti_3 precipitates. In the case of normal TWSME, the stress field plays the dominant role during the martensitic transformation, because the Ni_4Ti_3 precipitates are relatively large, while in the case of abnormal TWSME, the residual stress field plays the dominant role due to the weak stress field produced by the small Ni_4Ti_3 precipitates.

In their study of abnormal TWSME, Li et al. also discovered the critical condition by which the abnormal TWSME can occur. When the aging time is fixed at 1 h, an aging temperature below 385 °C can induce the abnormal TWSME, and when the aging temperature is fixed at 350 °C, a time shorter than 6 h can induce the abnormal TWSME. Although this critical condition was found, the full understanding of how Ni_4Ti_3 precipitates affect TWSME during low-temperature constrained aging is still limited. Therefore, it is necessary to use TEM to characterize the microstructure of the Ni_4Ti_3 precipitates, including their sizes and growth, and starting from nanoscale structures. In this chapter, conventional TEM, HRTEM and GPA methods are used to investigate the Ni-Ti alloys that were constrained aged at 350 °C for 1 h, 6 h and 10 h, and some quantitative data was obtained to better understand the evolution of the Ni_4Ti_3 precipitates when the alloy is changed from the abnormal TWSME state to the normal TWSME state.

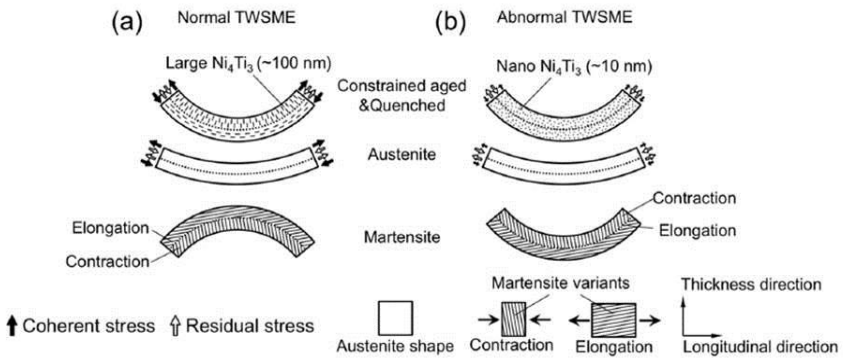

Figure 5.1 An illustration of the mechanism of (a) normal TWSME and (b) abnormal TWSME [98].

5.1.2 Material preparation

The $Ni_{51}Ti_{49}$ alloys used in this study were prepared by the arc melting method using electrolytic nickel (purity >99.9%) and titanium sponge (purity >99.7%). The melting process was repeated six times for every ingot in a non-consumable vacuum arc melting furnace connected to a vacuum casting part with a water-cooled thick copper mold. The dimensions of the Ni-Ti ingots after melting and casting are 70 × 8 × 0.5 (length × width × thickness) mm^3. To homogenize the composition of the alloys, a solid solution treatment at 850 °C for 3 h under an Ar (purity 99.9%) protective atmosphere followed by water quenching was applied. After the solid solution treatment, constrained aging was applied to introduce the TWSME of the alloy. Ni-Ti strips were placed in a specially designed arc mold with a diameter of 48 mm and underwent aging for 1 h, 6 h and 10 h at 350 °C; the structure of the mold used for the constrained aging is the same as that shown in Figure 4.1a.

The phase transformation temperatures were studied by DSC (Q200, TA), and the microstructure of the alloy was investigated by TEM (Tecnai G2/Themis Z, Thermo Fisher scientific; JEM-2100F, JEOL). The TEM specimens were prepared by twin-jet electropolishing. Electropolished specimens are prepared from the top side of the strip, which shows tensile stress, as can be seen in Figure 4.1b.

5.2 TEM investigation of the Ni_4Ti_3 precipitates in a low-temperature constrained aged $Ni_{51}Ti_{49}$ alloy

5.2.1 Conventional TEM study

Figure 5.2 shows the conventional TEM results of the samples constrained aged at 350 °C for 1 h. In Figure 5.2a, the SAED pattern was taken from the $[012]_{B2}$ zone axis, and from the diffraction pattern, the superspots from one variant of the Ni_4Ti_3 precipitates can be clearly observed along the 1/7 $(32\bar{1})$ positions. Here it is important to note that in a non-constrained aged sample one would expect superspots belonging to two variants. Meanwhile, superspots

of the R phase are also observed in the diffraction pattern, because the R_s temperature of all these samples is close to room temperature. Figure 5.2b shows the BF image of the same sample and Figure 5.2c shows the corresponding DF image taken from the region indicated by the white circle in Figure 5.2a. Due to the limitation of the objective aperture size, the region selected on the diffraction pattern for the DF image always included two or more spots; however, since no spot from the Ni-Ti B2 phase was selected to form the DF image, the DF image results can reveal information concerning the Ni_4Ti_3 precipitates. In Figure 5.2c, a high density of more or less round bright dots with diameters less than 5 nm and dispersedly distributed and corresponding to Ni_4Ti_3 precipitates is found. Most of these bright dots are quite blurred with the background and do not have clearly visible boundaries, whereas few dots have clear boundaries with the matrix. These bright dots in the DF image give an indication the nanoscale, shape and distribution of the Ni_4Ti_3 precipitates when the alloy was constrained aged at 350 °C for 1 h. The R phase spot included in the white circle of Figure 5.2a leads to the appearance of the bright grey matrix compared to darker matrix regions in Figure 5.2c.

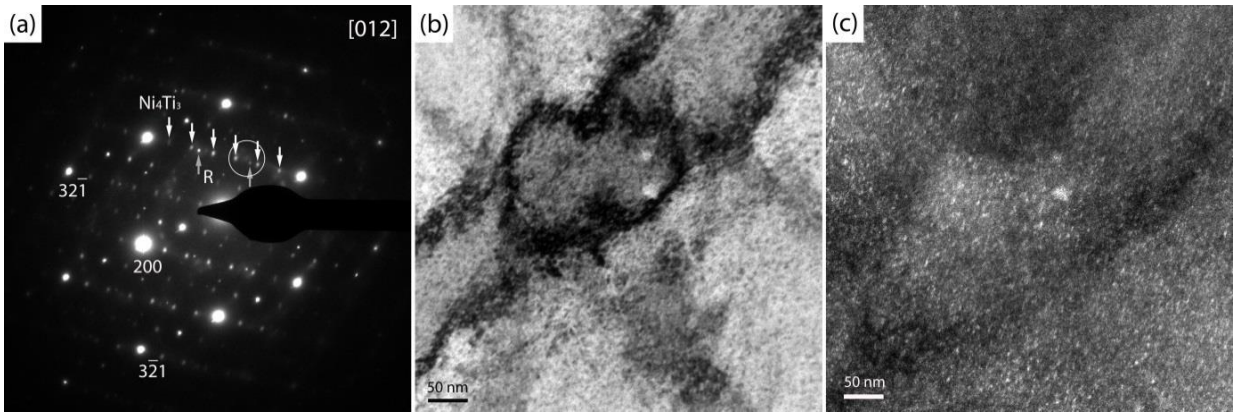

Figure 5.2 Conventional TEM study of the alloy constrained aged at 350 °C for 1 h. (a) Electron diffraction pattern showing Ni_4Ti_3 and R-phase superspots, (b) BF image, and (c) corresponding DF image taken from the region indicated by the white circle in (a).

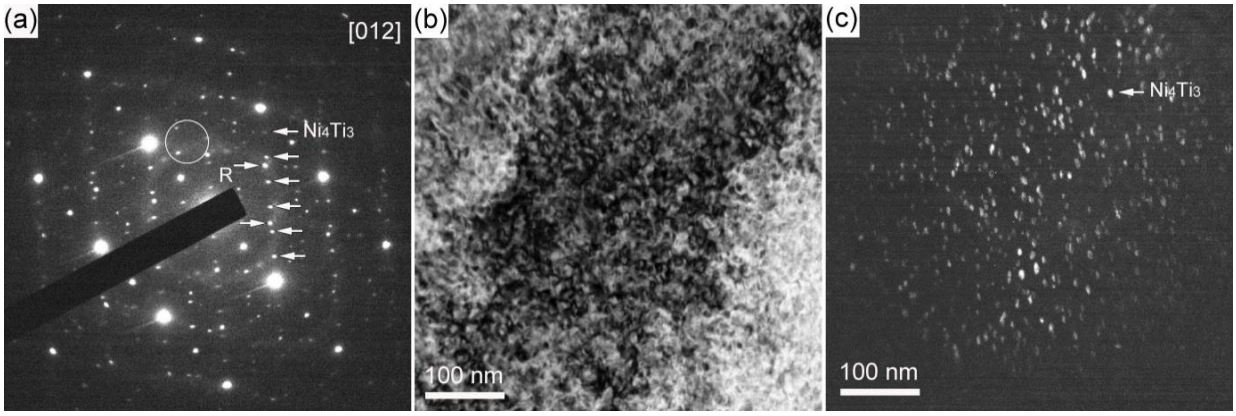

Figure 5.3 Conventional TEM study of the alloy constrained aged at 350 °C for 6 h. (a) Electron diffraction pattern showing Ni_4Ti_3 and R-phase superspots, (b) BF image, and (c) corresponding DF image taken from the region indicated by the white circle in (a).

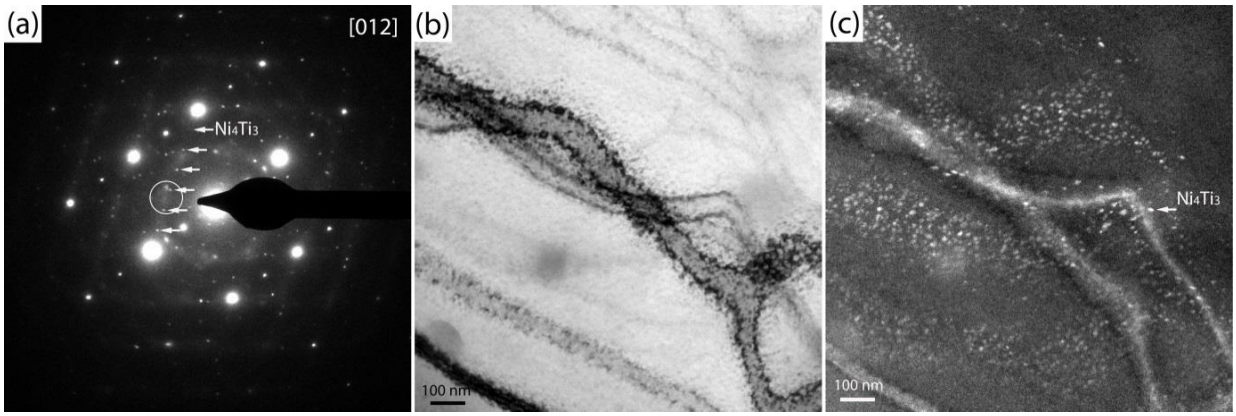

Figure 5.4 Conventional TEM study of the alloy constrained aged at 350 °C for 10 h. (a) Electron diffraction pattern showing Ni_4Ti_3 superspots, (b) BF image, and (c) corresponding DF image taken from the region indicated by the white circle in (a).

Figure 5.3 shows the conventional TEM results of the sample constrained aged at 350 °C for 6 h. Similar to the SAED pattern obtained for the sample constrained aged at 350 °C for 1 h, the SAED pattern in Figure 5.3a shows only superspots from one variant of the Ni_4Ti_3 precipitate plus some R-phase superspots. Figure 5.3b shows the BF image, and Figure 5.3c shows the corresponding DF image. The size of the Ni_4Ti_3 precipitates in Figure 5.3c is larger than that of the precipitates shown in Figure 5.2c and their shape is of a more elliptic type with lengths that are larger than 5 nm.

Figure 5.4 shows the conventional TEM results of the sample constrained aged at 350 °C for 10 h. The SAED pattern in Figure 5.4a shows that again only one variant of the Ni_4Ti_3 precipitate appeared, and these precipitates can be seen in Figure 5.4c, which is the DF image from the corresponding region of the BF image in Figure 5.4b. The size of the Ni_4Ti_3 precipitates has further increased to approximately 10 nm, and no obvious density change can be observed from the DF image.

5.2.2 HRTEM study

Since the very small Ni_4Ti_3 precipitates examined in this study are very difficult to characterize by conventional TEM, HRTEM was used to observe the precipitates in these low-temperature constrained aged alloys. Figure 5.5 shows a typical HRTEM result along the same [012] viewing direction as in Fig. 5.2 of the sample constrained aged at 350 °C for 1 h. Figure 5.5a shows the HRTEM image, from which it can be observed that variations exist in different regions; some regions show clear arrangement of atom columns when compared to a B2 matrix, while in other regions, the dots are quite blurred. If an FFT is applied to the regions indicated by white squares, denoted as regions 1 and 2 in Figure 5.5a, the FFT results of regions 1 and 2 are seen to be different. Figure 5.5c shows the FFT result of region 1, and Figure 5.5d shows the FFT result of region 2; bright spots corresponding to the (012) B2 matrix are visible in both of the patterns, but the pattern in Figure 5.5c has extra superspots corresponding to the Ni_4Ti_3 precipitate structure. This difference in the FFT results indicates that Ni_4Ti_3 precipitates have already formed in region 1, while only the Ni-Ti B2 matrix is present in region 2. Although Ni_4Ti_3 was observed in Figure 5.5a, it is not easy to identify the boundary between the precipitates and the matrix. One reason for this difficulty is that the Ni_4Ti_3 precipitates are still very small, and the well-known lenticular shape did not form yet; thus, the contrast between the matrix and the precipitates is limited. In addition, the (012) zone axis is not a perfect zone for observing the boundary between the Ni-Ti B2 matrix and the precipitates, because it is not an ‘edge on’ condition even for full-grown precipitates, and the matrix and precipitates will thus overlap on the boundary regions, which increases the

difficulty of clearly observing the precipitates ('edge on' condition is $[110]_{B2}$). Figure 5.5b shows the FFT of the entire image of Figure 5.5a, and from this FFT pattern, more than one variant of Ni_4Ti_3 precipitates can be observed, as indicated by the white and red arrows shown in Figure 5.5b. The first variant indicated by the white arrows takes the dominant position, and most of the brighter superspots in this pattern correspond to this variant. The superspots shown in Figure 5.5c also belong to the variant indicated by the white arrows in Figure 5.5b. However, another Ni_4Ti_3 variant exists and is indicated by the red arrows in Figure 5.5b. The superspots attributed to this variant are very weak, and some of these superspots even have diffuse intensities. However, the presence of these less intense superspots still proves that more than one variant appeared at an early stage of the formation of the Ni_4Ti_3 precipitates. Although this was not recognized in the conventional SAED pattern, this observation is reasonable because the preferential growth of the Ni_4Ti_3 precipitates is caused by the interaction of the external stress induced during aging with the stress field induced by the precipitates. However, in the early stage of precipitate formation, the stress field induced by the precipitates is too small, and thus the restriction of the external stress to the precipitates is also limited, which enables the appearance of more than one variant. As the size of the precipitate increases, the interaction between the external stress and the internal stress field also increases, which will gradually restrict the growth of other variants until only one variant having the best orientation with the external stress remains, as discussed in Chapter 4.

Figure 5.6 shows the HRTEM results of the sample constrained aged at 350 °C for 6 h. Figure 5.6a shows the HRTEM image obtained from the (012) zone axis, and from the HRTEM image, it is possible to observe several Ni_4Ti_3 precipitates having clear boundaries with the matrix. These precipitates already reveal an elliptical shape, which means that the aspect ratio starts to increase under this aging condition. The two regions denoted as regions 1 and 2 were selected from the HRTEM image, and their corresponding FFT results are presented in Figure 5.6c and 5.6d, respectively. Figure 5.6c shows shows the reciprocal spots corresponding to

both the Ni-Ti B2 matrix and Ni_4Ti_3 precipitate, while Figure 5.6d only reveals reciprocal spots corresponding to the Ni-Ti B2 matrix. The FFT of the entire HRTEM image of Figure 5.6a is shown in Figure 5.6b in which the spots corresponding to only one variant of Ni_4Ti_3 precipitates are seen, which means that as the precipitates grow the external stress starts to affect the preferential growth of the Ni_4Ti_3 precipitates during constrained aging.

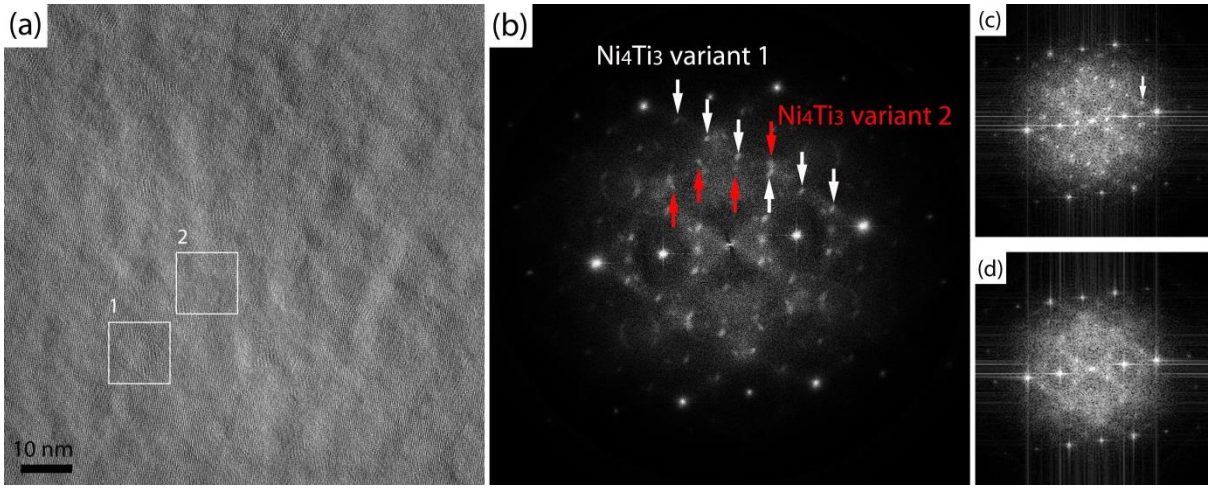

Figure 5.5 HRTEM study of the alloy constrained aged at 350 °C for 1 h. (a) HRTEM image from the [012] zone axis, (b) FFT of (a), and (c) and (d) FFT results of regions 1 and 2 shown in (a), respectively.

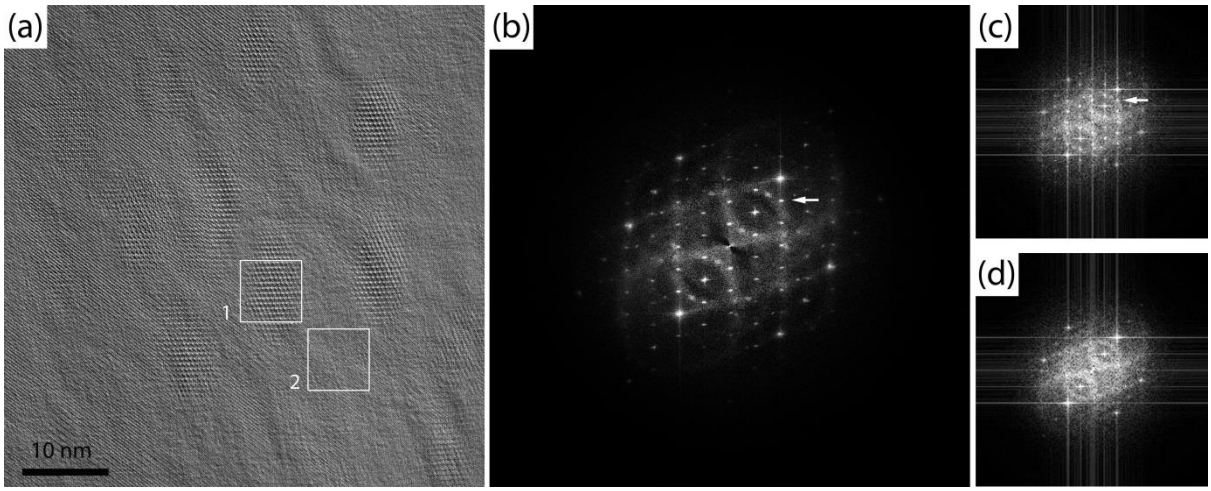

Figure 5.6 HRTEM study of the alloy constrained aged at 350 °C for 6 h. (a) HRTEM image from the [012] zone axis, (b) FFT of (a), and (c) and (d) FFT results of regions 1 and 2 shown in (a), respectively. White arrows indicate the superspots corresponding to the Ni_4Ti_3 precipitates.

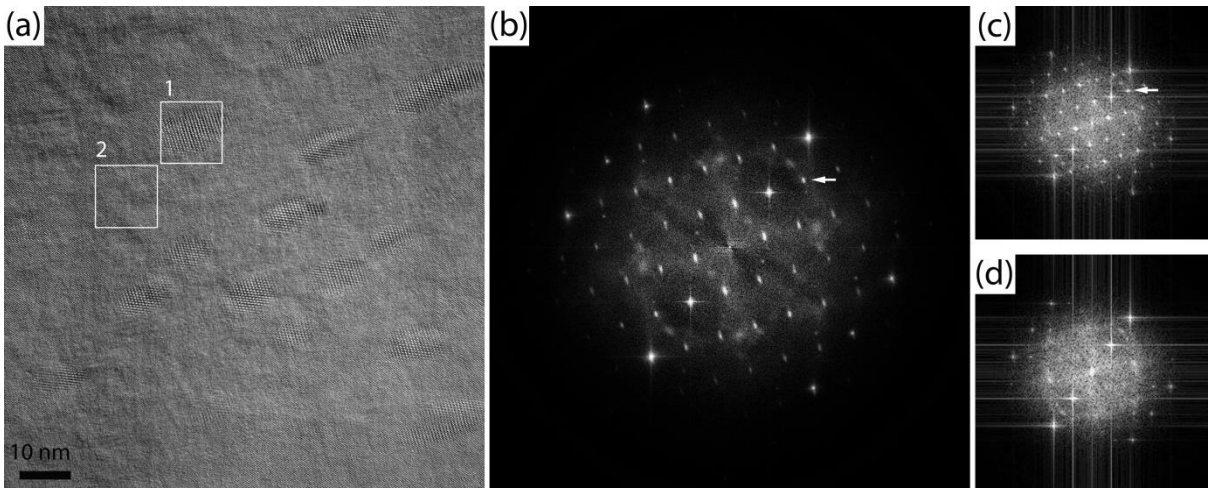

Figure 5.7 HRTEM study of the alloy constrained aged at 350 °C for 10 h. (a) HRTEM image from the [012] zone axis, (b) FFT of (a), and (c) and (d) FFT results of regions 1 and 2 shown in (a), respectively. White arrows indicate the superspots corresponding to the Ni_4Ti_3 precipitates.

Figure 5.7 shows the HRTEM results of the sample constrained aged at 350 °C for 10 h. Figure 5.7a shows the HRTEM image obtained from the [012] zone axis. Compared to Figures 5.5 and 5.6, the Ni_4Ti_3 precipitates observed in Figure 5.7a have clearer shapes and larger aspect ratios, and the boundary between the Ni_4Ti_3 precipitates and the matrix shown in Figure 5.7a is also easier to distinguish than that seen in Figures 5.5 and 5.6. The two regions containing precipitates and pure matrix, denoted as regions 1 and 2, were selected from the HRTEM image, and their corresponding FFT results are presented in Figure 5.7c and 5.7d, respectively. The FFT pattern in Figure 5.7c shows the reciprocal spots corresponding to both the Ni-Ti B2 matrix and Ni_4Ti_3 precipitate, and the FFT pattern in Figure 5.7d shows the reciprocal spots corresponding to only the Ni-Ti B2 matrix. Figure 5.7b shows the FFT result of the entire HRTEM image of Figure 5.7a, which also shows reciprocal spots corresponding to both the Ni-Ti B2 matrix and one variant of Ni_4Ti_3 precipitates. The shape of the reciprocal spots corresponding to the Ni_4Ti_3 precipitates in Figure 5.7b is clearly elongated from round dots to ellipses, which is caused by the shape of the precipitates observed in the HRTEM image. This effect, usually referred to as streaks and is a diffraction artifact, in which the shape of a reciprocal spot is determined by the Fourier transform of the shape function of the

crystal, and when the shape function decreases in one direction, the perpendicular direction of the Fourier transformed image elongates. Therefore, an obvious elongation of the shape of reciprocal spots proves that the shape of the precipitates also changes in real space, in this case indicating a change in the aspect ratio.

5.2.3 Virtual dark field (VDF) study of the HRTEM images

The differences in the size and distribution of the Ni_4Ti_3 precipitates under different aging times were observed by the above conventional TEM and HRTEM studies, but these studies are insufficient for clearly and quantitatively explaining the relationship between the Ni_4Ti_3 precipitates and the normal/abnormal TWSMEs. Therefore, a more quantitative understanding of the Ni_4Ti_3 precipitates should be obtained for further analysis. The HRTEM images can be used to statistically analyze the size and shape of the Ni_4Ti_3 precipitates under different aging conditions by generating virtual dark field (VDF) images from the Fourier transformed reciprocal lattice patterns of the HRTEM images. The VDF images used in this study were generated by selecting one reciprocal spot corresponding to the Ni_4Ti_3 precipitates from the FFT patterns and then applying the IFFT to the masked region, where only the single selected reciprocal spot was examined. Since the VDF images were created by applying the reciprocal spot corresponding to the Ni_4Ti_3 precipitates, the VDF images only contain the information concerning the Ni_4Ti_3 precipitates. Figure 5.8 shows a typical example of a VDF image of a sample constrained aged at 350 °C for 1 h. Figure 5.8a shows the original VDF image; because the Ni_4Ti_3 precipitates are very small under this aging condition and the observation region is relatively large, the characteristics of the precipitates are not obvious, but when the image is magnified, as shown in the inset, small brighter regions can be observed in the image indicating the presence of Ni_4Ti_3 precipitates. By adjusting the threshold of Figure 5.8a, it is then possible to obtain an image as shown in Figure 5.8b, from which the Ni_4Ti_3 precipitates are clearly distinguishable from the matrix.

The process to determine the threshold and distinguish precipitates in the image is usually

known as image binarization. For a grayscale image, the idea of image binarization is to identify each pixel in the image as a background pixel if the gray level $I_{i,j}$ is less than or equal to some fixed constant T (that is, $I_{i,j} \leq T$), or a foreground pixel if the gray level $I_{i,j}$ is greater than that constant. The value of this constant, which is used to divide the foreground and background pixels, is the threshold. There are different algorithms to calculate a proper threshold value to binarize the image. In the present work, the image binarization is performed in ImageJ© which has 16 different algorithms that can be used to determine the threshold value. After comparing the results of the final images obtained from the different algorithms with the original HRTEM images, the MaxEntropy thresholding algorithm showed the best result with a difference in size of about 5%. The size difference is calculated by manually measuring the length l of several precipitates which can be clearly observed in both the HRTEM image (e.g., Figure 5.7a) and the binarized image, and then the difference between different images is calculated as: $\frac{|l_1 - l_2|}{|l_1, l_2|_{min}}$ and expressed in %.

The MaxEntropy algorithm uses the posteriori entropy of the gray level histogram as the reference to determine the proper threshold value for the image processing. In a grayscale image, the probability distribution of gray-level p_i can be expressed as:

$$p_i = \frac{f_i}{N} \text{ , } i = 1,2,\ldots,n,$$

where f_i is the observed gray-level frequency, N is the total number of pixels in the image and n is the number of gray-levels, with $\sum_{i=1}^{n} f_i = N$. The posteriori entropy is defined by

$$H_n = -\sum_{i=1}^{n} p_i \ln(p_i) \, .$$

When a certain value of the threshold s is applied, the image will be separated into two parts, the above defined background and foreground, by this threshold. The cumulative probability of these two parts can be described as:

$$P_s = \sum_{i=1}^{s} p_i \, , 1 - P_s = \sum_{i=s+1}^{n} p_i$$

Therefore, the probability distributions of the two parts are:

$$\text{A: } \frac{p_1}{P_s}, \frac{p_2}{P_s}, \ldots, \frac{p_s}{P_s}$$

$$\text{B: } \frac{p_{s+1}}{1-P_s}, \quad \frac{p_{s+2}}{1-P_s}, \ldots, \quad \frac{p_n}{1-P_s}.$$

The corresponding entropies associated with each distribution of part A and B are as follows:

$$H(A) = -\sum_{i=1}^{s} \frac{p_i}{P_s} ln \frac{p_i}{P_s} = lnP_s + \frac{H_s}{P_s}$$

$$H(B) = -\sum_{i=s+1}^{n} \frac{p_i}{1-P_s} ln \frac{p_i}{1-P_s} = \ln(1-P_s) + \frac{H_n - H_s}{1-P_s}$$

The sum of H(A) and H(B) is defined as *ψ(s)*, which can be maximized to obtain the maximum information between the foreground and background distributions in the image. The discrete value *s* which maximize *ψ(s)* is then determined as the threshold value [109].

In a following step after the threshold determination, ImageJ© can be used to quantitatively analyze the size and shape of the precipitates in this modified image. When creating a VDF image, the size of the applied mask influences the spatial resolution in the reconstructed image and eventually influences the measured size of the precipitates, therefore, the influence of the size of the applied mask also needs to be discussed. To study the size of the applied mask Figure 5.7a is used as the original image for the analysis, because in Figure 5.7a the Ni_4Ti_3 precipitates have a relatively clear boundary with the matrix and it is easier to calculate the size difference by comparing the length of precipitates obtained both in VDF image and HRTEM image, the latter done by hand, which is done in the same way as

determining the threshold algorithm discussed above. Table 5.1 shows the relationship between the diameter of the applied mask and the size difference. The size of the reciprocal spot in Figure 5.7b is 0.016 1/nm, therefore, 0.016 1/nm is the smallest possible diameter of the mask applied on the FFT image. As the diameter of the applied mask increases, the size difference of precipitates between VDF image and HRTEM image first decreases and then increases. The smallest size difference is observed when the diameter of the applied mask is 0.028 1/nm. The reason why the size difference first decreases and then increases as the diameter of the mask increases can be explained by the calculation process of the threshold which directly affects the results of the quantification of the precipitates. Since the MaxEntropy algorithm calculates the posteriori entropy of the image as described above, the threshold is determined by the maximum entropy and the value of the entropy is strongly affected by the probability distribution p_i. When the size of the applied mask changes, the information obtained from precipitates and background also changes. If the size of the applied mask is too small or too big, the ratio of $P_s/(1-P_s)$ would be very large and this will greatly increase the threshold value s to n (or decrease s to 1). Under such a condition, the information from the minor part will easily merge into the major part and decreases their boundary, leading to an increase in size difference in this study. Therefore, after the trial of different mask diameters, the proper value that can be used in this study can be determined.

Table 5.1 Relationship between the diameter of the applied mask on FFT image and size difference of precipitates with HRTEM images.

Mask diameter (1/nm)	0.016	0.022	0.028	0.032	0.041	0.054
Size difference	27%	10%	5%	6%	13%	17%

In this study, six VDF images were generated from every HRTEM image by selecting the six reciprocal Ni_4Ti_3 spots from a given row of the pattern. This was done for statistical reasons since the relative intensity of different reciprocal spots can vary from different regions even if

they originate from the same Ni_4Ti_3 variant. Figure 5.9 shows one example of different VDF images taken from different reciprocal spots in one FFT image which is from the alloy constrained aged at 350 °C for 1 h. In Figure 5.9b, 5.9c and 5.9d, the observed Ni_4Ti_3 precipitates appeared in different regions with similar size, therefore, a quantification combining different reciprocal Ni_4Ti_3 spots will increase the reliability of the statistical result. The same procedure was also conducted for the samples constrained aged at 350 °C for 6 h and 10 h. Figures 5.10 and 5.11 show typical examples of the VDF images before and after the threshold treatment of the samples constrained aged at 350 °C for 6 h and 10 h. After all these VDF images were generated, a quantitative analysis on the size and shape of the Ni_4Ti_3 precipitates was performed, and the results are listed in Table 5.2.

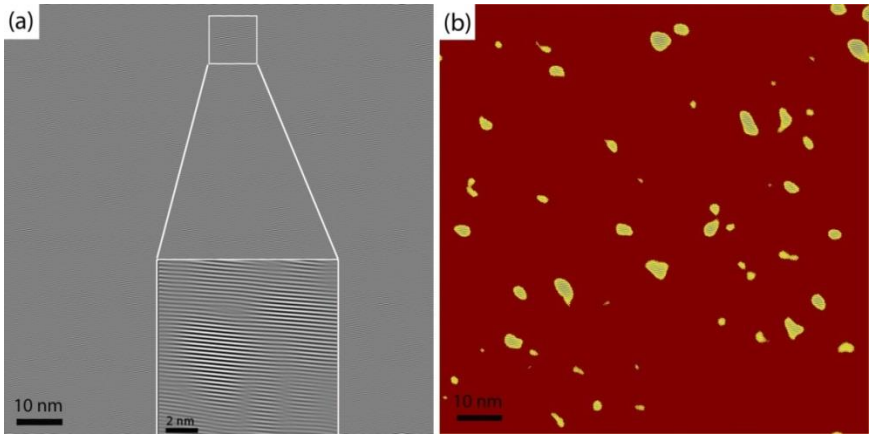

Figure 5.8 (a) Virtual dark field image of the HRTEM image of the alloy constrained aged at 350 °C for 1 h. (b) is image (a) after the threshold treatment and was used to identify the boundary between the precipitates and the matrix.

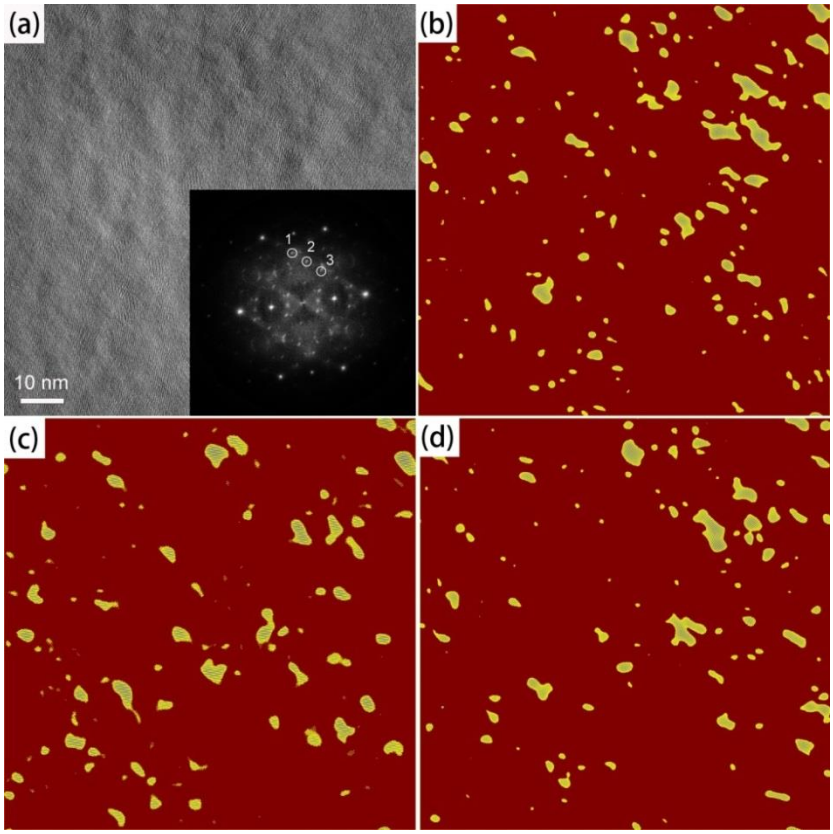

Figure 5.9 An illustration of VDF images generated from different reciprocal spots of Ni_4Ti_3. (a) HRTEM image and FFT of the alloy constrained aged at 350 °C for 1 h. (b), (c) and (d) Virtual dark field images generated from reciprocal spots 1, 2 and 3 marked in (a) respectively and applied threshold treatments to identify the boundary between the precipitates and the matrix.

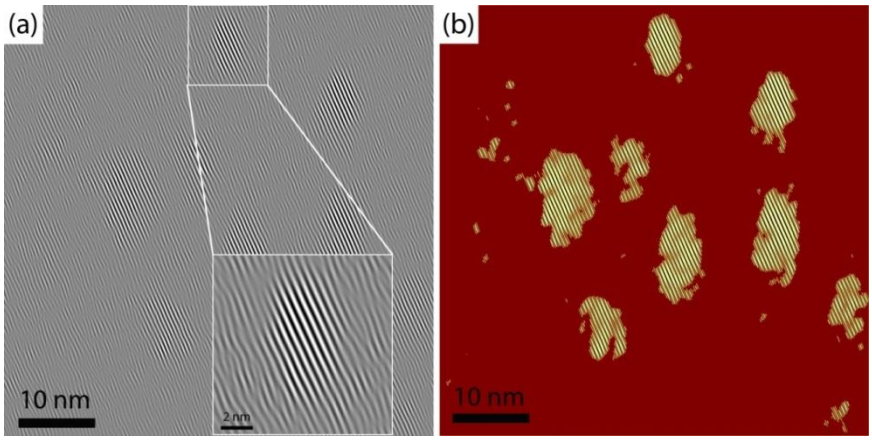

Figure 5.10 (a) Virtual dark field image of the HRTEM image of the alloy constrained aged at 350 °C for 6 h. (b) is image (a) after the threshold treatment and was used to identify the boundary between the precipitates and the matrix.

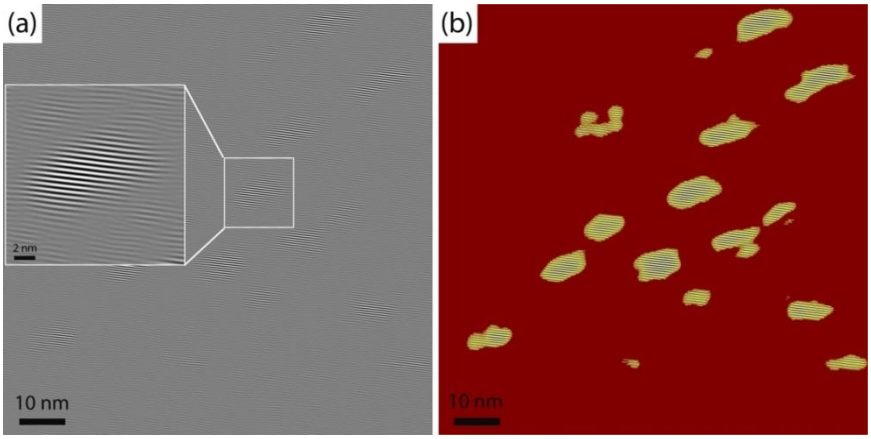

Figure 5.11 (a) Virtual dark field image of the HRTEM image of the alloy constrained aged at 350 °C for 10 h. (b) is image (a) after the threshold treatment and was used to identify the boundary between the precipitates and the matrix.

Table 5.2 shows the average size and shape of the Ni_4Ti_3 precipitates, as obtained from the series of VDF images. The table shows that as the aging time increases from 1 h to 10 h, the size and aspect ratio of the Ni_4Ti_3 precipitates also increases. For the sample constrained aged at 350 °C for 1 h, which shows the abnormal TWSME, the average length (defined as maximum Feret diameter) of the precipitates is approximately 3.7 nm, which agrees with the observation made from the conventional DF images. The aspect ratio of 1.6 of the precipitates resulting from this aging time is quite low, which means that the precipitates are still quite round instead of having a clear lenticular shape. The stress fields induced by such small, rounded shaped precipitates are very weak, which is also the reason that more than one precipitate variant was observed. When the aging time is prolonged to 6 h, the average length of the precipitates increases to approximately 6 nm, and the aspect ratio increases to 2. Since this aging condition is the critical condition between abnormal TWSME and normal TWSME, it means that the internal stress field induced by the precipitates is equal to the residual stress fields. Therefore, the magnitude of the internal stress field increases, and this increase leads to the disappearance of other Ni_4Ti_3 variants, resulting in the presence of only the preferential variant.

Table 5.2 Average sizes of the Ni_4Ti_3 precipitates with standard error in alloys treated with different aging conditions.

	Maximum Feret diameter (nm)	Minimum Feret diameter (nm)	Aspect ratio
350 °C, 1 h	3.7 ± 0.3	2.3 ±0.2	1.6 ±0.1
350 °C, 6 h	6.0 ± 0.9	3.0 ± 0.3	2.0 ± 0.3
350 °C, 10 h	8.1 ± 1.1	3.9 ± 0.4	2.2 ± 0.2

In fact, in this study, the microstructures of the rapidly solidified Ni-Ti alloys have very strong [001] textures, and Li. et al. determined that when the external stress is applied perpendicular to the [001] texture for these alloys, two Ni_4Ti_3 precipitate variants can appear during constrained aging instead of one variant [104]. However, possibly because only a narrow viewing region can be observed by HRTEM, the second Ni_4Ti_3 precipitate variant was not observed in this study. As the aging time further increases from 6 h to 10 h, the length, width (minimum Feret diameter) and aspect ratio all increase, but the aspect ratio increases slower than the size, in this case about 10% versus 30%, respectively. This indicates that when the precipitates grow as the aging time increases from 6 h to 10 h, the rate in which the length and width increase is similar. Thus, at this growth stage of the precipitates, the barriers to form stress fields along the length and width of the precipitates are similar. This differs from the condition where the precipitates become larger, where the barrier to form stress fields along the width of the precipitates would be much higher than that to form stress fields along the length of the precipitates, and this is the main reason why the precipitates have lenticular shapes after a sufficient aging treatment. In Table 5.2, the standard error increases as the aging time increases, which is due to the decrease of the number of the precipitates in the image. Since the HRTEM images have the same image size, the number of precipitates inside one image decreases as the size of the precipitates increase. Since the standard error is calculated using the equation: $SE = \frac{\sigma}{\sqrt{N}}$, where σ is the standard deviation of the data and N is the number of measured precipitates, the decrease of N leads to the increase of the standard

error.

The quantitative data of the size of the precipitates is closely related to the normal/abnormal TWSME. The appearance of normal and abnormal TWSME is caused by the combined action of residual stress and internal stress during the transformation process of the alloy. The residual stress in the alloy is induced during the constrained aging process while the internal stress is induced by the lattice mismatch between the precipitates and the surrounding matrix. Since the alloy is under the combined action of both residual stress and internal stress, different stress levels will lead to different shape change bahaviors. When the residual stress is smaller than the internal stress, the internal stress will take the dominant position during the shape change behavior of the alloy stripe and vice versa. In the normal TWSME case, the internal stress takes the dominant position to determine the shape change behavior of the alloy stripe, and the abnormal TWSME occurs when the internal stress is too small. In their study Li et al. observed the abnormal shape change behavior in the constrained aged alloy and indicated that the abnormal TWSME appeared because the internal stress is too small which makes the residual stress to take the dominant position during the transformation process, but they lack experimental proof for this argument [119]. In this study, the size of the Ni_4Ti_3 precipitates is quantitatively measured in the alloys with both normal and abnormal TWSME, and the results coincide well with the shape change behavior on macroscale. In the sample constrained aged at 350 °C for 1 h we have observed the smallest precipitates and the internal stress field induced by these small precipitates is very limited. Therefore, the internal stress in this alloy is smaller than the residual stress and abnormal TWSME appears in this sample. As the aging time increased to 6 h and 10 h, the size of the precipitates continues to grow, and the internal stress also increases which gradually becomes equal to (6 h) or larger than (10 h) the residual stress, leading to the disappearance of abnormal TWSME and the appearance of normal TWSME.

5.2.4 GPA analysis

As mentioned in the introduction and discussed above, the appearance of the abnormal TWSME is mainly due to the combined action of the stress field of precipitates and the residual stress. Therefore, the study of strain distribution can be helpful for understanding the role of precipitates. GPA is a proper option because it analyzes the local two-dimensional displacement on HRTEM images and extracts information on local strains. The HRTEM images from Figure 5.5, 5.6 and 5.7 were all used for GPA analysis and the result is displayed in Figure 5.11. Although certainly for the 6 and 10 h samples the precipitates are clearly visible in these treated images, the result shows that the strains appearing on the three images are all very low and do not exceed ~0.4%. Such values are too small to be properly quantified by GPA since it has reached the precision value of this method and can be easily affected by other factors, therefore the strain value obtained can not be regarded as the true strain value in this material. The main reason to explain this small strain value obtained with GPA which is below the lattice mismatch of both phases is the quality of the HRTEM image. Although the shape of the precipitates can be observed in the HRTEM image, the image quality in the matrix region is not good enough to identify every atom clearly due to the slight changes in focus. However, these results do indicate that the growth of Ni_4Ti_3 precipitates is quite sensitive to the external strains. Under the aging condition of 350 °C for 6 h where the size of precipitates is around 6 nm, the preferential growth of precipitates already appears.

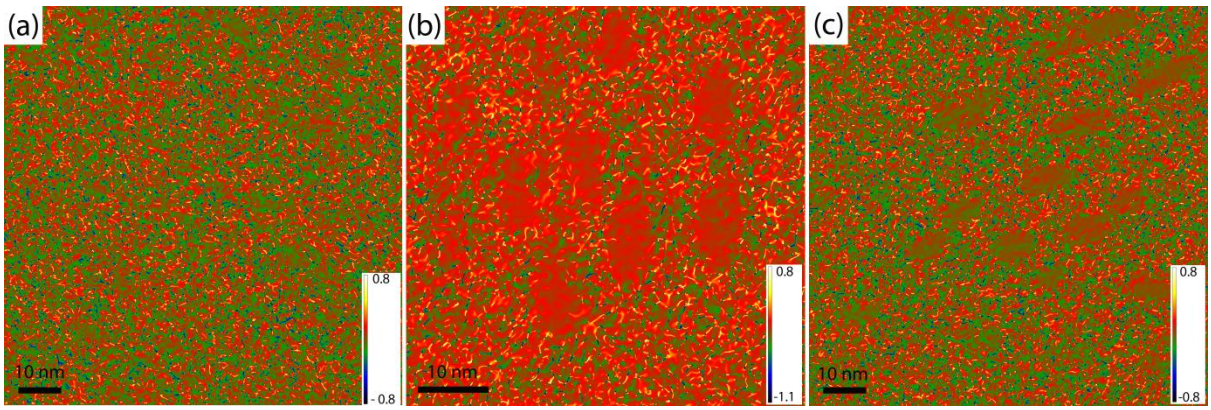

Figure 5.12 GPA results of the HRTEM images from (a) the alloy constrained aged at 350 °C for 1 h, (b) the alloy constrained aged at 350 °C for 6 h and (c) the alloy constrained aged at 350 °C for 10 h.

5.3 Conclusion

The low-temperature constrained aged $Ni_{51}Ti_{49}$ alloys with normal and abnormal TWSME were studied with various TEM techniques, and some quantitative data was obtained to better understand the evolution of the Ni_4Ti_3 precipitates during the low-temperature constrained aging process.

Ni_4Ti_3 precipitates already form in the alloy constrained aged at 350 °C for 1 h, which shows an abnormal TWSME, but observing the precipitates by TEM is not easy. The average size of the precipitates is approximately 3.7 nm, with an aspect ratio of 1.6, which is a very low value and causes the precipitates to resemble circles rather than lenticular shapes. More than one precipitate variant appeared under this aging condition, and as the aging time increased, a normal TWSME appeared, and only one variant remained in the alloy. The size and aspect ratio all increased as the aging time increased, and for the critical condition in which a normal TWSME becomes an abnormal TWSME, the size of the precipitates is approximately 6 nm.

Summary

This work focuses on the study of Ni_4Ti_3 precipitates in low temperature aged Ni-Ti shape memory alloy. A technique called “ACOM-TEM” is used in this study to help quantify the precipitates under different constrained aging conditions which will induce special two-way shape memory effects (all-round shape memory effect or abnormal two-way shape memory effect). An optimization process is carried out to the ACOM-TEM technique at first, and then the size, morphology, distribution of the Ni_4Ti_3 precipitates are studied quantitatively based on the ACOM-TEM results. In the end, nanoscaled Ni_4Ti_3 which induced an abnormal two-way shape memory effect is studied. The detailed contents of the thesis are as follows:

In Chapter 3, an optimization process of the ACOM-TEM applied to the Ni-Ti alloy is studied. This is necessary because the default settings of the ACOM-TEM cannot present a good recognition between the Ni-Ti matrix and precipitates due to the similarity in the diffraction patterns of the two phases. The optimization is applied from both the data collection process and template matching process. In the data collection process, the parameters that can affect the quality of the collected diffraction patterns are studied, a series of different values are tested for these parameters and the optimum results are obtained by comparing the shape of Ni_4Ti_3 precipitates obtained with conventional TEM images and ACOM-TEM. In the template matching process, the parameters that can affect the quality of the generated diffraction patterns are studied to improve the quality of simulated diffraction patterns for better matching to the experimental data. After the optimization, the best settings for observing the Ni_4Ti_3 precipitates by ACOM-TEM is obtained and is applied to the studies in chapter 4.

In Chapter 4, the size, morphology, and distribution of Ni_4Ti_3 precipitates in a constrained

aged Ni-Ti alloy with all-round shape memory effect are studied, together with the relation between the Ni_4Ti_3 precipitates and the direction of external stress during aging. The obtained results can be concluded as follows:

In the constrained-aged $Ni_{51}Ti_{49}$ alloy, the higher Ni_4Ti_3 precipitates density leads to a higher recovery ratio in TWSME. Among the currently designed ARSME alloys, the alloy aged at 400°C for 100 h under constrained stress provides the optimal ARSME with a Ni_4Ti_3 density of approximately 31.4% on the tension side and 28.6% on the compression side, which is the highest volume fraction value for the precipitates among all aged alloys. In the constrained aging process, which can induce ARSME, the influence of the aging time and temperature on the volume fraction is mainly due to the changes in the interparticle spacings rather than due to the changes in the size or the shape of the Ni_4Ti_3 precipitates.

When external stress was applied during aging without a fixed relation to the crystal orientation of the grains, the preferential growth of Ni_4Ti_3 precipitates will appear such that the Ni_4Ti_3 variant that has the largest angle with the external tensile stress will grow preferentially, and the Ni_4Ti_3 variant that has the smallest angle with the external compression stress will grow preferentially.

In Chapter 5, a special Ni-Ti alloy which is obtained by low temperature constrained aging and shows an abnormal TWSME is studied via both conventional TEM and HRTEM. This study reveals the nucleation and growth of Ni_4Ti_3 precipitates at very early stages where the size of precipitates is around several nanometers. Conventional TEM has reached its limit to clearly observe the morphology of precipitates and HRTEM can obtain the size and morphology information, but the strain field is too small to be studied. It is concluded that Ni_4Ti_3 precipitates already form in the alloy constrained aged at 350°C for 1 h, which shows an abnormal TWSME, but observing the precipitates by TEM is not easy. The average size of the precipitates is approximately 3.7 nm, with an aspect ratio of 1.6, which is a very low value and causes the precipitates to resemble circles rather than lenticular shapes. More than

one precipitate variant appeared under this aging condition, and as the aging time increased, a normal TWSME appeared, and only one variant remained in the alloy. The size and aspect ratio all increased as the aging time increased, and for the critical condition in which a normal TWSME becomes an abnormal TWSME, the size of the precipitates is approximately 6 nm.

To sum up, the Ni_4Ti_3 precipitates plays an important role in the two-way shape memory effect, which directly determines the shape change behavior and the recovery ratios. The size, morphology, and distribution of the precipitates are strongly influenced by the aging conditions such as stress, time and temperature. A quantitative study helps to better connect the aging conditions to the nucleation and growth of precipitates and eventually lead to a better control to the shape memory behavior.

Samenvatting

Dit werk richt zich op de studie van Ni_4Ti_3-precipitaten in een Ni-Ti-vormgeheugenlegering na veroudering en bij lage temperatuur. Een techniek genaamd "ACOM-TEM" wordt in dit onderzoek gebruikt om de precipitaten te kwantificeren onder verschillende beperkte verouderingsomstandigheden die speciale tweezijdige vormgeheugeneffecten zullen veroorzaken (veelzijdig vormgeheugeneffect of abnormaal tweeweg vormgeheugeneffect). Eerst wordt een optimalisatieproces volgens de ACOM-TEM techniek uitgevoerd en vervolgens worden de grootte, morfologie en verdeling van de Ni_4Ti_3-precipitaten kwantitatief bestudeerd op basis van de ACOM-TEM resultaten. Uiteindelijk wordt nanogeschaalde Ni_4Ti_3 bestudeerd dat een abnormaal twee-weg vormgeheugeneffect induceerde. De gedetailleerde inhoud van het proefschrift is als volgt:

In hoofdstuk 3 wordt een optimalisatieproces van de ACOM-TEM toegepast op de Ni-Ti-legering bestudeerd. Dit is nodig omdat de standaardinstellingen van de ACOM-TEM geen goede herkenning kan bieden tussen de Ni-Ti-matrix en de precipitaten vanwege de sterke overeenkomst in de diffractiepatronen van de twee fasen. De optimalisatie wordt toegepast in zowel het verzamelen van de gegevens als in de sjabloon correlatie procedure. Bij het verzamelen van de data worden de parameters bestudeerd die de kwaliteit van de verzamelde diffractiepatronen kunnen beïnvloeden, een reeks verschillende waarden worden getest voor deze parameters en de optimale resultaten worden verkregen door de vorm van Ni_4Ti_3-precipitaten te vergelijken tussen conventionele TEM-afbeeldingen en ACOM -TEM. In de sjabloon correlatie procedure worden de parameters bestudeerd die de kwaliteit van de gegenereerde diffractiepatronen kunnen beïnvloeden om de kwaliteit van gesimuleerde diffractiepatronen te verbeteren voor een betere aanpassing aan de experimentele gegevens. Na de optimalisatie worden de beste instellingen voor het observeren van de

Ni_4Ti_3-precipitaten door ACOM-TEM verkregen en toegepast op de studies in hoofdstuk 4.

In hoofdstuk 4 worden de grootte, morfologie en verdeling van Ni_4Ti_3-precipitaten in een beperkt verouderde Ni-Ti-legering met een veelzijdig vormgeheugen-effect bestudeerd, samen met de relatie tussen de Ni_4Ti_3-precipitaten en de richting van externe stress tijdens veroudering. De verkregen resultaten kunnen als volgt worden omvat:

In de $Ni_{51}Ti_{49}$-legering met beperkte veroudering leidt de hogere dichtheid van de Ni_4Ti_3-precipitaten tot een hogere herstelverhouding in TWSME. Onder de momenteel ontworpen ARSME-legeringen, biedt de legering die 100 uur verouderd werd bij 400°C onder beperkte spanning de optimale ARSME met een Ni_4Ti_3-dichtheid van ongeveer 31,4% aan de trekzijde en 28,6% aan de drukzijde, wat de grootste volumefractie aan precipitaten is onder alle verouderde legeringen. In het beperkte verouderingsproces, dat ARSME kan induceren, is de invloed van de verouderingstijd en temperatuur op de volumefractie voornamelijk te wijten aan de veranderingen in de afstanden tussen de deeltjes in plaats van aan de veranderingen in de grootte of de vorm van de Ni_4Ti_3 precipitaten.

Wanneer externe spanning werd uitgeoefend tijdens veroudering zonder een vaste relatie tot de kristaloriëntatie van de korrels zal de preferentiële groei van Ni_4Ti_3-precipitaten zodanig verschijnen dat de Ni_4Ti_3-variant die de grootste hoek heeft met de externe trekspanning bij voorkeur zal groeien, terwijl de Ni_4Ti_3-variant dat de kleinste hoek heeft met de externe compressiespanning bij voorkeur zal groeien.

In hoofdstuk 5 wordt een speciale Ni-Ti-legering bestudeerd die een abnormale TWSME laat zien na veroudering bij lage temperaturen, zowel via conventionele TEM als HRTEM. Deze studie onthult de nucleatie en groei van Ni_4Ti_3-precipitaten in zeer vroege stadia waarbij de grootte van de precipitaten rond enkele nanometers ligt. Conventionele TEM heeft zijn limiet bereikt om de morfologie van precipitaten duidelijk waar te nemen en HRTEM kan informatie over de grootte en morfologie verkrijgen, maar het spanningsveld is te klein om

degelijk te bestuderen. Er wordt geconcludeerd dat Ni_4Ti_3-precipitaten zich al vormen in de legering die 1 uur verouderd is bij 350°C, wat een abnormale TWSME vertoont, maar het observeren van de precipitaten met TEM is niet eenvoudig. De gemiddelde grootte van de precipitaten is ongeveer 3.7 nm, met een beeldverhouding van 1.6, wat een zeer lage waarde is en ervoor zorgt dat de precipitaten op cirkels lijken in plaats van lenticulaire vormen. Meer dan één precipitaatvariant verscheen onder deze verouderingstoestand en naarmate de verouderingstijd toenam, verscheen een normale TWSME en bleef slechts één variant in de legering achter. De grootte en aspectverhouding namen allemaal toe naarmate de verouderingstijd toenam, en voor de kritieke toestand waarin een normale TWSME een abnormale TWSME wordt, is de grootte van het precipitaat ongeveer 6 nm.

Samengevat spelen de Ni_4Ti_3 precipitaten een belangrijke rol in het vormgeheugeneffect in twee richtingen, dat direct het gedrag van vormverandering en de herstelverhoudingen bepaalt. De grootte, morfologie en verdeling van de precipitaten worden sterk beïnvloed door de verouderingsomstandigheden zoals stress, tijd en temperatuur. Een kwantitatief onderzoek helpt om de verouderingsomstandigheden beter te verbinden met de nucleatie en groei van precipitaten en leidt uiteindelijk tot een betere beheersing van het gedrag van een vormgeheugen.

References

[1] W.J. Buehler, J.V. Gilfrich, R.C. Wiley, Effect of Low‐Temperature Phase Changes on the Mechanical Properties of Alloys near Composition TiNi, Journal of Applied Physics 34(5) (1963) 1475-1477.

[2] G.B. KAUFFMAN, I. MAYO, The Story of Nitinol: The Serendipitous Discovery of the Memory Metal and Its Applications, The Chemical Educator 2(2) (1997) 1-21.

[3] A. Ölander, An electrochemical investigation of solid cadmium-gold alloys, Journal of the American Chemical Society 54(10) (1932) 3819-3833.

[4] A.B. Greninger, V.G. Mooradian, Strain transformation in metastable beta copper-zinc and beta copper-tin alloys, (1937).

[5] A. Nagasawa, K. Enami, Y. Ishino, Y. Abe, S. Nenno, Reversible shape memory effect, Scripta Metallurgica 8(9) (1974) 1055-1060.

[6] M. Nishida, T. Honma, All-round shape memory effect in Ni-rich TiNi alloys generated by constrained aging, Scripta Metallurgica 18(11) (1984) 1293-1298.

[7] E. Goo, R. Sinclair, The B2 To R Transformation in Ti50Ni47Fe3 and Ti49.5Ni50.5 alloys, Acta Metallurgica 33(9) (1985) 1717-1723.

[8] Q. Meng, Z. Wu, R. Bakhtiari, B.S. Shariat, H. Yang, Y. Liu, T.-h. Nam, A unique “fishtail-like” four-way shape memory effect of compositionally graded NiTi, Scripta Materialia 127 (2017) 84-87.

[9] K.H. Eckelmeyer, The effect of alloying on the shape memory phenomenon in nitinol, Scripta Metallurgica 10(8) (1976) 667-672.

[10] F.E. Wang, W.J. Buehler, S.J. Pickart, Crystal Structure and a Unique``Martensitic"Transition of TiNi, Journal of Applied Physics 36(10) (1965) 3232-3239.

[11] K.N. Melton, O. Mercier, Deformation behavior of NiTi-based alloys, Metallurgical Transactions A 9(10) (1978) 1487-1488.

[12] K. Melton, J. Simpson, T. Duerig, A new wide hysteresis NiTi based shape memory alloy and its applications, Proceedings of the International Conference on Martensitic Transformations. ICOMAT-86, 1986, pp. 1053-1058.

[13] M.B. Salamon, M.E. Meichle, C.M. Wayman, Premartensitic phases of Ti50Ni47Fe3, Physical Review B 31(11) (1985) 7306-7315.

[14] X. Lan, J.S. Leng, S.Y. Du, Design of a deployable antenna actuated by shape memory alloy hinge, Materials science forum, Trans Tech Publ, 2007, pp. 1567-1570.

[15] J. Mohd Jani, M. Leary, A. Subic, M.A. Gibson, A review of shape memory alloy research, applications and opportunities, Materials & Design 56 (2014) 1078-1113.

[16] D.J. Hartl, D.C. Lagoudas, Aerospace applications of shape memory alloys, Proceedings of the Institution of Mechanical Engineers, Part G: Journal of Aerospace Engineering 221(4) (2007) 535-552.

[17] J. Mabe, F. Calkins, G. Butler, Boeing's Variable Geometry Chevron, Morphing Aerostructure for Jet Noise Reduction, 47th AIAA/ASME/ASCE/AHS/ASC Structures, Structural Dynamics, and Materials Conference, American Institute of Aeronautics and Astronautics2006.

[18] S. Oehler, D. Hartl, R. Lopez, R. Malak, D. Lagoudas, Design optimization and uncertainty analysis of SMA morphing structures, Smart Materials and Structures 21(9) (2012) 094016.

[19] D.J. Hartl, J.T. Mooney, D.C. Lagoudas, F.T. Calkins, J.H. Mabe, Use of a Ni60Ti shape memory alloy for active jet engine chevron application: II. Experimentally validated numerical analysis, Smart Materials and Structures 19(1) (2010) 015021.

[20] D. Hartl, D. Lagoudas, F. Calkins, J. Mabe, Use of a Ni60Ti shape memory alloy for active jet engine chevron application: I. Thermomechanical characterization, Smart Materials and Structures 19(1) (2009) 015020.

[21] G.F. Andreasen, T.B. Hilleman, An Evaluation of 55 Cobalt Substituted Nitinol Wire for Use in Orthodontics, The Journal of the American Dental Association 82(6) (1971) 1373-1375.

[22] R. Pfeifer, C.W. Müller, C. Hurschler, S. Kaierle, V. Wesling, H. Haferkamp, Adaptable Orthopedic Shape Memory Implants, Procedia CIRP 5 (2013) 253-258.

[23] Festo, BionicOpter - Inspired by dragonfly flight, Festo (2013).

[24] D. Stoeckel, Shape memory actuators for automotive applications, Materials & Design 11(6) (1990) 302-307.

[25] G.F. Bastin, G.D. Rieck, Diffusion in the titanium-nickel system: I. occurrence and growth of the various intermetallic compounds, Metallurgical Transactions 5(8) (1974) 1817-1826.

[26] M. Nishida, C.M. Wayman, T. Honma, Precipitation processes in near-equiatomic TiNi shape memory alloys, Metallurgical Transactions A 17(9) (1986) 1505-1515.

[27] K. Otsuka, C.M. Wayman, Shape memory materials, Cambridge university press1999.

[28] S.P. Gupta, K. Mukherjee, A.A. Johnson, Diffusion controlled solid state transformation in the near-equiatomic Ti ・ Ni alloys, Materials Science and Engineering 11(5) (1973) 283-297.

[29] V.G. Chuprina, I.M. Shalya, Reactions of TiNi with Oxygen, Powder Metallurgy and Metal Ceramics 41(1) (2002) 85-89.

[30] L.-M. Wu, S.-K. Wu, The evolution of Ti2Ni precipitates in annealed Ti51Ni49 shape memory melt-spun ribbons, Philosophical Magazine Letters 90(4) (2010) 261-268.

[31] J. Bhagyaraj, K. Ramaiah, C. Saikrishna, S. Bhaumik, Behavior and effect of Ti_2Ni phase during processing of NiTi shape memory alloy wire from cast ingot, Journal of Alloys and Compounds 581 (2013) 344-351.

[32] J. Khalil-Allafi, W.W. Schmahl, M. Wagner, H. Sitepu, D.M. Toebbens, G. Eggeler, The influence of temperature on lattice parameters of coexisting phases in NiTi shape memory alloys—a neutron diffraction study, Materials Science and Engineering: A 378(1-2) (2004) 161-164.

[33] Y. Kudoh, M. Tokonami, S. Miyazaki, K. Otsuka, Crystal structure of the martensite in Ti-49.2 at.%Ni alloy analyzed by the single crystal X-ray diffraction method, Acta Metallurgica 33(11) (1985) 2049-2056.

[34] K.F. Hane, T. Shield, Microstructure in the cubic to monoclinic transition in titanium–nickel shape memory alloys, Acta materialia 47(9) (1999) 2603-2617.

[35] D. Schryvers, P. Potapov, nbsp, L, R-Phase Structure Refinement Using Electron Diffraction Data, MATERIALS TRANSACTIONS 43(5) (2002) 774-779.

[36] K. Bhattacharya, Microstructure of martensite: why it forms and how it gives rise to the shape-memory effect, Oxford University Press2003.

[37] J. Perkins, R.O. Sponholz, Stress-Induced Martensitic Transformation Cycling and Two-Way Shape Memory Training in Cu-Zn-Al Alloys, Metallurgical Transactions A 15(2) (1984) 313-321.

[38] L. Contardo, G. Guénin, Training and two way memory effect in Cu-Zn-Al alloy, Acta Metallurgica et Materialia 38(7) (1990) 1267-1272.

[39] Y. Liu, P.G. McCormick, Factors influencing the development of two-way shape memory in NiTi, Acta Metallurgica et Materialia 38(7) (1990) 1321-1326.

[40] Y. Liu, Y. Liu, J. Van Humbeeck, Two-way shape memory effect developed by martensite deformation in NiTi, Acta Materialia 47(1) (1998) 199-209.

[41] W. Tirry, D. Schryvers, Linking a completely three-dimensional nanostrain to a structural transformation eigenstrain, Nat Mater 8(9) (2009) 752-7.

[42] W. Tirry, D. Schryvers, K. Jorissen, D. Lamoen, Quantitative determination of the crystal structure of Ni4Ti3 precipitates, Materials Science and Engineering: A 438-440 (2006) 517-520.

[43] D.Y. Li, L.Q. Chen, Selective variant growth of coherent $Ti_{11}Ni_{14}$ precipitate in a TiNi alloy under applied stresses, Acta Materialia 45(2) (1997) 471-479.

[44] R. Kainuma, M. Matsumoto, T. Honma, The mechanism of the all-round shape memory effect in a Ni-rich TiNi alloy, Proceedings of the International Conference on Martensitic Transformations. ICOMAT-86, 1986, pp. 717-722.

[45] A.D. Pogrebnjak, S.N. Bratushka, V.M. Beresnev, N. Levintant-Zayonts, Shape memory effect and superelasticity of titanium nickelide alloys implanted with high ion doses, Russian Chemical Reviews 82(12) (2013) 1135.

[46] T. Tadaki, Y. Nakata, K. Shimizu, rsquo, ichi, K. Otsuka, Crystal Structure, Composition and Morphology of a Precipitate in an Aged Ti-51 at%Ni Shape Memory Alloy, Transactions of the Japan Institute of Metals 27(10) (1986) 731-740.

[47] W. Tirry, D. Schryvers, K. Jorissen, D. Lamoen, Electron-diffraction structure refinement of Ni4Ti3 precipitates in Ni52Ti48, Acta Crystallogr B 62(Pt 6) (2006) 966-71.

[48] M. Nishida, C.M. Wayman, Electron microscopy studies of precipitation processes in near-equiatomic TiNi shape memory alloys, Materials Science and Engineering 93 (1987) 191-203.

[49] H. Horikawa, H. Tamura, Y. Okamoto, H. Hamanaka, F. Miura, Reversible characteristic changes in yield stresses of a NiTi alloy, Proceedings of the MRS International Meeting on Advanced Materials., 1988, pp. 195-200.

[50] J. Zhang, W. Cai, X. Ren, K. Otsuka, M. Asai, The Nature of Reversible Change in M s Temperatures of Ti–Ni Alloys with Alternating Aging, Materials Transactions, JIM 40(12) (1999) 1367-1375.

[51] Z. Yang, W. Tirry, D. Schryvers, Analytical TEM investigations on concentration gradients surrounding Ni4Ti3 precipitates in Ni–Ti shape memory material, Scripta Materialia 52(11) (2005) 1129-1134.

[52] G. Fan, W. Chen, S. Yang, J. Zhu, X. Ren, K. Otsuka, Origin of abnormal multi-stage martensitic transformation behavior in aged Ni-rich Ti–Ni shape memory alloys, Acta Materialia 52(14) (2004) 4351-4362.

[53] J. Khalil-Allafi, A. Dlouhy, G. Eggeler, Ni4Ti3-precipitation during aging of NiTi shape memory alloys and its influence on martensitic phase transformations, Acta Materialia 50(17) (2002) 4255-4274.

[54] S.-y. Jiang, Y.-n. Zhao, Y.-q. Zhang, L. Hu, Y.-l. Liang, Effect of solution treatment and aging on microstructural evolution and mechanical behavior of NiTi shape memory alloy, Transactions of Nonferrous Metals Society of China 23(12) (2013) 3658-3667.

[55] J.I. Kim, S. Miyazaki, Effect of nano-scaled precipitates on shape memory behavior of Ti-50.9at.%Ni alloy, Acta Materialia 53(17) (2005) 4545-4554.

[56] K. Gall, H.J. Maier, Cyclic deformation mechanisms in precipitated NiTi shape memory alloys, Acta Materialia 50(18) (2002) 4643-4657.

[57] J. Kim, S. Miyazaki, Effect of nano-scaled precipitates on shape memory behavior of Ti-50.9at.%Ni alloy, Acta Materialia 53(17) (2005) 4545-4554.

[58] S. Kustov, B. Mas, D. Salas, E. Cesari, S. Raufov, V. Nikolaev, J. Van Humbeeck, On the effect of room temperature ageing of Ni-rich Ni–Ti alloys, Scripta Materialia 103 (2015) 10-13.

[59] X. Wang, J. Van Humbeeck, B. Verlinden, S. Kustov, Thermal cycling induced room temperature aging effect in Ni-rich NiTi shape memory alloy, Scripta Materialia 113 (2016) 206-208.

[60] S. Pourbabak, X. Wang, D. Van Dyck, B. Verlinden, D. Schryvers, Ni cluster formation in low temperature annealed $Ni_{50.6}Ti_{49.4}$, Functional Materials Letters 10(01) (2017) 1740005.

[61] D.Y. Li, L.Q. Chen, Shape of a rhombohedral coherent $Ti_{11}Ni_{14}$ precipitate in a cubic matrix and its growth and dissolution during constrained aging, Acta Materialia 45(6) (1997) 2435-2442.

[62] J. Michutta, C. Somsen, A. Yawny, A. Dlouhy, G. Eggeler, Elementary martensitic transformation processes in Ni-rich NiTi single crystals with Ni4Ti3 precipitates, Acta Materialia 54(13) (2006) 3525-3542.

[63] J. Michutta, A. Yawny, M.C. Carroll, C. Somsen, G. Eggeler, Influence of compression aging on phase transition temperatures in single crystalline Ni-rich NiTi shape memory alloys, Materialwissenschaft und Werkstofftechnik 35(5) (2004) 289-293.

[64] W. Tang, Thermodynamic study of the low-temperature phase B19′ and the martensitic transformation in near-equiatomic Ti-Ni shape memory alloys, Metallurgical and Materials Transactions A 28(3) (1997) 537-544.

[65] S. Miyazaki, S. Kimura, K. Otsuka, Shape-memory effect and pseudoelasticity associated with the R-phase transition in Ti-50·5 at.% Ni single crystals, Philosophical Magazine A 57(3) (1988) 467-478.

[66] S. Miyazaki, K. Otsuka, Deformation and transition behavior associated with theR-phase in Ti-Ni alloys, Metallurgical Transactions A 17(1) (1986) 53-63.

[67] H.C. Ling, R. Kaplow, Phase transitions and shape memory in NiTi, Metallurgical and Materials Transactions A 11(1) (1980) 77-83.

[68] G.B. Stachowiak, P.G. McCormick, Two stage yielding in a NiTi alloy, Scripta Metallurgica 21(3) (1987) 403-406.

[69] "Columns." [Online]. Available:

http://en.wikipedia.org/wiki/Transmission_electron_microscopy.

[70] V. Randle, Electron backscatter diffraction: Strategies for reliable data acquisition and processing, Materials Characterization 60(9) (2009) 913-922.

[71] B.L. Adams, S.I. Wright, K. Kunze, Orientation imaging: The emergence of a new microscopy, Metallurgical Transactions A 24(4) (1993) 819-831.

[72] F.J. Humphreys, Review: Grain and subgrain characterisation by electron backscatter diffraction, Journal of Materials Science 36(16) (2001) 3833-3854.

[73] D. Vilado, M. Veron, M. Gemmi, F. Peiro, J. Portillo, S. Estrade, J. Mendoza, N. Llorca-Isern, S. Nicolopoulos, Orientation and phase mapping in the transmission electron microscope using precession-assisted diffraction spot recognition: state-of-the-art results, Journal of microscopy 252(1) (2013) 23-34.

[74] Y.M. Wang, F. Sansoz, T. LaGrange, R.T. Ott, J. Marian, T.W. Barbee Jr, A.V. Hamza, Defective twin boundaries in nanotwinned metals, Nature Materials 12 (2013) 697.

[75] L. Cao, K. Ganesh, L. Zhang, O. Aubel, C. Hennesthal, M. Hauschildt, P.J. Ferreira, P.S. Ho, Grain structure analysis and effect on electromigration reliability in nanoscale Cu interconnects, Applied Physics Letters 102(13) (2013) 131907.

[76] E. Rauch, L. Dupuy, Rapid spot diffraction patterns idendification through template matching, Archives of Metallurgy Materials 50 (2005) 87-99.

[77] E.F. Rauch, M. Veron, Coupled microstructural observations and local texture measurements with an automated crystallographic orientation mapping tool attached to a TEM, Materials Science and Engineering Technology 36(10) (2005) 552-556.

[78] R. Vincent, P.A. Midgley, Double conical beam-rocking system for measurement of integrated electron diffraction intensities, Ultramicroscopy 53(3) (1994) 271-282.

[79] J. Portillo, E.F. Rauch, S. Nicolopoulos, M. Gemmi, D. Bultreys, Precession Electron Diffraction Assisted Orientation Mapping in the Transmission Electron Microscope, Materials Science Forum 644 (2010) 1-7.

[80] D.B. Williams, C.B. Carter, The transmission electron microscope, Springer1996.

[81] J. Gjønnes, V. Hansen, A. Kverneland, The Precession Technique in Electron Diffraction and Its Application to Structure Determination of Nano-Size Precipitates in Alloys, Microscopy and Microanalysis 10(01) (2004) 16-20.

[82] E.F. Rauch, J. Portillo, S. Nicolopoulos, D. Bultreys, S. Rouvimov, P. Moeck, Automated nanocrystal orientation and phase mapping in the transmission electron microscope on the basis of precession electron diffraction, Zeitschrift für Kristallographie International journal for structural, physical, and chemical aspects of crystalline materials 225(2-3) (2010) 103-109.

[83] M.J. Hÿtch, E. Snoeck, R. Kilaas, Quantitative measurement of displacement and strain fields from HREM micrographs, Ultramicroscopy 74(3) (1998) 131-146.

[84] J.L. Rouvière, E. Sarigiannidou, Theoretical discussions on the geometrical phase analysis, Ultramicroscopy 106(1) (2005) 1-17.

[85] X. Yao, Y. Li, S. Cao, X. Ma, Z. Xin-ping, D. Schryvers, Optimization of Automated Crystal Orientation and Phase Mapping in TEM Applied to Ni-Ti All Round Shape Memory Alloy, MATEC Web of Conferences, EDP Sciences, 2015.

[86] H. Liu, Y. Luo, M. Higa, X. Zhang, Y. Saijo, Y. Shiraishi, K. Sekine, T. Yambe, Biochemical evaluation of an artificial anal sphincter made from shape memory alloys, J Artif Organs 10(4) (2007) 223-7.

[87] M.R. Doddamani, S.M. Kulkarni, Flexural Behavior of Functionally Graded Sandwich Composite, INTECH Open Access Publisher2012.

[88] E.F. Rauch, A. Duft, Orientation maps derived from TEM diffraction patterns collected with an external CCD camera, Materials Science Forum, Trans Tech Publ, 2005, pp. 197-202.

[89] J. Ciston, B. Deng, L.D. Marks, C.S. Own, W. Sinkler, A quantitative analysis of the cone-angle dependence in precession electron diffraction, Ultramicroscopy 108(6) (2008) 514-522.

[90] E.F. Rauch, M. Veron, Solving the 180 Degree Orientation Ambiguity Related to Spot Diffraction Patterns in Transmission Electron Microscopy, Microscopy and Microanalysis 19(SupplementS2) (2013) 324-325.

[91] A. Morawiec, E. Bouzy, On the reliability of fully automatic indexing of electron diffraction patterns obtained in a transmission electron microscope, Journal of applied crystallography 39(1) (2006) 101-103.

[92] A. Avilov, K. Kuligin, S. Nicolopoulos, M. Nickolskiy, K. Boulahya, J. Portillo, G. Lepeshov, B. Sobolev, J.P. Collette, N. Martin, A.C. Robins, P. Fischione, Precession technique and electron diffractometry as new tools for crystal structure analysis and chemical bonding determination, Ultramicroscopy 107(6–7) (2007) 431-444.

[93] E.F. Rauch, M. Véron, Automated crystal orientation and phase mapping in TEM, Materials Characterization 98 (2014) 1-9.

[94] W. Tirry, D. Schryvers, Quantitative determination of strain fields around Ni4Ti3 precipitates in NiTi, Acta Materialia 53(4) (2005) 1041-1049.

[95] T. Fukuda, T. Saburi, K. Doi, S. Nenno, Nucleation and Self-Accommodation of the R-Phase in Ti–Ni Alloys, Materials Transactions, JIM 33(3) (1992) 271-277.

[96] Y. Zhou, J. Zhang, G. Fan, X. Ding, J. Sun, X. Ren, K. Otsuka, Origin of 2-stage R-phase transformation in low-temperature aged Ni-rich Ti–Ni alloys, Acta Materialia 53(20) (2005) 5365-5377.

[97] E.R. Weibel, Stereological methods, Academic Press London1979.

[98] Y.Y. Li, X.Y. Yao, S. Cao, X. Ma, C.Y. Zeng, X.P. Zhang, An abnormal two-way shape memory effect in a rapidly solidified $Ni_{51}Ti_{49}$ alloy induced by low temperature constrained aging, Scripta Materialia 149 (2018) 117-120.

[99] Y. Li, X. Yao, S. Cao, X. Ma, C. Ke, X. Zhang, Rapidly solidified and optimally constraint-aged $Ni_{51}Ti_{49}$ shape memory alloy aiming at making a purpose-designed bio-actuator, Materials & Design 118 (2017) 99-106.

[100] T. Hildebrand, P. Rüegsegger, A new method for the model-independent assessment of thickness in three-dimensional images, Journal of microscopy 185(1) (1997) 67-75.

[101] A.D. Darbal, K.J. Ganesh, X. Liu, S.B. Lee, J. Ledonne, T. Sun, B. Yao, A.P. Warren, G.S. Rohrer, A.D. Rollett, P.J. Ferreira, K.R. Coffey, K. Barmak, Grain Boundary Character Distribution of Nanocrystalline Cu Thin Films Using Stereological Analysis of Transmission Electron Microscope Orientation Maps, Microscopy and Microanalysis 19(1) (2013) 111-119.

[102] C.B. Ke, S.S. Cao, X.P. Zhang, Phase field simulation of coherent precipitation of Ni_4Ti_3 particles during stress-assisted aging of a porous NiTi alloy, Modelling and Simulation in Materials Science and Engineering 23(5) (2015) 055008.

[103] X.M. C.B. Ke, X. P. Zhang, Phase field simulation of the effect of applied external stress on growth kinetics of coherent Ni_4Ti_3 precipitate in NiTi alloy, Acta Metall Sin 46(8) (2010) 921-929.

[104] Y.Y. Li, S.S. Cao, X. Ma, C.B. Ke, X.P. Zhang, Influence of strongly textured microstructure on the all-round shape memory effect of rapidly solidified $Ni_{51}Ti_{49}$ alloy, Materials Science and Engineering: A 705 (2017) 273-281.

[105] T. Saburi, S. Nenno, T. Fukuda, Crystal structure and morphology of the metastable X phase in shape memory Ti-Ni alloys, Journal of the Less Common Metals 125(0) (1986) 157-166.

[106] 舟久保熙康, 形状記憶合金, 産業図書, 1984.

[107] D. Xue, Y. Zhou, X. Ren, The effect of aging on the B2-R transformation behaviors in Ti-51at%Ni alloy, Intermetallics 19(11) (2011) 1752-1758.

[108] Y. Liao, Practical Electron Microscopy and Database-An Online Book, can be found under http://www. globalsino. com/EM/, nd (2007).

[109] J.N. Kapur, P.K. Sahoo, A.K.C. Wong, A new method for gray-level picture thresholding using the entropy of the histogram, Computer Vision, Graphics, and Image Processing 29(3) (1985) 273-285.

List of publications

Journal articles:

X. Yao, B. Amin-Ahmadi, Y. Li, S. Cao, X. Ma, XP. Zhang, D. Schryvers. Optimization of Automated Crystal Orientation Mapping in a TEM for Ni_4Ti_3 Precipitation in All-Round SMA. Shape Memory and Superelasticity, 2016, 2 (4): 286-297.

Y. Li, **X. Yao**, S. Cao, X. Ma, C. Ke, XP. Zhang. Rapidly solidified and optimally constraint-aged $Ni_{51}Ti_{49}$ shape memory alloy aiming at making a purpose-designed bio-actuator. Materials and Design, 2017, 118: 99-106.

Y. Li, **X. Yao**, S. Cao, X. Ma, C. Zeng, XP. Zhang. An abnormal two-way shape memory effect in a rapidly solidified $Ni_{51}Ti_{49}$ alloy induced by low temperature constraint-aging. Scripta Materialia, 2018, 149: 117-120.

Conference proceedings:

X. Yao, Y. Li, S. Cao, X. Ma, XP. Zhang, D. Schryvers. Optimization of automated crystal orientation and phase mapping in TEM Applied to Ni-Ti All Round Shape Memory Alloy. In MATEC Web of Conferences, 2015, (Vol. 33, p. 03022).

X. Yao, S. Cao, X. Ma, XP. Zhang, D. Schryvers. Microstructural characterization and transformation behavior of porous $Ni_{50.8}Ti_{49.2}$. Materials Today: Proceedings, 2015, 2, S833-S836.

X. Yao, Y. Li, S. Cao, X. Ma, XP. Zhang, D. Schryvers. Quantitative investigation of the all-round shape memory effect in a $Ni_{51}Ti_{49}$ alloy by TEM orientation imaging. European Microscopy Congress, 2016.

Acknowledgements

As the last part of my thesis, I would like to say thanks to all the people that helped me and encouraged me over my PhD study.

First and foremost, I would like to give my sincere gratitude to my promoter, Prof. Dominique Schryvers, for his untiring guidance, sensible advices and kind encouragement and patience throughout the PhD study. Without his guide and support I could not accomplish my thesis. It is my best fortune to have him as my PhD promoter.

I would like to particularly thank Prof Xin-ping Zhang, for guiding me during my bachelor study and accepting me as a PhD student in the beginning of my scientific life, and then recommended me to the EMAT and became my co-promoter for my PhD study. During my stay in EMAT, he always helped and cared about me.

I would like to give my great thanks to Dr. Shanshan Cao, for helping me solving many practical problems, providing good ideas for my scientific research, and also for helping me on many other aspects related to my study.

I wish to thank the people who taught me microscopy techniques right in the beginning of my study: Jiangbo, Maggie (Hui), Kai (Li) and Zhiyi. I am grateful to all EMATers that your help and discussions helped me reach a better understanding of microscopy and you made my PhD life more colourful: He, Xiaoxing, Gang, Sijun, Roger (Haiyan), Yinggang, Yang, Ge, Lipeng, Pei, Chen, Da, Qiongyang, Kai (Du), Zezhong, Hosni, Behnam, Eva (Grieten), Gunnar, Saeid, Vahid, Andrey, Thomas, Maria (Filippousi), Alexander (Meledin), Maria (Meledina), Stuart, Nicolass, Frederic, Martin, Giulio, Gerardo, Ivan, Robert, Marcos, Eva (Bladt), Hamed, Annick, Julie, Bart, Kirsten, Dimitri,

Kristof, Roeland, Laura, Ruben, Tom, Ludo, Andre, Marnik, Christine, Sabine, Lydia, Stijn, Kim, Liesbet, Tine, Koen, Christen, Daniele, Nathalie, Elena, Svetlana, Naomi, Olesia, Antonios, Karel, Carolien, Mylene, Ece, Nesli.

I would like to acknowledge the help of SMEPers, my scientific study was started there and part of my PhD study was accomplished there: Dr. Ma Xiao, Dr. Zhou Minbo, Dr. Ke Changbo, Changzheng, Moyang, Caiyou, Zhongxun, Zhiwei and all others. My special thanks given to Yuanyuan for providing me all the materials I used and for all the discussions we had for the study, the article and the thesis.

Also many thanks to my friends that live in Europe or China, the list can not include everyone but I really appreciate the friendship and your company that inspired me when I had hard times during the study. Yun, Yuru, Quanzhi, Jia, Tianhong, Changsheng, Yuan, Jiawei, Wei, Yaofeng, Jiahao, Shengfang, Guoqiang, Songqing, Guangyu, Shanshan, Yuansheng, Yixiao, Hanzhang, Baiyang, Yicong, Sujin, Xiang, Lu, Bicheng, Jieqiong.

Finally, with all my heart I give my greatest thanks to my beloved parents. Without their firm support and encouragement I could never finish my PhD study. They deserve my deepest and most admirable thanks and I hope from this thesis they can share the happiness and achievement with me.